Astronomy & Astrophysics

HCN emission from translucent gas and UV-illuminated cloud edges revealed by wide-field IRAM 30 m maps of the Orion B GMC

Revisiting its role as a tracer of the dense gas reservoir for star formation

M. G. Santa-Maria[1], J. R. Goicoechea[1], J. Pety[2,3], M. Gerin[3], J. H. Orkisz[2,4], F. Le Petit[5], L. Einig[2,6],
P. Palud[7,5], V. de Souza Magalhaes[2], I. Bešlić[3], L. Segal[3,8], S. Bardeau[2], E. Bron[5], P. Chainais[7],
J. Chanussot[6], P. Gratier[9], V. V. Guzmán[10], A. Hughes[11], D. Languignon[5], F. Levrier[12], D. C. Lis[13],
H. S. Liszt[14], J. Le Bourlot[5], Y. Oya[15,16], K. Öberg[17], N. Peretto[18], E. Roueff[5], A. Roueff[8],
A. Sievers[2], P.-A. Thouvenin[7], and S. Yamamoto[15,16]

(Affiliations can be found after the references)

ABSTRACT

Context. Massive stars form within dense clumps inside giant molecular clouds (GMCs). Finding appropriate chemical tracers of the dense gas ($n(H_2) >$ several 10^4 cm^{-3} or $A_V > 8$ mag) and linking their line luminosity with the star formation rate is of critical importance.

Aims. Our aim is to determine the origin and physical conditions of the HCN-emitting gas and study their relation to those of other molecules.

Methods. In the context of the IRAM 30m ORION-B large program, we present 5 deg^2 ($\sim$250 pc^2) HCN, HNC, HCO$^+$, and CO $J = 1-0$ maps of the Orion B GMC, complemented with existing wide-field [C I] 492 GHz maps, as well as new pointed observations of rotationally excited HCN, HNC, H^{13}CN, and HN^{13}C lines. We compare the observed HCN line intensities with radiative transfer models including line overlap effects and electron excitation. Furthermore, we study the HCN/HNC isomeric abundance ratio with updated photochemical models.

Results. We spectroscopically resolve the HCN $J = 1$—0 hyperfine structure (HFS) components (and partially resolved $J = 2-1$ and $3-2$ components). We detect anomalous HFS line intensity (and line width) ratios almost everywhere in the cloud. About 70% of the total HCN $J = 1-0$ luminosity, L'(HCN $J = 1-0$) = 110 K km s^{-1} pc^{-2}, arises from $A_V < 8$ mag. The HCN/CO $J = 1-0$ line intensity ratio, widely used as a tracer of the dense gas fraction, shows a bimodal behavior with an inflection point at $A_V \lesssim 3$ mag typical of translucent gas and illuminated cloud edges. We find that most of the HCN $J = 1-0$ emission arises from extended gas with $n(H_2) \lesssim 10^4$ cm^{-3}, and even lower density gas if the ionization fraction is $\chi_e \geq 10^{-5}$ and electron excitation dominates. This result contrasts with the prevailing view of HCN $J = 1-0$ emission as a tracer of dense gas and explains the low-A_V branch of the HCN/CO $J =1-0$ intensity ratio distribution. Indeed, the highest HCN/CO ratios (~ 0.1) at $A_V < 3$ mag correspond to regions of high [C I] 492 GHz/CO $J =1-0$ intensity ratios (>1) characteristic of low-density photodissociation regions. The low surface brightness ($\lesssim 1$ K km s^{-1}) and extended HCN and HCO$^+$ $J = 1-0$ emission scale with I_{FIR} – a proxy of the stellar far-ultraviolet (FUV) radiation field – in a similar way. Together with CO $J = 1-0$, these lines respond to increasing I_{FIR} up to $G_0 \simeq 20$. On the other hand, the bright HCN $J = 1-0$ emission (> 6 K km s^{-1}) from dense gas in star-forming clumps weakly responds to I_{FIR} once the FUV field becomes too intense ($G_0 > 1500$). In contrast, HNC $J = 1-0$ and [C I] 492 GHz lines weakly respond to I_{FIR} for all G_0. The different power law scalings (produced by different chemistries, densities, and line excitation regimes) in a single but spatially resolved GMC resemble the variety of Kennicutt-Schmidt law indexes found in galaxy averages.

Conclusions. Given the widespread and extended nature of the [C I] 492 GHz emission, as well as its spatial correlation with that of HCO$^+$, HCN, and ^{13}CO $J = 1-0$ lines (in this order), we argue that the edges of GMCs are porous to FUV radiation from nearby massive stars. Enhanced FUV radiation favors the formation and excitation of HCN on large scales, not only in dense star-forming clumps, and it leads to a relatively low value of the dense gas mass to total luminosity ratio, α (HCN) = 29 $M_\odot$/(K km s^{-1}pc^2) in Orion B. As a corollary for extragalactic studies, we conclude that high HCN/CO $J = 1-0$ line intensity ratios do not always imply the presence of dense gas, which may be better traced by HNC than by HCN.

Key words. galaxies: ISM – ISM: clouds – photon-dominated region (PDR) – ISM: individual objects: Orion B – radio lines: ISM – astrochemistry

1. Introduction

Massive stars dominate the injection of radiative energy into their interstellar environment through ultraviolet (UV) photons. They form within cold clumps of dense gas inside giant molecular clouds (GMCs, e.g., Lada 1992; Lada & Lada 2003). Observations reveal that the star formation rate (SFR) is close to linearly proportional to the cloud mass above a visual extinction threshold of $A_V \simeq 8$ mag (Schmidt 1959, 1963; Kennicutt 1998a,b; Lada et al. 2010; Evans et al. 2020), which corresponds to an approximate gas density threshold of $n(H_2) > 10^4$ cm^{-3} (e.g., Bisbas et al. 2019). In galaxies, the far-infrared (FIR) dust luminosity (L_{FIR}, defined between 40 μm and 500 μm, see Sect. 2.5 and Sanders & Mirabel 1996) provides a measure of the

SFR, especially in starbursts (e.g., Kennicutt 1998a). The L_{FIR} and the HCN $J = 1-0$ line luminosity ($L_{HCN}\,1-0$) are linearly correlated over a broad range of spatial scales and galaxy types, from spatially resolved star-forming clumps ($L_{FIR} \simeq 10^4\ L_\odot$) to ultraluminous infrared galaxies (ULIRGs, with $L_{FIR} \geq 10^{11}\ L_\odot$) (Solomon et al. 1992; Gao & Solomon 2004b; Wu et al. 2010). These studies suggest that $L_{HCN\,1}-0$ is a good tracer of the dense star-forming gas mass. However, the $L_{CO}\,1-0$ to L_{FIR} luminosity ratio in ULIRGs is lower than in normal galaxies. This leads to a superlinear relationship $L_{FIR} \propto L_{CO}^{N>1}$ (e.g., Kennicutt 1998b; Gao & Solomon 2004a). The above relations are observational proxies of the so-called Kennicutt-Schmidt (KS) relationship, $\Sigma_{SFR} = a\,\Sigma_{H_2}^N$, where Σ_{SFR} and Σ_{H_2} are the SFR and molecular gas surface densities. One obtains $N \approx 1.5$ assuming that a roughly constant fraction of the gas present in molecular clouds is subsequently converted into stars each free-fall time (e.g., Madore 1977; Elmegreen 2002).

HCN has a high dipole moment ($\mu_e = 2.99$ D), 30 times higher than that of CO. The HCN $J = 1-0$ line is commonly used as a tracer of dense gas because of its high critical density (n_{cr}), the density for which the net radiative decay from $J = 1$ equals the rate of collisional (de-)excitations out of the upper level. This results in $n_{cr}(HCN\ J = 1-0) \simeq 3 \times 10^5$ cm^{-3} for collisions with H_2 at 20 K (see Table 1 for references on spectroscopy and collisional rate coefficients). However, as lines become optically thick, radiative trapping becomes important, leading to lower effective critical densities ($n_{cr,\,eff}$; e.g., Evans 1999; Shirley 2015).

The end ^{14}N atom has a large nuclear electric quadrupole moment (O'Konski & Ha 1968) and nuclear spin $I = 1$. The large quadruple moment coupling with the molecular rotation induces a hyperfine splitting of each rotational level (J) of HCN, in three hyperfine levels $F (= I + J)$ that vary between $|I - J|$ and $I + J$, except for $J = 0$ which only has a single level. The rotational transition $J = 1-0$ splits into three hyperfine transitions: $F = 0-1$, $F = 2-1$, and $F = 1-1$, separated by -7.1 km s^{-1} and $+4.9$ km s^{-1} from the central component $F = 2-1$, respectively (e.g., Ahrens et al. 2002; Goicoechea et al. 2022). The three hyperfine structure (HFS) lines of the $J = 1-0$ transition are usually well spectrally resolved by observations toward GMCs of the Galactic disk. In principle, this is convenient since the relative HCN $J = 1-0$ HFS line intensity ratios can provide the line opacity and the excitation temperature (T_{ex}), thus avoiding the need to observe isotopologues or multiple-J lines. However, only in the optically thin limit ($\tau \to 0$) are the relative HFS line intensity ratios equal to their relative line strengths (1:5:3), is the linewidth the same for the three HFS lines, and is T_{ex} exactly the same for the three HFS transitions, with $T_{ex} = T_k$ if local thermodynamic equilibrium (LTE) prevails. For optically thick lines, the line intensity ratios approach unity. Overall, the expected HCN $J = 1-0$ HFS line intensity ratio ranges are $R_{02} = W(F = 0-1)/W(F = 2-1) = [0.2, 1]$ and $R_{12} = W(F = 1-1)/W(F = 2-1) = [0.6, 1]$, where we define the integrated line intensity as $W = \int T_{mb}(v)\,dv$ (in K km s^{-1}). Interestingly, the observed interstellar line ratios are usually outside these ranges. This is called anomalous HCN emission.

Early studies of the HCN $J = 1-0$ emission from warm GMCs revealed anomalous $R_{12} < 0.6$ and $R_{02} \gtrsim 0.2$ ratios (Wannier et al. 1974; Clark et al. 1974; Gottlieb et al. 1975). Cold dark clouds show HFS anomalies toward embedded cores (Walmsley et al. 1982) and around them (Cernicharo et al. 1984a). More modern observations confirm the ubiquity of the HCN $J = 1-0$ HFS line intensity anomalies toward low- and high-mass star-forming cores (e.g., Fuller et al. 1991; Sohn et al. 2007; Loughnane et al. 2012; Magalhães et al. 2018).

Since the first detection of anomalous HCN $J = 1-0$ HFS emission, several theoretical studies have tried to explain its origin. Proposed explanations are as follows: radiative trapping combined with efficient collisional excitation from $J = 0$ to 2 (Kwan & Scoville 1975); HFS line overlap effects (Guilloteau & Baudry 1981; Daniel & Cernicharo 2008; Keto & Rybicki 2010); resonant scattering by low density halos (Gonzalez-Alfonso & Cernicharo 1993); and line overlaps together with electron-assisted weak collisional excitation (Goicoechea et al. 2022). A proper treatment of the HCN excitation in GMCs thus requires (i) the radiative effects induced by high line opacities and HFS line overlaps to be modeled and (ii) the HFS-resolved inelastic collision rate coefficients to be known. Recent developments include collisions of HCN with p-H_2, o-H_2, and e^- (Faure et al. 2007b; Faure & Lique 2012; Hernández Vera et al. 2017; Magalhães et al. 2018; Goicoechea et al. 2022).

Mapping large areas of nearby molecular clouds (a few hundred pc^2) in molecular rotational lines different than CO, and at the high spatial resolution (< 0.1 pc) needed to separate the emission from the different cloud component (cores, filaments, and ambient gas), has always been a difficult challenge. Recent surveys of GMCs, sensitive to the line emission from star-forming clumps and their environment, suggest that a significant fraction of the HCN $J = 1-0$ emission stems from low visual extinctions (A_V, i.e., from low density gas; e.g., Pety et al. 2017; Shimajiri et al. 2017; Kauffmann et al. 2017; Evans et al. 2020; Barnes et al. 2020; Tafalla et al. 2021; Patra et al. 2022; Dame & Lada 2023). Even the most translucent (Turner et al. 1997) and diffuse molecular clouds ($A_V < 1$ mag) show HCN $J = 1-0$ emission and absorption lines (Liszt & Lucas 2001; Godard et al. 2010) compatible with HCN abundances similar to those inferred in dense molecular clouds, 10^{-8}–10^{-9} (e.g., Blake et al. 1987).

Giant molecular clouds are illuminated by UV photons from nearby massive stars and by the interstellar radiation field. They are also bathed by cosmic ray particles. Ultraviolet radiation favors high electron abundances (the ionization fraction or χ_e) in the first $A_V \approx 2$–3 mag into the cloud (e.g., Hollenbach et al. 1991). In these cloud surface layers, most electrons arise from the photoionization of carbon atoms. Hence, $\chi_e \simeq \chi(C^+) \simeq$ a few 10^{-4} (Sofia et al. 2004). At intermediate cloud depths, from $A_V \approx 2$–3 to 4–5 mag depending on the gas density, cloud porosity to UV photons (Boisse 1990), and abundance of low ionization potential elements such as sulfur determine the ionization fraction (e.g., $\chi_e \simeq \chi(S^+) \simeq$ a few 10^{-5} in Orion A; Goicoechea & Cuadrado 2021). At much larger A_V, deeper inside the dense cores shielded from external UV radiation, χ_e is much lower, $\sim 10^{-7}$–10^{-8}. These χ_e values apply to GMCs in the disk of the galaxy exposed to standard cosmic ray ionization rates, $\zeta_{CR} = 10^{-17}$–10^{-16} s^{-1} (Guelin et al. 1982; Caselli et al. 1998; Goicoechea et al. 2009).

More than 45 yr ago, Dickinson et al. (1977) suggested that electron collisions contribute to the rotational excitation of very polar neutral molecules (see also Liszt 2012). These molecules have large cross sections for collisions with electrons (Faure et al. 2007b). This implies that the rate coefficients of inelastic collisions with electrons can be at least three orders of magnitude greater than those of collisions with H_2 and H. Hence, electron collisions contribute to, and even dominate, the excitation of these molecules when (i) χ_e is higher than the critical fractional abundance of electrons, $\chi_{cr}^*(e^-) = n_{cr}(e^-)/n_{cr}(H_2)$, and (ii) the gas density $n(H_2)$ is lower than the critical density for collisions with H_2, $n(H_2) < n_{cr}(H_2)$. For HCN $J = 1-0$, this implies
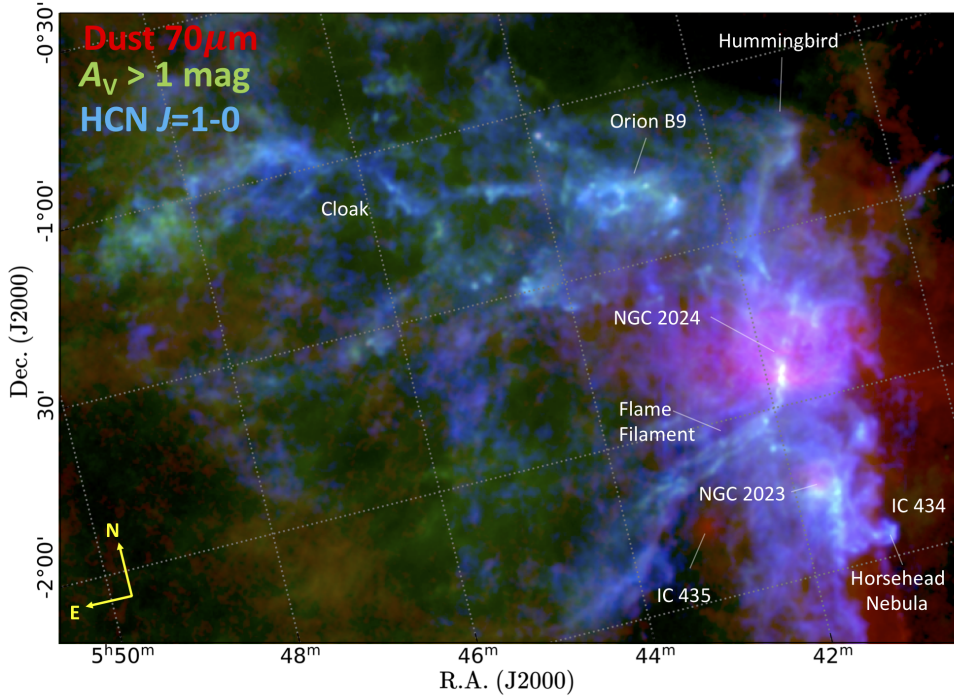
Fig. 1. Composite image of the ∼5 deg² area mapped in Orion B. Red color represents the PACS 70 µm emission tracing FUV-illuminated extended warm dust. Green color represents the cloud depth in magnitudes of visual extinction, $A_V \propto N(H_2)$. Blue color represents the HCN $J = 1-0$ line intensity. We note that outside the main filaments most of the HCN $J = 1-0$ emission is at $A_V < 4$ mag.

Table 1. Spectroscopic parameters of the lines studied in this work (from Endres et al. 2016, and references therein), critical densities for collisions with p-H₂ and electrons at 20 K (if LTE prevails, 99.82% of H₂ is in para form), and critical fractional abundance of electrons (see text).

Species	Transition	Frequency (GHz)	E_u/k_B (K)	A_{ul} (s⁻¹)	$n^{H_2}_{cr,u}$ ($T_k = 20$ K) (cm⁻³)	$n^e_{cr,u}$ ($T_k = 20$ K) (cm⁻³)	$\chi^*_{cr,e}$	Ref. collisional rates para-H₂, e⁻
HCN	$J = 1-0$	88.63185	4.25	2.41×10^{-5}	2.7×10^5	3.2	1.2×10^{-5}	a,b
HCN	$J = 2-1$	177.26122	12.76	2.31×10^{-4}	2.3×10^6	38	1.7×10^{-5}	
HCN	$J = 3-2$	265.88650	25.52	8.36×10^{-4}	5.8×10^6	168	2.9×10^{-5}	
HCN	$J = 4-3$	354.50548	42.53	2.05×10^{-3}	1.6×10^7	485	3.0×10^{-5}	
HNC	$J = 1-0$	90.66357	4.35	2.69×10^{-5}	7.0×10^4	3.6	5.2×10^{-5}	a,b
HNC	$J = 3-2$	271.98114	26.11	9.34×10^{-4}	2.2×10^6	191	8.6×10^{-5}	
HCO⁺	$J = 1-0$	89.18852	4.28	4.19×10^{-5}	4.5×10^4	2.0	4.4×10^{-5}	c,d
HCO⁺	$J = 2-1$	178.37506	12.84	4.02×10^{-4}	4.0×10^5	21	5.3×10^{-5}	
HCO⁺	$J = 3-2$	267.55763	25.68	1.45×10^{-3}	1.5×10^6	84	5.8×10^{-5}	
HCO⁺	$J = 4-3$	356.73422	42.80	3.57×10^{-3}	3.1×10^6	223	7.1×10^{-5}	
CO	$J = 1-0$	115.27120	5.53	7.20×10^{-8}	5.7×10^2	...	...	e
C⁰	$^3P_1$-$^3P_0$	492.16065	23.62	7.88×10^{-8}	5.5×10^2	410	7.0×10^{-1}	f,g

Notes. We define the critical density as the H₂ (or e^-) density at which A_{ul} equals the sum of all upward and downward collisional rates from the upper level. That is, $n_{cr} = A_{ul} / \sum_{i \neq u} \gamma_{ui}$. For collisions with electrons, we consider only dipole-allowed transitions. We define the critical fractional abundance of electrons as $\chi^*_{cr,e} = n^e_{cr} / n^{H_2}_{cr}$.
References. (a) Hernández Vera et al. (2017); (b) Faure et al. (2007b); (c) Denis-Alpizar et al. (2020); (d) Faure et al. (2007a, 2009); (e) Yang et al. (2010); (f) Schroder et al. (1991); (g) Johnson et al. (1987).

$\chi_e \gtrsim 10^{-5}$ and $n(H_2) \lesssim 10^5$ cm⁻³ (Dickinson et al. 1977; Liszt 2012; Goldsmith & Kauffmann 2017; Goicoechea et al. 2022). Table 1 lists the frequency, upper level energy, n_{cr}, and critical fractional abundance $\chi^*_{cr}(e^-)$ of the lines relevant to this work.

Galactic and extragalactic studies typically overlook the role of electron excitation (e.g., Yamada et al. 2007; Behrens et al. 2022). However, the ionization fraction in the interstellar medium (ISM) of galaxies can be very high because of enhanced cosmic ray ionization rates and X-ray fluxes driven by accretion processes in their nuclei (Lim et al. 2017). Mapping

nearby GMCs in our Galaxy offers a convenient template to spatially resolve and quantify the amount of low surface brightness HCN emission (affected by electron excitation) not directly associated with dense star-forming clumps. This emission component is usually not considered in extragalactic studies (e.g., Papadopoulos et al. 2014; Stephens et al. 2016).

Here we carry out a detailed analysis of the extended HCN $J = 1-0$ line emission, and that of related molecules, obtained in the framework of the large program Outstanding Radio-Imaging of Orion B (ORION-B) over 5 deg² (see Fig. 1

Table 2. Properties of the massive stars creating H II regions.

H II region	Spectral type	Distance[a] (pc)	Radius[b] (arcmin)
IC 434	O9.5V B	388 ± 1	42
NGC 2024	O9.5V	415	12
Around Alnitak	O9.7Ib+B0III C	290 ± 21	11
IC 435	B5V D	170 ± 37	3
NGC 2023	B1.5V C	360 ± 35	2.5

Notes. [a] Distance to the ionizing star (as in Pety et al. 2017). [b] Radius of the circles draw in Fig. 2b (as in Gaudel et al. 2023).

for an overview). These maps cover five times larger areas than those originally presented by Pety et al. (2017). We revisit the diagnostic power of the HCN $J = 1$–0 emission as a tracer of the dense molecular gas reservoir for star formation. This paper is organized as follows. In Sect. 2, we introduce the most relevant regions in Orion B as well as the observational dataset. In Sect. 3, we present and discuss the spatial distribution of different tracers. In Sect. 4, we analyze the extended HCN emission and derive gas physical conditions. In Sect. 5, we reassess the chemistry of HCN and HNC in FUV-illuminated gas. In Sect. 6, we discuss the relevance and properties of the low-density extended cloud component, we determine the dense gas mass conversion factor α(HCN), and discuss the $I_{FIR}-W$ scalings we find between different emission lines and FIR dust intensities. In Sect. 7, we summarize our findings and give our conclusions.

2. Observations

2.1. The Orion B GMC

Orion B, in the Orion complex, east of the Orion Belt stars, is one of the nearest GMCs (e.g., Anthony-Twarog 1982). Here we adopt a distance[1] of $d = 400$ pc. Orion B is a good template to study the star formation processes in the disk of a normal galaxy. This is an active but modest star-forming region (with a low SFR $\sim 1.6 \times 10^{-4}$ $M_\odot$ yr^{-1} and low star-formation efficiency, SFE $\sim 1\%$, e.g., Lada et al. 2010; Megeath et al. 2016; Orkisz et al. 2019) that contains thousands of dense molecular cores: starless, prestellar, and protostellar cores (e.g., Könyves et al. 2020). Massive star formation is highly concentrated in four main regions: NGC 2071 and NGC 2068 in the northeast, and NGC 2023 and NGC 2024 in the southwest. Table 2 summarizes the properties of the massive stars that create H II regions in the field. Figure 2b shows the position and extent of these H II regions (marked with circles). Orion B hosts a complex network of filaments. The main and longest filaments are the Flame and Hummingbird filaments, Orion B9, and the Cloak (Orkisz et al. 2019; Gaudel et al. 2023). Appendix A outlines the main properties of these regions.

2.2. ORION-B molecular line maps in the 3 mm band and spatial smoothing

The ORION-B project (PIs: J. Pety and M. Gerin) is a large program that uses the 30m telescope of the Institut de Radioastronomie Millimétrique (IRAM) to map a large fraction of the

Orion B molecular cloud (5 square-degrees, 18.1×13.7 pc^2). Observations were obtained using the EMIR090 receiver at $\sim 21''-28''$ resolution. The FTS backend provided a channel spacing of 195 kHz (0.5–0.7 km s^{-1} depending on the line frequency). The typical 1σ line sensitivity in these maps is ~ 100 mK per velocity resolution channel. The full field of view was covered in about 850 h by (on-the-fly) mapping rectangular tiles with a position angle of 14° in the Equatorial J2000 frame that follows the global morphology of the cloud. Data reduction was carried out using GILDAS[2]/CLASS and CUBE. This includes gridding of individual spectra to produce regularly sampled maps, at a common angular resolution of 30″, with pixels of 9″ size, about one third of the angular resolution of the telescope (half power beam width, HPBW). The projection center of the maps is located on the Horsehead photodissociation region (PDR) at 5h40m54.27s, -02°28′00.0″. We rotated the maps counter-clockwise by 14° around this center. Pety et al. (2017) presents a detailed description of the observing procedure and data reduction. Here we focus on a global analysis of the HCN $J = 1$–0 emission, and its relation to that of HNC, ^{12}CO, and HCO$^+$. Orion B shows three main velocity components at the local standard of rest (LSR) velocities ~ 2.5, ~ 6, and ~ 10 km s^{-1} (Gaudel et al. 2023). Here we obtained the line intensity maps (zero-order moment maps) integrating each line spectrum in the velocity ranges [−5, +25] km s^{-1} (for ^{12}CO and HCN $J = 1$–0 lines) and [0, +18] km s^{-1} (for HNC and HCO$^+$ $J = 1$–0). We refer to Gaudel et al. (2023) for a thorough analysis of the ^{13}CO and C^{18}O $J = 1$–0 maps and gas kinematics.

To match the resolution of the [C I] 492 GHz map (see next Section), and since we are interested in the faint and extended molecular emission, we spatially smoothed the original line maps to an angular resolution of $\sim 2'$ (~ 0.2 pc). This allows us to recover a significant fraction of low surface brightness line emission at large spatial scales. Spatial smoothing improves the root mean square (rms) to ~ 25 mK per velocity channel. Thus, it improves the detection limit and signal-to-noise ratio (S/N) of the faint and extended emission. Figure 2 shows the spatially smoothed maps.
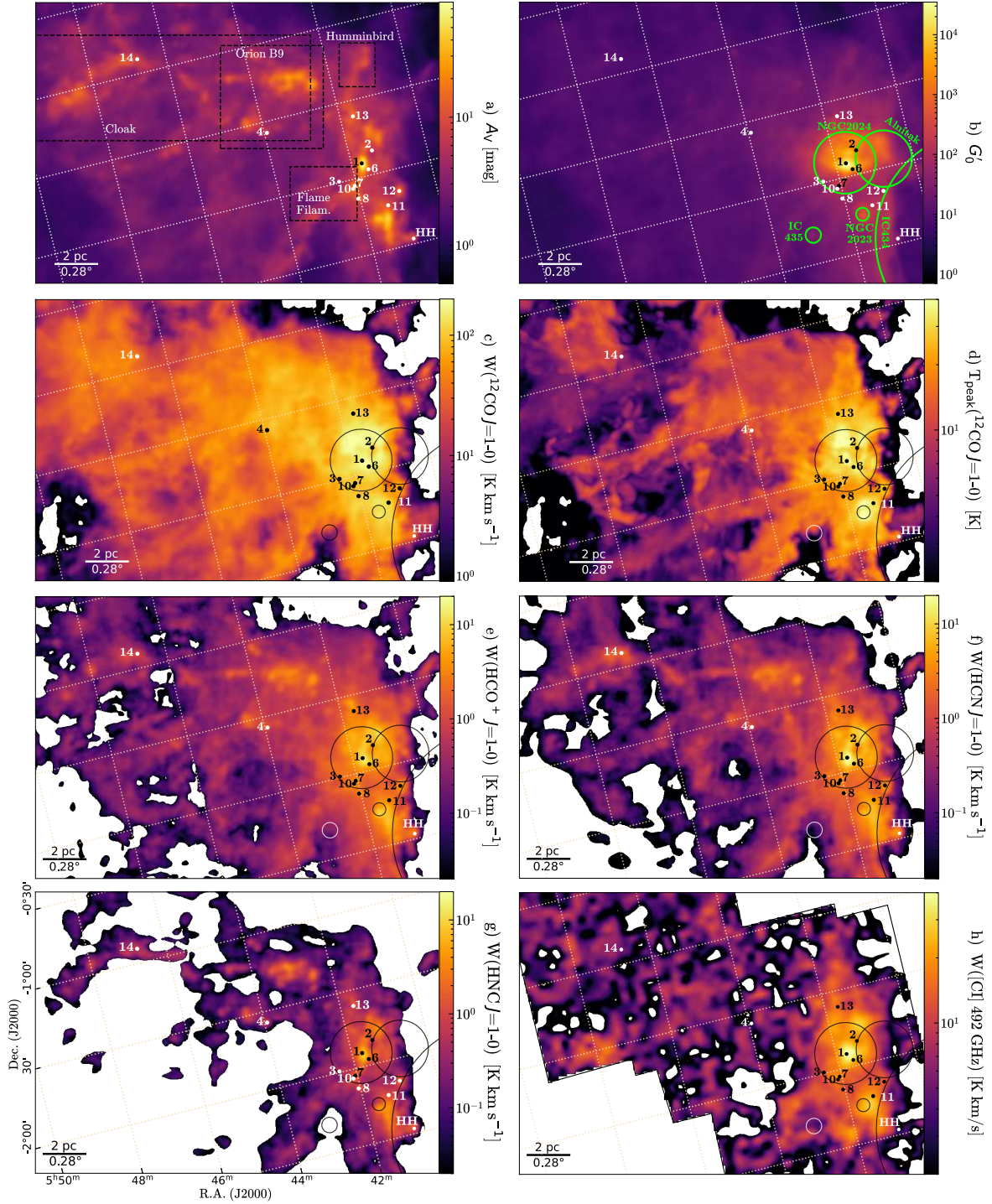
2.3. Wide-field [C I] 492 GHz map

We complement our molecular line maps with an existing wide-field map of the ground-state fine structure line ($^3P_1$–$^3P_1$) of neutral atomic carbon, the [C I] 492 GHz line, obtained with the Mount Fuji submillimeter-wave telescope. These observations reached a rms noise of ~ 0.45 K per 1.0 km s^{-1} velocity channel (Ikeda et al. 2002). The angular resolution is $\sim 2'$. Figure 2h shows the [C I] 492 GHz line integrated intensity map in the LSR velocity range [+3, +14] km s^{-1}.

2.4. Pointed observations of rotationally excited lines

In addition to the molecular $J = 1$–0 line maps, we observed several cloud positions (see Table 3 for the exact coordinates and details) in rotationally excited lines ($J = 2$–1, 3–2, and 4–3). We obtained these observations also with the IRAM-30m telescope. We observed 14 positions representative of different cloud environments: cold and dense cores, filaments and their surroundings, PDRs adjacent to H II regions and cloud environment. Figure 2 shows the location of these positions. We used the EMIR receivers E150 (at 2 mm), E230 (at 1.3 mm), and E330 (at

---

[1] Interferometric observations of the σ Ori system provides a distance of ~ 388 pc (Schaefer et al. 2016). Recent determinations using *Gaia* also estimate ~ 400 pc (e.g., Zucker et al. 2019; Rezaei Kh. et al. 2020).

[2] See https://www.iram.fr/IRAMFR/GILDAS

Fig. 2. Maps of Orion B in different tracers. (a) Visual extinction A_V, (b) Approximate FUV field, G_0' (see text), (d) ^{12}CO $J = 1$–0 peak temperature (in K). (c) and (e) to (h) ^{12}CO, HCO$^+$, HCN, HNC $J = 1$–0, and [C I] 492 GHz (from Ikeda et al. 2002) integrated line intensity maps (in K km s^{-1}) spatially smoothed to an angular resolution of $\sim$2′. Dashed black boxes mark the Cloak, Orion B9, Hummingbird, and Flame filament. Circles mark the extension of the H II regions in NGC 2024, NGC 2023, IC 434, IC 435, and around the star Alnitak. The HH dot marks the position of the Horsehead PDR, the projection center of the maps.

0.9 mm) in combination with the FTS backend (195 kHz spectral resolution). The HPBW varies as ≈ 2460/Freq[GHz][3]. For the E1, E2, and E3 bands, the HPBW is $\sim$14″, $\sim$9″, and $\sim$7″, respectively. We carried out dualband observations combining the E1 and E3 bands, during December 2021 and 2022, under excellent

winter conditions ($\sim$1–4 mm of precipitable water vapor, pwv). We obtained the E2 band observations during three different sessions: (i) December 2021: pwv<4 mm (positions #1, #2, #4, #10, and #11), (ii) March 2022: pwv>6 mm (#3 and #7), (iii) May 2022: pwv $\sim$ 5 mm (#6, #8, #12, #13, and #14).

In order to compare line intensities at roughly the same 30″ resolution, we averaged small raster maps centered around

---

[3] See https://publicwiki.iram.es/Iram30mEfficiencies

Table 3. Representative environments of our pointed observations.

Pos.	(RA, Dec) [h:m:s, °:′:″]	Environment
#1	5:41:44.4, −1:54:45.4	Protostellar core NGC 2024(FIR-4)
#2	5:41:24.1, −1:50:49.5	Irradiated prestellar core (NGC 2024 bubble)
#3	5:42:25.3, −1:59:33.2	Starless core
#4	5:43:55.9, −1:34:21.4	Orion B9 (south)
HH PDR	5:40:53.9, −2:28:00.0	Warm PDR
#6	5:41:36.5, −1:57:38.5	NGC 2024 south: dust ridge
#7	5:42:03.2, −2:02:35.8	Prestellar core in the Flame Filament
#8	5:42:02.9, −2:07:45.2	Protostellar core (YSO)
HH Core	5:40:55.6, −2:27:38.0	DCO$^+$ emission peak
#10	5:42:06.8, −2:03:33.5	#7 surroundings
#11	5:41:20.2, −2:13:03.6	NGC 2023 north surroundings
#12	5:40:58.1, −2:08:41.9	Prestellar core
#13	5:41:40.0, −1:36:13.6	Filament surroundings
#14	5:46:43.7, −0:54:22.6	Cloak

Notes. We sort these positions in decreasing order of $T_{\rm rot}$(HCN) (see also Table 7).

each target position and approximately covering the area of a 30″ diameter disk (Fig. F.1 shows our pointing strategy). The total integration time per raster-map was ~1 h, including on and off integrations. The achieved rms noises of these observations, merging all observed positions of a given raster-map, are ~22 mK ($J = 2$–1), ~20 mK ($J = 3$–2), and ~30 mK ($J = 4$–3), per 0.5 km s^{-1} velocity channel. Table F.1 summarizes the frequency ranges observed with each backend, the HPBW, and the number of pointings of each raster map.

We analyzed these pointed observations with CLASS. We subtracted baselines fitting line-free channels with first or second order polynomial functions. We converted the intensity scale from antenna temperature, $T_{\rm A}^*$, to main-beam temperature, $T_{\rm mb}$, as $T_{\rm mb} = T_{\rm A}^* \times F_{\rm eff}/B_{\rm eff}$, where $F_{\rm eff}$ and $B_{\rm eff}$ are the forward and beam efficiencies[3]. Figure 3 shows a summary of the spectra. Figures G.1 and G.2 show the complete dataset.

2.5. Herschel $T_{\rm d}$, $A_{\rm V}$, and G_0' maps

In addition to the molecular and atomic line maps, we also make use of the dust temperature ($T_{\rm d}$) and 850 μm dust opacity ($\tau_{850\,\mu\rm m}$) maps fitted by Lombardi et al. (2014) on a combination of *Planck* and *Herschel* data from the *Herschel* Gould Belt Survey (HGBS) (André et al. 2010). In Appendix C we provide additional details on these maps. We estimated the (line of sight) visual extinction from the $\tau_{850\,\mu\rm m}$ dust opacity map following Pety et al. (2017):

$$A_{\rm V} = 2.7 \times 10^4\, \tau_{850\,\mu\rm m}\ {\rm [mag]}. \tag{1}$$

By taking the $\tau_{850\,\mu\rm m}$ error map of Lombardi et al. (2014), we determine that the mean 5σ error of the $A_{\rm V}$ map is about 0.8 mag.

This value is slightly above our molecular line detection threshold ($A_{\rm V} \simeq 0.3$–0.4 mag, see Fig. 4). Thus, we caution that one can probably not trust any $A_{\rm V}$−W trend below $A_{\rm V} \simeq 0.8$ mag. For each line of sight, we determined the FIR surface brightness, $I_{\rm FIR}$, from spectral energy distributions (SED) fits, by integrating:

$$I_{\rm FIR} = \int I_\nu\, d\nu = \int B_\nu(T_{\rm d})[1 - {\rm e}^{-\tau_\nu}]\, d\nu, \tag{2}$$

from $\lambda = 40$ to 500 μm. In this expression, $B_\nu(T_{\rm d})$ is the blackbody function, $\tau_\nu = \tau_{\nu_{850\,\mu\rm m}}(\nu/\nu_{850\,\mu\rm m})^\beta$ is the frequency-dependent dust opacity (we adopt the same emissivity exponent as Lombardi et al. 2014), and $T_{\rm d}$ is an effective dust temperature.

We estimate the strength of the far-UV (FUV) radiation field ($6 < E < 13.6$ eV), in Habing units (G_0'), from $I_{\rm FIR}$ using:

$$G_0' = \frac{1}{2} \frac{I_{\rm FIR}\ [{\rm erg\ s^{-1}\ cm^{-2}\ sr^{-1}}]}{1.3 \times 10^{-4}}. \tag{3}$$

In this expression we assume that the FIR continuum emission arises from dust grains heated by stellar FUV and visible photons (Hollenbach & Tielens 1999). We use the notation G_0' (meaning approximate G_0) because this expression is precise for a face-on PDR (e.g., it is valid for NGC 2024 and NGC 2023). Because of their edge-on geometry, Eq. (3) is less accurate for the Horsehead PDR and IC 434 front (although it provides the expected G_0 within factors of a few). In addition, Eq. (3) provides an upper limit to the actual G_0 toward embedded star-forming cores (at high $A_{\rm V}$). These cores emit significant non-PDR FIR dust continuum. To directly compare our line emission maps with the $A_{\rm V}$, G_0', and $I_{\rm FIR}$ maps, we also spatially smoothed these SED-derived maps to an angular resolution of 120″ (Figs. 2a and b).

3. Results

3.1. Spatial distribution of the HCN $J = 1$–0 emission, relation to other chemical species, and $A_{\rm V}$ and G_0' maps

Figure 1 shows a composite RGB image of the mapped area (~ 5 deg^2 = 250 pc^2). This image shows extended HCN $J = 1$–0 emission far from the main dense gas filaments (where $A_{\rm V} > 8$ mag), as well as very extended 70 μm dust emission (e.g., André et al. 2010) from FUV-illuminated warm grains. Figure 2 shows the spatial distribution of the ^{12}CO, HCO$^+$, HCN, and HNC $J = 1$–0 integrated line intensities, W (also dubbed line surface brightness) at a common resolution of ~2′ (~0.2 pc, thus matching the angular resolution of the [C I] 492 GHz map in Fig. 2g). W(HCN $J = 1$–0) refers the sum of the three HFS components. The emission from all species peaks toward NGC 2024. The last column in Table 4 shows that spatial smoothing (increasing the line sensitivity at the expense of lower spatial resolution) allows us to detect HCN and HNC $J = 1$–0 emission from a cloud area nearly four times bigger than from maps at ~30″ resolution. For CO $J = 1$–0 (very extended emission) the recovered area is smaller. CO $J = 1$–0 shows the most widespread emission. It traces the most extended and translucent gas, arising from 90% of the mapped area. HCO$^+$ and HCN $J = 1$–0 are the next molecular lines showing the most extended distribution, 73% and 60% of the total observed area, respectively. On the other hand, HNC $J = 1$–0 shows a similar distribution as C^{18}O $J = 1$–0 (Gaudel et al. 2023).

Table 4 provides the total line luminosity ($L_{\rm line}$) from the mapped area in $L_\odot$ units. $L_{\rm line}$ is the power emitted through a
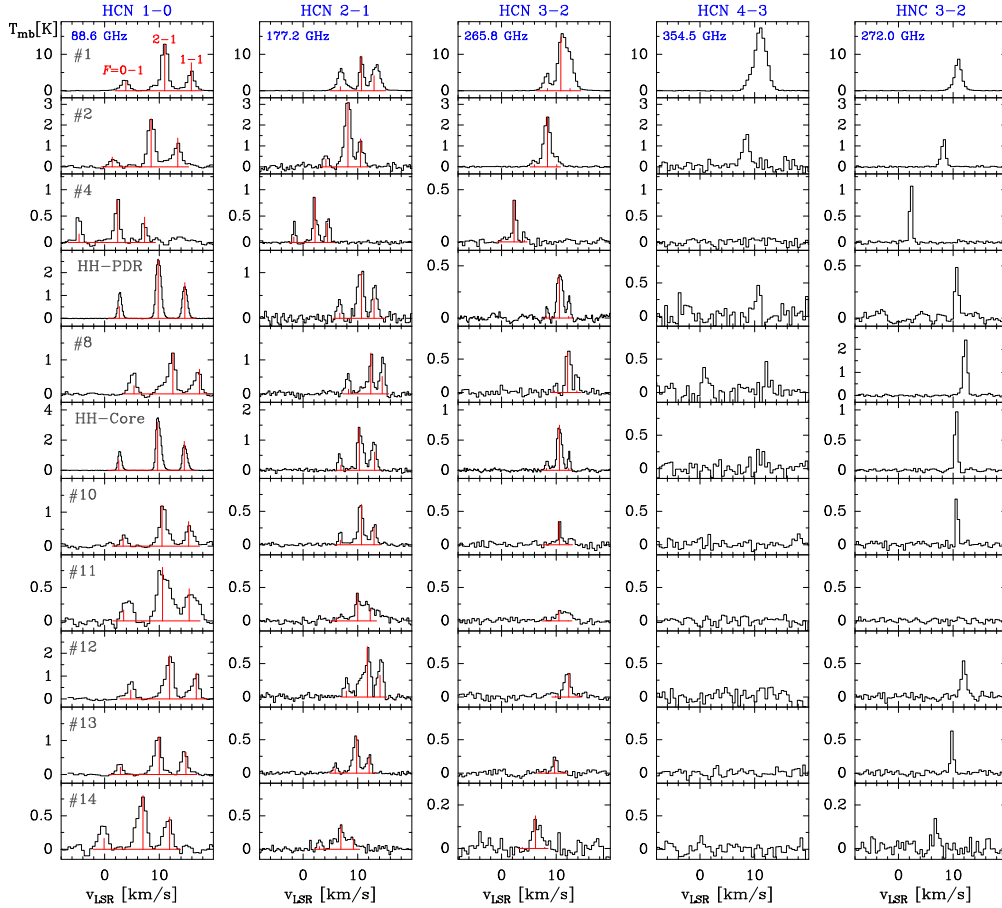
Fig. 3. Selection of HCN $J = 1–0$ to 4–3, and HNC $J = 3–2$ line detections toward representative cloud environments in Orion B. Red lines show the expected relative HFS line intensities in the LTE and optically thin limit.

Table 4. Characteristics of the molecular line emission over $5\,\mathrm{deg}^2$ of Orion B.

(1) Line	(2) Intensity (W_{average}) (K km s^{-1})	(3) $T_{\mathrm{mb}}^{\mathrm{peak}}$ [K]	(4) Luminosity (L') (K km s^{-1}pc^2)	(5) Luminosity (L) ($L_\odot$)	(6) α (molecule) ($M_\odot$/(K km s^{-1}pc^2))	(7) (8) A_{cov} [%]		(9) $A_{\mathrm{cov}}^{120''}/A_{\mathrm{cov}}^{30''}$
(average spectrum)						30"	120"	
^{12}CO $J=1–0$	30.6	5.4	7300	1.7×10^0	0.43	78	92	1.2
HCO$^+$ $J=1–0$	0.52	0.14	120	1.4×10^{-2}	25	21	73	3.5
HCN $J=1–0$	0.46	0.06	110	1.2×10^{-2}	29	16	60	3.8
HNC $J=1–0$	0.15	0.04	40	4.1×10^{-3}	88	9	33	3.8

Notes. (2), (3): Line intensity and line peak temperature of the average spectrum in the mapped area. (4) and (5): Line luminosity in K km s^{-1} pc^2 and $L_\odot$ units. (6) Dense gas mass M_{dg} to line luminosity ratio, where $M_{\mathrm{dg}} = 3.1 \times 10^3\,M_\odot$ (mass at $A_V > 8$ mag). (7) and (8): Percentage of the mapped area with 3σ line detections. (9): Ratio of cloud areas with 3σ line detection after spatial smoothing.

given line. It also provides L'_{line} (in units of K km s^{-1} pc^2), with:

$$L'_{\mathrm{line}} = d^2 \int T_{\mathrm{mb}}(v)\,dv\,d\Omega = W_{\mathrm{average}} \times A, \qquad (4)$$

where Ω is the solid angle subtended by the source area and W_{average} is the average spectrum over the mapped area A. This last quantity is commonly used to express mass conversion factors (see Sect. 6.3) and it is also frequently used in the extragalactic context (e.g., Gao & Solomon 2004a; Carilli & Walter 2013). The ^{12}CO $J=1–0$ luminosity over the mapped area,

$\sim 1.7\,L_\odot$, is more than a hundred times higher than $L_{\mathrm{HCO^+\,1–0}}$ and $L_{\mathrm{HCN\,1–0}}$.

Figures 2a and b show maps of visual extinction (A_V) and the approximate strength of the FUV radiation field G'_0 (see Sect. 2.5). Table 5 summarizes the median, average, and standard deviation values of the SED-derived parameters. The star-forming cores at the center of the NGC 2024 have the highest A_V values, with a secondary peak toward NGC 2023 star-forming cores. The highest values of G'_0 correspond to cloud areas in the vicinity of the H II regions NGC 2024 ($G'_0 \approx 10^4$), with a contribution from the neighbor H II region created by Alnitak

Table 5. SED derived parameters from 5 deg^2 maps of Orion B.

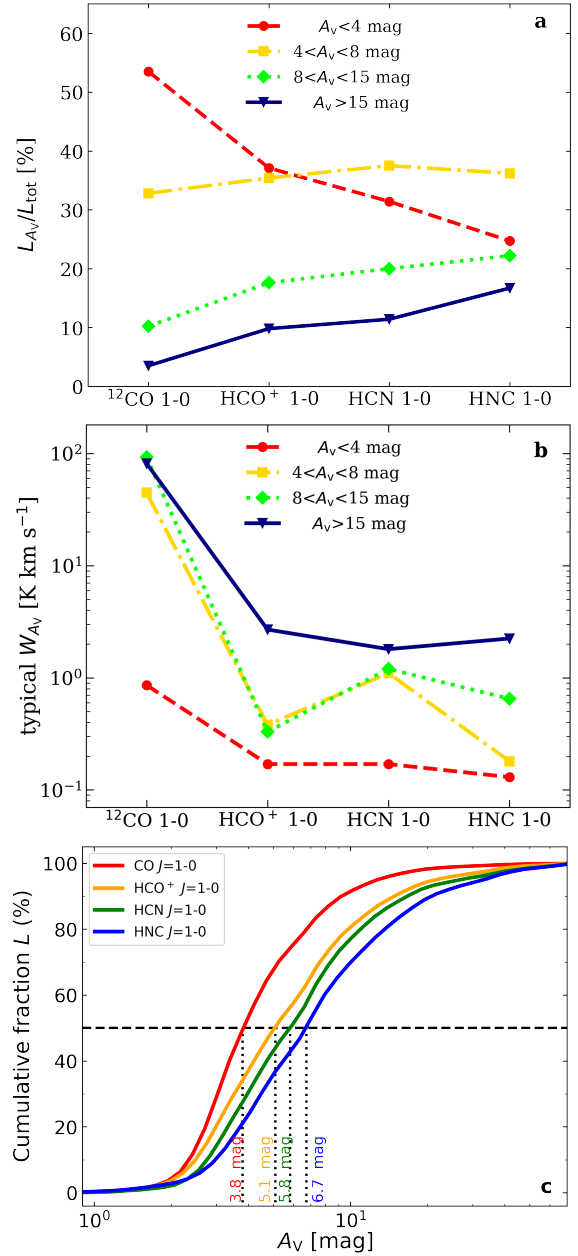| Parameter	Median	Mean value	Std. dev.	Units
T_d	18	20	4	K
A_V	2.6	3.2	3	mag
I_{FIR}	0.002	0.02	0.3	erg s^{-1} cm^{-2} sr^{-1}
G'_0	9	70	1000	Habing
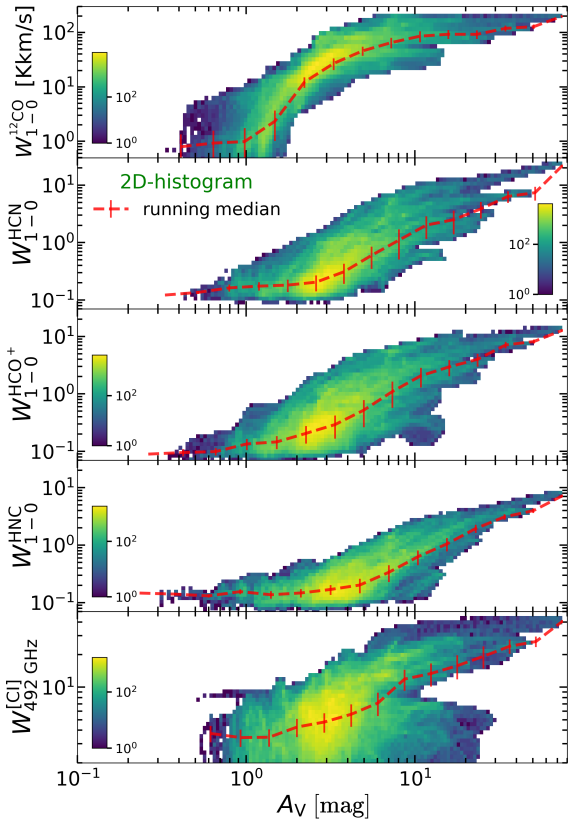
Fig. 4. Distribution of ^{12}CO, HCN, HCO$^+$, HNC $J = 1–0$, and [C I] 492 GHz line intensities as a function of A_V. The dashed red lines show the running median (median values of the line intensity within equally spaced log A_V bins). Error bars show the line intensity dispersion. We note that the 5σ error of A_V is $\simeq 0.8$ mag. Thus, one cannot trust any trend below this threshold.

Fig. 5. Line emission properties as a function of A_V. (a) Fractions (in %) of line luminosities emitted in each A_V mask. (b) Typical (the mode) line intensity in each A_V mask. (c) Cumulative line luminosity.

star ($G'_0 \approx 10^3$), NGC 2023 ($G'_0 \approx 10^3$), IC 435 ($G'_0 \approx 10^2$), and the ionization front IC 434 ($G'_0 \approx$ a few 10^2) that includes the iconic Horsehead Nebula. On the other hand, the easter part of the cloud shows low surface brightness I_{FIR} emission compatible with G'_0 of a few to $\simeq 10$. The median G'_0 in the mapped region is 9.

Figure 4 shows 2D histograms of the CO, HCN, HCO$^+$, HNC $J = 1−0$, and [C I] 492 GHz integrated line intensities as function of the visual extinction into the cloud[4]. The running median of the HCN $J = 1−0$ emission increases with extinction at $A_V > 3$ mag, whereas the running median of the HNC $J = 1−0$ emission shows a similar change of tendency but at higher extinction depths $A_V > 5$ mag. As HCN, the largest number of HCO$^+$ $J = 1−0$ and [C I] 492 GHz line detections in the map occur at $A_V \simeq 3$ mag. Atomic carbon, however, shows an approximate bimodal behavior with A_V (it shows both bright and faint

emission at high A_V). Indeed, while A_V is the total visual extinction along each line of sight, we expect that in many instances the [C I] 492 GHz emission mostly arises from cloud rims close to the C^0/CO transition (e.g., Hollenbach et al. 1991). On the other hand, lines of sight of large A_V and very bright [C I] 492 GHz emission (such as NGC 2024) probably trace FUV-illuminated surfaces of multiple dense cores and PDRs along the line of sight.

Following Pety et al. (2017), Fig. 5a shows the fraction of total L_{line} within a set of four visual extinction masks. The mask with $A_V > 15$ mag (~1% of the total mapped area) represents the highest density gas associated with dense cores. The mask within the A_V range 8–15 mag (~3% of the mapped area) is right above the extinction threshold above which the vast majority of prestellar cores are found in molecular clouds (e.g., Lada 1992;

---

[4] Section 6.4 discusses the relation between these lines and I_{FIR}.

Lada et al. 2010; Wu et al. 2010; Evans et al. 2020). Below this threshold, we create two masks to differentiate the emission associated with A_V below 4 mag (translucent and PDR gas; ~80% of the mapped area) and $4 < A_V < 8$ mag (intermediate cloud depths representing ~16% of the mapped area). We find that more than half of the total CO $J = 1–0$ intensity arises from the lowest extinction mask $A_V < 4$ mag. Interestingly, about a 30% of the total HCN $J = 1–0$ emission arises from gas also at $A_V < 4$ mag. Most of the HCN and HNC $J = 1–0$ emission arises from regions at visual extinctions between 4 and 8 mag, and only 10% of the HCN emission arises from regions at very high visual extinctions, $A_V > 15$ mag. Likewise, the HCN and HNC 2D histograms peak at A_V lower than 3 mag (HCN) and 5 mag (HNC). This contrasts with the N_2H^+ $J = 1–0$ emission, which arises from cold and dense gas shielded from FUV radiation at $A_V > 15$ mag (see Pety et al. 2017). For each molecular line, Fig. 5b shows the typical (the statistical mode) intensity W toward each of the four extinction masks. The CO $J = 1–0$ emission is bright (~1 K km s^{-1}) even at $A_V < 4$ mag, and very bright (> 10 K km s^{-1}) toward all the other masks (although optically thick).

The typical HCN, HNC, and HCO$^+$ $J = 1–0$ line intensities are above 1 K km s^{-1} for $A_V > 15$ mag (dense gas). For lower A_V, the lines are fainter but detectable. Since the translucent gas spans much larger areas than the dense gas (96% of the mapped cloud is $A_V < 8$ mag, 80% at $A_V < 3$ mag), in many instances it is the widespread and faint extended emission that dominates the total luminosity. We stress that ~70% of the HCN $J = 1–0$ line luminosity in Orion B arises from gas at $A_V < 8$ mag (and 50% of the FIR dust luminosity). Table 4 summarizes the line intensities and line luminosities over the mapped area.

Figure 5c shows the cumulative fractions of the integrated intensities for CO, HCO$^+$, HCN, HNC $J = 1–0$ as a function of A_V. The cumulative distributions are different for each species. We define the visual extinction that contains 50% of the total integrated line intensity as the characteristic A_V, such as $W(A_V < A_V^{char}) = 50\%$ (e.g., Barnes et al. 2020). We find that the characteristic A_V^{char} for CO $J = 1–0$ is 3.8 mag, which implies that 50% of the CO total intensity arises from gas below $A_V = 3.8$ mag. For HCO$^+$, HCN, and HNC $J = 1–0$ lines, we find A_V^{char} of 5.0, 5.8, and 6.7 mag, respectively. These values agree with recent studies of the star-forming regions Orion A and W49 (Kauffmann et al. 2017; Barnes et al. 2020).

3.2. HCN/CO, HCN/HNC, HCN/HCO$^+$, and [C I]/CO line intensity ratio maps

The spatial distribution of the HCN $J = 1–0$ line emission compared to that of other molecules provides information about the origin and the physical conditions of the HCN-emitting gas. Figure 6 shows the HCN/^{12}CO $J = 1–0$, HCN/HNC $J = 1–0$, and HCN/HCO$^+$ $J = 1–0$ integrated line intensity ratios. We generated these maps by taking only line signals above 3σ for each species (i.e., we show regions where the emission from both species spatially coexist along the line of sight). In addition, Fig. 6d shows a map of the [C I] 492 GHz/CO $J = 1–0$ integrated line intensity ratio[5]). Table 6 summarizes the average and median line intensity ratios in the mapped region.

– HCN/CO $J = 1–0$: The average line intensity ratio is 0.015, with a standard deviation of 0.023. In the inner regions of the cloud, close to the Cloak, Orion B9, Hummingbird, and Flame

Table 6. Statistics of 5 deg^2 line intensity ratio maps shown in Fig. 6.

Line intensity ratio	Median	Average	Std	$\rho(G_0')^{(\dagger)}$
HCN/CO $J = 1–0$	0.011	0.015	0.023	0.4
HCN/HNC $J = 1–0$	2.7	3.1	1.2	0.6
HCN/HCO$^+$ $J = 1–0$	0.9	0.88	0.4	0.2
[C I]/CO $J = 1–0$	0.15	0.20	0.26	–0.3

Notes. $^{(\dagger)}\rho(G_0')$ is the Spearman correlation rank with the G_0' map. See also Fig. B.2.

filaments, the ratio increases with A_V (shown in contours). We also find high line intensity ratios (~ 0.1) in the FUV-illuminated cloud edges (see discussion in Sect. 6.2).

– HCN/HNC $J = 1–0$: The average line intensity ratio is 3.1, with a standard deviation of 1.2. The lowest ratios, ~0.5–0.9, appear in cold and low I_{FIR} regions such as the Cloak and Orion B9.

– HCN/HCO$^+$ $J = 1–0$: The average line intensity ratio is 0.9, with a standard deviation of 0.4. In general, this line ratio displays small variations across the cloud. The Cloak, the center of NGC 2024, the Flame Filament, and the Horsehead show a line intensity ratio above one (reddish areas in Fig. 6c). All these regions host starless and prestellar cores (Könyves et al. 2020).

– [C I] 492 GHz/CO $J = 1–0$: The average line intensity ratio is 0.20, with a standard deviation of 0.26. In PDR gas, this ratio is roughly inversely proportional to the gas density (see e.g., Kaufman et al. 1999). We find the highest ratios, above one, toward the FUV-illuminated edges of the cloud.

We also investigate the possible spatial correlations of the above line intensity ratios with the SED derived parameters G_0', T_d, T_{peak}(CO), and A_V. Only the HCN/HNC $J = 1–0$ line intensity map shows a (weak) monotonic correlation with G_0' (Spearman correlation rank of 0.6; see Table 6). This spatial correlation is not linear (the Pearson correlation rank is 0.5 in log-log scale and 0.008 in linear scale) but suggests a connection between the HCN/HNC abundance ratio and the FUV radiation field. Figures B.1 and B.2 show 2D histograms of the studied line intensity ratios as function a of A_V and I_{FIR}, respectively.

4. HCN excitation, radiative transfer models, and gas physical conditions

In this section we analyze the large scale HCN $J = 1–0$ emission in detail. We, (i) derive excitation temperatures (T_{ex}) and HCN column densities, N(HCN), using the LTE-HFS fitting method, (ii) analyze the anomalous HCN $J = 1–0$ HFS emission, (iii) determine the physical conditions of the widespread and extended HCN $J = 1–0$ emitting gas, and (iv) derive rotational temperatures, T_{rot}, and N(HCN) in a sample of representative positions observed in rotationally excited HCN and H^{13}CN lines. In order to determine all these parameters at the highest possible spatial resolution, throughout all this section we make use of maps and pointed observations at an effective 30$''$ resolution (~0.06 pc).

4.1. HCN column density and T_{ex} using the LTE-HFS method

Firstly, we determine T_{ex} ($J = 1–0$) and the opacity-corrected column density $N^{\tau,corr}$(HCN) by applying the LTE-HFS fitting method in CLASS[2] (Appendix D.1). This method uses as input the

---

[5] To obtain the [C I] 492 GHz/CO $J = 1–0$ line ratio with line intensities in erg cm^{-2} s^{-1} sr^{-1} one has to multiply by (492 GHz/115 GHz)$^3 \simeq 78$.
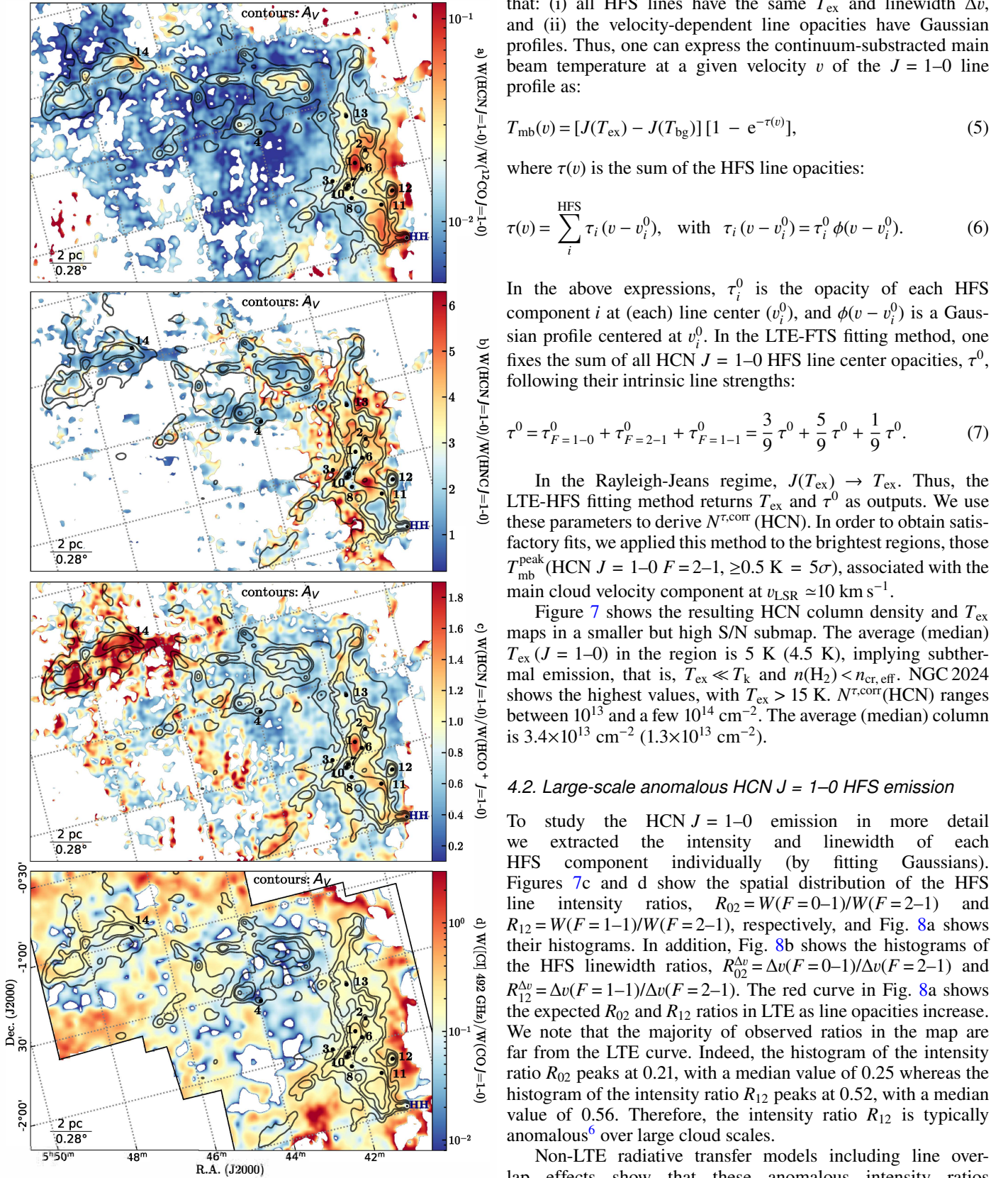
Fig. 6. Line intensity ratio maps. Contours show A_V = 4, 6, 8, and 15 mag.

line separations and 1:5:3 intrinsic line strengths of the J = 1–0 HFS components. The LTE-HFS fitting method assumes

that: (i) all HFS lines have the same T_{ex} and linewidth Δv, and (ii) the velocity-dependent line opacities have Gaussian profiles. Thus, one can express the continuum-substracted main beam temperature at a given velocity v of the J = 1–0 line profile as:

$$T_{mb}(v) = [J(T_{ex}) - J(T_{bg})] \, [1 - e^{-\tau(v)}], \tag{5}$$

where $\tau(v)$ is the sum of the HFS line opacities:

$$\tau(v) = \sum_i^{HFS} \tau_i \, (v - v_i^0), \quad \text{with} \quad \tau_i \, (v - v_i^0) = \tau_i^0 \, \phi(v - v_i^0). \tag{6}$$

In the above expressions, τ_i^0 is the opacity of each HFS component i at (each) line center (v_i^0), and $\phi(v - v_i^0)$ is a Gaussian profile centered at v_i^0. In the LTE-FTS fitting method, one fixes the sum of all HCN J = 1–0 HFS line center opacities, τ^0, following their intrinsic line strengths:

$$\tau^0 = \tau_{F=1-0}^0 + \tau_{F=2-1}^0 + \tau_{F=1-1}^0 = \frac{3}{9}\tau^0 + \frac{5}{9}\tau^0 + \frac{1}{9}\tau^0. \tag{7}$$

In the Rayleigh-Jeans regime, $J(T_{ex}) \rightarrow T_{ex}$. Thus, the LTE-HFS fitting method returns T_{ex} and τ^0 as outputs. We use these parameters to derive $N^{\tau,corr}$ (HCN). In order to obtain satisfactory fits, we applied this method to the brightest regions, those T_{mb}^{peak}(HCN J = 1–0 F = 2–1, ≥0.5 K = 5σ), associated with the main cloud velocity component at $v_{LSR} \simeq 10$ km s^{-1}.

Figure 7 shows the resulting HCN column density and T_{ex} maps in a smaller but high S/N submap. The average (median) T_{ex} (J = 1–0) in the region is 5 K (4.5 K), implying subthermal emission, that is, $T_{ex} \ll T_k$ and $n(H_2) < n_{cr, eff}$. NGC 2024 shows the highest values, with $T_{ex} > 15$ K. $N^{\tau,corr}$(HCN) ranges between 10^{13} and a few 10^{14} cm^{-2}. The average (median) column is 3.4×10^{13} cm^{-2} (1.3×10^{13} cm^{-2}).

4.2. Large-scale anomalous HCN J = 1–0 HFS emission

To study the HCN J = 1–0 emission in more detail we extracted the intensity and linewidth of each HFS component individually (by fitting Gaussians). Figures 7c and d show the spatial distribution of the HFS line intensity ratios, $R_{02} = W(F = 0–1)/W(F = 2–1)$ and $R_{12} = W(F = 1–1)/W(F = 2–1)$, respectively, and Fig. 8a shows their histograms. In addition, Fig. 8b shows the histograms of the HFS linewidth ratios, $R_{02}^{\Delta v} = \Delta v(F = 0–1)/\Delta v(F = 2–1)$ and $R_{12}^{\Delta v} = \Delta v(F = 1–1)/\Delta v(F = 2–1)$. The red curve in Fig. 8a shows the expected R_{02} and R_{12} ratios in LTE as line opacities increase. We note that the majority of observed ratios in the map are far from the LTE curve. Indeed, the histogram of the intensity ratio R_{02} peaks at 0.21, with a median value of 0.25 whereas the histogram of the intensity ratio R_{12} peaks at 0.52, with a median value of 0.56. Therefore, the intensity ratio R_{12} is typically anomalous[6] over large cloud scales.

Non-LTE radiative transfer models including line overlap effects show that these anomalous intensity ratios imply that lines are optically thick and that a single T_{ex} does not represent the excitation of these HFS levels

---

[6] We recall that the range of possible HFS line intensity ratios in LTE are $R_{02} = [0.2, 1]$ and $R_{12} = [0.6, 1]$. Outside these ranges, HFS ratios are called anomalous (and very anomalous if $R_{02} < 0.2$ and $R_{12} < 0.6$). Only in LTE, HFS lines have the same T_{ex} and same linewidths, thus $R^{\Delta v} = 1$.
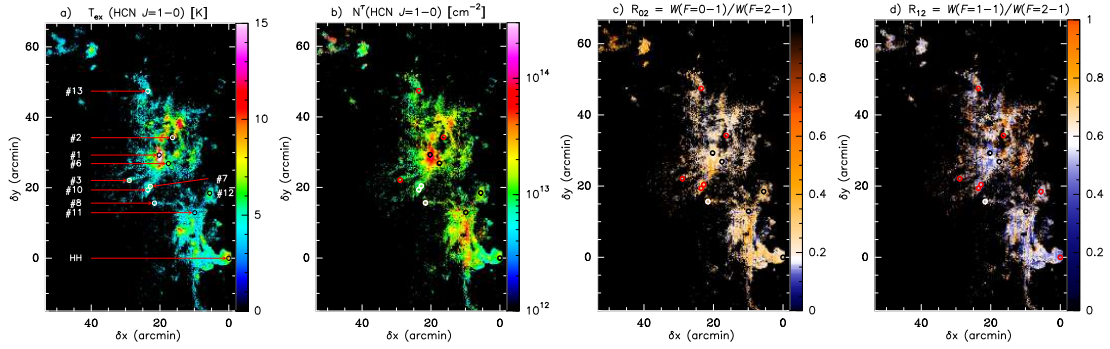
**Fig. 7.** Spatial distribution of T_{ex}(HCN $J=1$–0) and N(HCN) estimated from LTE-HFS fits, and maps of HCN $J=1$–0 HFS intensity ratios. (a) T_{ex}(HCN $J=1$–0). (b) Opacity-corrected column densities N(HCN). (c) and (d) R_{02} and R_{12} (white color corresponds to non-anomalous ratios).
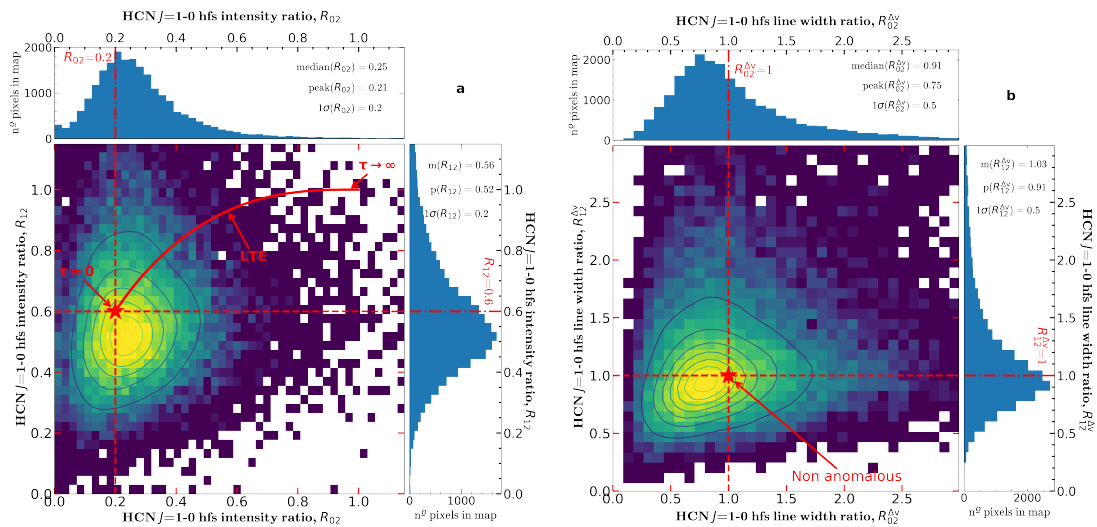
Fig. 8. Histograms of HCN $J=1$–0 HFS (a) Line intensity ratios, and (b) Line-width ratios observed in Orion B. R_{02} stands for $W(F=0$–$1)/W(F=2$–$1)$ and R_{12} stands for $W(F=1$–$1)/W(F=2$–$1)$. The red curve in panel (a) shows the expected LTE ratios as line opacities increase. The red star marks the non-anomalous ratios in the optically thin limit $\tau \to 0$ (1σ is the standard deviation relative to the mean line ratios).
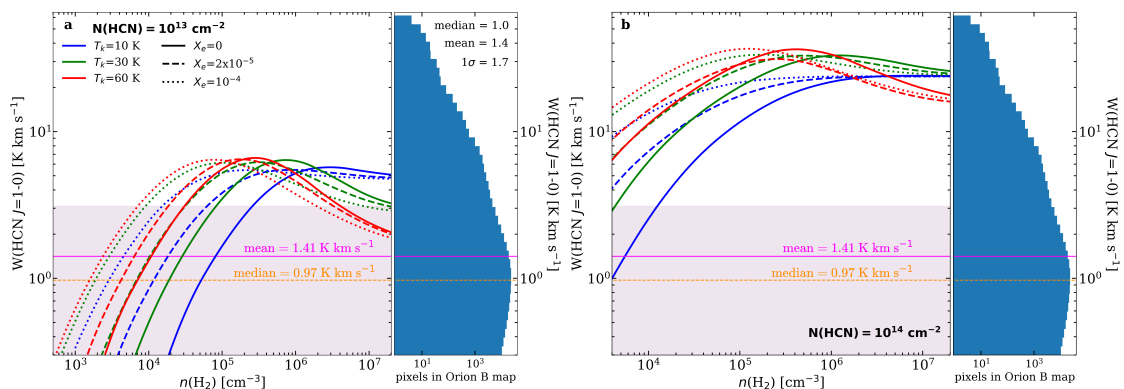
Fig. 9. Comparison of observed W(HCN $J=1$–0) intensities in Orion B and predictions from nonlocal and non-LTE radiative transfer models including line overlap for (a) N(HCN) $=10^{13}$ cm^{-2} and (b) N(HCN) $=10^{14}$ cm^{-2}. The continuous curves show model results for $T_k = 60$, 30, and 10 K (red, green, and blue curves, respectively), different ionization fractions: $\chi_e = 0$ (continuous curves), $\chi_e = 2 \times 10^{-5}$ (dashed curves), and $\chi_e = 10^{-4}$ (dotted curves). The pink and orange horizontal line mark the mean and median values of W(HCN $J=1$–0). The pink shaded area represents the standard deviation (1σ) relative to the mean detected W(HCN $J=1$–0) intensities in Orion B (at 30″). Positions in the pink area account for ∼70% of the total $L_{HCN\,1-0}$ in the map. The right panels show an histogram with the distribution of W(HCN $J=1$–0) detections in individual map pixels.

(Gonzalez-Alfonso & Cernicharo 1993; Goicoechea et al. 2022). This questions the precision of the parameters obtained from the LTE-HFS fitting method. To illustrate this, Fig. D.1 shows the (poor) best LTE-HFS fit to the HCN $J = 1$–0 HFS lines toward the Horsehead PDR.

The linewidth of the faintest $F = 0$–1 HFS component in the map ranges from ~ 1 to ~ 2 km s^{-1} (see also Table G.1). These linewidths are broader than the narrow linewidths, ~ 0.5 km s^{-1}, typically observed in Orion B toward dense and FUV-shielded cold cores in molecules such as H^{13}CO$^+$ (e.g., Gerin et al. 2009). Thus, HCN $J = 1$–0 traces a different cloud component. Figure 8b shows the histogram of the HFS linewidth ratios $R_{02}^{\Delta v}$ and $R_{12}^{\Delta v}$. They peak at 0.75 and 0.91 respectively, with median values of 0.91 and 1.03. That is, the linewidths of the different HFS components are not the same and line opacity broadening matters. Non-LTE models including line overlap predict these anomalous linewidth ratios, $R^{\Delta v} \neq 1$, when HFS lines become optically thick (e.g., see Fig. 3 of Goicoechea et al. 2022).

4.3. Physical conditions of the extended low surface brightness HCN $J = 1$–0 emitting gas

Here we compare the observed line integrated intensities W(HCN $J = 1$–0) with a grid of non-local and non-LTE radiative transfer models calculated by Goicoechea et al. (2022). These models include HFS line overlaps and use new HFS-resolved collisional rate coefficients for inelastic collisions of HCN with para-H$_2$, ortho-H$_2$, and electrons in warm gas.

The grid of single-component ($T_k = 60$, 30, and 10 K) static-cloud (no velocity field) models encompass the HCN column densities predicted by our chemical models (Sect. 5) and typically observed in Orion B (Fig. 7b): N(HCN) $= 10^{13}$ cm^{-2}, representative of optically thin or marginally optically thick HCN $J = 1$–0 HFS lines, and N(HCN) $= 10^{14}$ cm^{-2}, representative of bright optically thick lines. The range in gas densities n(H$_2$) goes from $\sim 10^7$ cm^{-3}, only relevant to hot cores and protostellar envelopes, to nearly 10^2 cm^{-3}, relevant to the most extended and FUV-illuminated component of GMCs. As we are mostly interested in this component, these models compute the HCN excitation for three different electron abundances: $\chi_e = 10^{-4}$, 2×10^{-5}, and 0. Figure 9 shows model results (continuous curves) in the form of predicted line intensities W(HCN $J = 1$–0) as a function of n(H$_2$).

The right panels in Fig. 9 show histograms with the distribution of W(HCN $J = 1$–0) detections ($> 3\sigma$) in individual pixels of the map. The mean (median) intensity[7] in these pixels is 1.4 K km s^{-1} (0.97 K km s^{-1}). The pink shaded area in Fig. 9 represents the 1σ dispersion relative to the mean W(HCN $J = 1$–0) value. However, while about 70% of the observed intensities have a value below the mean, less than 1% of the observed intensities have a value above 10 K km s^{-1} (very bright HCN emission). In the following we take W(HCN $J = 1$–0) $= 1$ K km s^{-1} as the reference[7] for the extended cloud emission. Models with N(HCN) $= 10^{13}$ cm^{-2} (Fig. 9a) encompass this W(HCN $J = 1$–0) intensity level. The gas temperature in this cloud component is $T_k \simeq 30$ to 60 K (translucent gas and UV-illuminated cloud edges; see specific PDR models in Sect. 5). Using N(HCN) $= 10^{13}$ cm^{-2} and

---

[7] This value is higher than the line intensity of the average HCN $J = 1$–0 spectrum over the full mapped area (see Table 4), thus including emission free pixels. The mean and median W(HCN $J = 1$–0) intensity values computed considering pixels with CO $J = 1$–0 detections above 3σ are 1.0 and 0.7 K km s^{-1}, respectively.
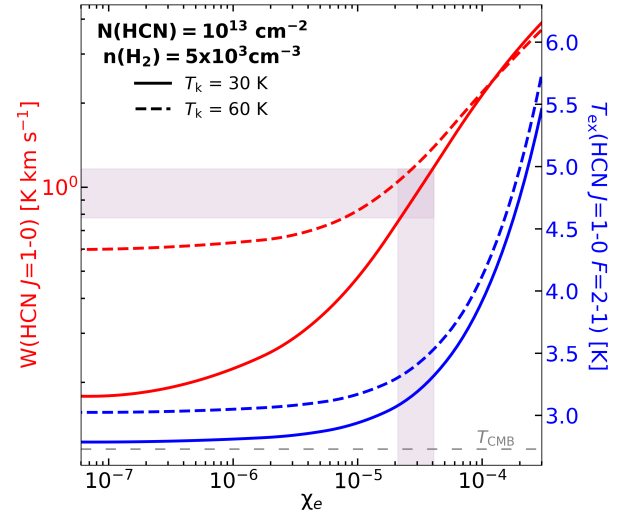
Fig. 10. W(HCN $J = 1$–0) (red curves) and T_{ex} (HCN $J = 1$–0 $F = 2$–1) (blue curves) predicted by non-LTE radiative transfer models, appropriate to extended and translucent gas, as a function of electron abundance. The vertical pink shaded area intersects the typical W(HCN $J = 1$–0) $= 1$ K km s^{-1} intensity level ($\pm 20\%$).

neglecting electron collisional excitation ($\chi_e = 0$) we determine an upper limit to the gas density of n(H$_2$) $\simeq (1$–3) $\times 10^4$ cm^{-3}.

Figure 10 shows the effect of electron excitation predicted by radiative transfer models appropriate to this extended and translucent gas (adopting n(H$_2$) $= 5 \times 10^3$ cm^{-3}). The plot shows how W(HCN $J = 1$–0) (red curves) and T_{ex}(HCN $J = 1$–0 $F = 2$–1) (blue curves) increase as the electron abundance χ_e increases. The reference intensity value, W(HCN $J = 1$–0) $= 1$ K km s^{-1}, intersects the model curves at an electron abundance of a few 10^{-5} and $T_{ex} \simeq 3.2$–3.5 K. These low excitation temperatures imply weak collisional excitation, but still $T_{ex} > T_{CMB}$.

Interestingly, the extended HCN $J = 1$–0 emission observationally correlates well with the [C I] 492 GHz emission (see Fig. 2 and Sect. 6.2.1). In addition, our photochemical models show that χ_e reaches $\gtrsim 10^{-5}$ in the [C I] 492 GHz emitting cloud layers (see Sect. 5). For such high χ_e values, electron excitation enhances the HCN $J = 1$–0 emission at low gas densities (see Fig. 10 and Goldsmith & Kauffmann 2017; Goicoechea et al. 2022). Hence, we estimate that the median gas density in the extended cloud component is n(H$_2$) $\simeq (4$–7) $\times 10^3$ cm^{-3} if $\chi_e \simeq 2 \times 10^{-5}$ (or $\simeq 10^3$ cm^{-3} if $\chi_e \simeq 10^{-4}$).

On the other hand, the strongest HCN-emitting regions in Orion B, those with W(HCN $J = 1$–0) > 6 K km s^{-1}, only represent $\sim 15\%$ of the total HCN $J = 1$–0 luminosity in the map. This bright HCN emission can only be reproduced by models with N(HCN) $= 10^{14}$ cm^{-2} and higher gas densities, n(H$_2$) $> 10^5$ cm^{-3}.

4.4. Rotationally excited HCN and H^{13}CN toward representative cloud environments in Orion B

To complement our analysis of the HCN $J = 1$–0 emission at large spatial scales, and to determine more accurate HCN column densities, here we analyze our multiple-J HCN and H^{13}CN line observations toward 14 positions in Orion B (see Table 3 for a brief explanation). Figure 3 shows a selection of the spectra. We detect HCN $J = 2$–1 and $J = 3$–2 toward all positions, and HCN $J = 4$–3 toward five of the 14 observed positions (Fig. G.1 shows the spectra of all observed positions).
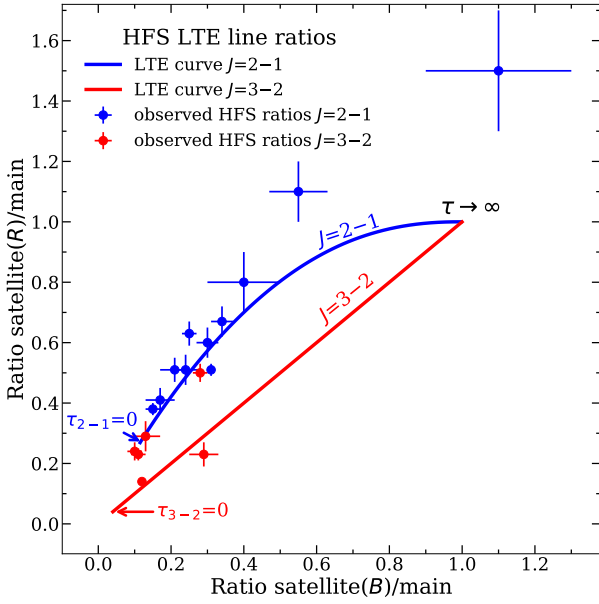
Fig. 11. HCN $J=2-1$ and $J=3-2$ HFS intensity ratios satellite(R)/main versus satellite(B)/main (see Sect. 4.4 for their definition) in LTE and as line opacities increase. Blue and red dots show the observed HFS line ratios toward the representative positions (see Table D.1).

The HCN $J=2-1$ transition has six HFS lines that, for the narrow line widths in Orion B, blend into three lines with apparent relative intensity ratios ~1:9:2 in the LTE and optically thin limit (red vertical lines in Fig. 3). The HCN $J=3-2$ transition also has six HFS lines. Only the central ones are blended and cannot be spectrally resolved. This gives the impression of three lines with relative intensity ratios 1:25:1 in the LTE and optically thin limit (e.g., Ahrens et al. 2002; Loughnane et al. 2012). We term these three apparent components (blueshifted, central, and redshifted) of the $J=2-1$ and $J=3-2$ rotational lines as "satellite (B)," "main," and "satellite (R)," respectively. We recall that these overlapping lines in the HCN $J=2-1$ and $3-2$ transitions are responsible of the observed anomalous HCN $J=1-0$ HFS line intensity ratios (Goicoechea et al. 2022, and references therein).

Blue and red curves in Fig. 11 show the expected HCN $J=2-1$ and $J=3-2$ HFS intensity ratios satellite (R)/main versus satellite (B)/main in LTE as line opacities increase. Only when $\tau_{2-1} \to 0$ and $\tau_{3-2} \to 0$, one should detect the ~1:9:2 and ~1:25:1 HFS ratios. The filled dots in Fig. 11 show the observed ratios (summarized in Table D.1) toward the sample of representative positions that could be fitted with three Gaussian lines. This plot shows that several HCN $J=2-1$, and specially $J=3-2$, HFS line intensity ratios do not lie on the LTE curves even for elevated line opacities. That is, the emission of rotationally excited HCN lines can also be anomalous.

4.4.1. HCN and HNC rotational diagrams

Here we estimate the degree of excitation (by determining rotational temperatures, $T_{\rm rot}$) and column densities of HCN and HNC toward the sample of representative positions. We analyze the detected rotationally excited HCN (up to $J=4-3$) and HNC (up to $J=3-2$) lines by constructing rotational population diagrams in Appendix E (Goldsmith & Langer 1999). We derive N(HCN), and N(HNC) ignoring their HFS structure (i.e., only the total line intensity of each rotational transition matters).

This is a valid approximation to obtain $T_{\rm rot}$ from observations of multiple-J lines. We derive the HCN column density and rotational temperature under the assumption of optically thin emission ($N^{\rm thin}$ and $T_{\rm rot}^{\rm thin}$). We also determine their opacity-corrected values ($N^{\tau,{\rm corr}}$ and $T_{\rm rot}^{\tau,{\rm corr}}$) by using the $H^{13}CN$ line intensities (see Fig. G.1) and assuming that the emission from HCN and $H^{13}CN$ lines arise from the same gas. Except for the brightest position #1, the derived HCN rotational temperatures range from 4 to 10 K (i.e. subthermal excitation), and $N^{\tau,{\rm corr}}$(HCN) ranges from 5×10^{12} to 3.4×10^{13} cm^{-2}. Table 7 summarizes the derived values and Appendix E shows the resulting rotational diagram plots. We employ the same methodology for HNC and $HN^{13}C$. Rotational temperatures are also low, from 5 to 11 K. HNC column densities range from ~10^{12} to 1.6×10^{13} cm^{-2} (see Table E.1).

4.4.2. Comparison with single-component non-LTE models

Most of the observed representative positions likely have velocity, temperature, and density gradients (specially prestellar cores and protostars). However, carrying out a complete, source-by-source, radiative transfer analysis is beyond the scope of this study (more focused on the extended cloud component). Here we just used the outputs of the grid of single-component and static models computed by Goicoechea et al. (2022), and presented in Sect. 4.3, to estimate the physical conditions (gas temperature and densities) compatible by the detected rotationally excited HCN line emission. We compared the observed line intensity ratios $R_{21}^J = W$(HCN $J=2-1$)/W(HCN $J=1-0$) and $R_{31}^J = W$(HCN $J=3-2$)/W(HCN $J=1-0$) summarized in Table 7 with the models shown in Fig. 10 of Goicoechea et al. (2022). As an example, the observed line ratios toward the Horsehead PDR are $R_{21}^J = 0.5$ and $R_{31}^J = 0.13$. These ratios can be explained by models with $T_k = 30-60$ K and $n(H_2)$ of a few 10^4 cm^{-3}. Position #14 shows the lowest line ratios of the sample, $R_{21}^J = 0.3$ and $R_{31}^J = 0.06$, which is consistent with $n(H_2)$ of a few 10^4 cm^{-3}. On the other hand, the observed line intensity ratios toward position #1 (center of NGC 2024) are $R_{21}^J = 0.9$ and $R_{31}^J = 1.2$. In this position we derive the highest HCN rotational temperature (~38 ± 10 K). The observed $R_{31}^J > R_{21}^J$ intensity ratios are consistent with the presence of dense gas, $n(H_2) \geq 10^6$ cm^{-3}.

4.5. HCN/HNC intensity and column density ratios

Table 8 summarizes the resulting N(HCN)/N(HNC) column density ratios obtained from rotational population diagrams (Sect. 4.4.1) as well as W(HCN)/W(HNC) $J=1-0$ and $J=3-2$ line intensity ratios. The positions that host lower excitation conditions (e.g., low $T_{\rm rot}$(HNC)) tend to have lower N(HCN)/N(HNC) column and W(HCN)/W(HNC) intensity ratios. Mildly FUV-illuminated environments such as the Horsehead nebula show W(HCN)/W(HNC) line intensity ratios of about two, whereas the most FUV-shielded cold cores and their surroundings (positions #7, #8, #10, #13) display ratios of about one. On the other hand, the most FUV-irradiated and densest cloud environments (those with HCN $J=4-3$ detections in NGC 2024) show ratios of at least four (positions #1 and #2).

These results roughly agree with the spatial correlation between the HCN/HNC $J=1-0$ integrated line intensity ratio and G_0' in the entire region. Figure 12 shows a 2D histogram of the observed W(HCN)/W(HNC) $J=1-0$ intensity ratio as a function of G_0' in the mapped region. The running median HCN/HNC $J=1-0$ intensity ratio increases from $\simeq 1$ at $G_0' \simeq 10$

Table 7. HCN $J = 1$–0 HFS line intensity ratios, W(HCN $J = 2$–1)$/W$(HCN $J = 1$–0) and W(HCN $J = 3$–2)$/W$(HCN $J = 1$–0) line intensity ratios, and parameters derived from rotational population diagrams, computed in Appendix E, toward a sample of representative cloud positions.

Pos.	HCN $J = 1$–0				Excited HCN		Rotational diagrams			
	R_{02}	R_{12}	$R_{02}^{\Delta v}$	$R_{12}^{\Delta v}$	$R^{J=2-1}_{J=1-0}$	$R^{J=3-2}_{J=1-0}$	$T_{\rm rot}^{\rm thin}$	$N^{\rm thin}$	$T_{\rm rot}^{\tau,\rm corr}$	$N^{\tau,\rm corr}$
							(K)	10^{13} (cm^{-2})	(K)	10^{13} (cm^{-2})
#1	0.3	0.4	1.1	1.1	0.9 ± 0.4	1.2 ± 0.5	18 ± 5	5 ± 3	38 ± 10	86 ± 20
#2	0.2	0.7	1.2	1.9	1.0 ± 0.4	0.7 ± 0.3	11 ± 2	0.8 ± 0.3	10 ± 1	1.5 ± 0.3
#3	0.3	0.4	0.9	1.1	1.0 ± 0.4	0.5 ± 0.2	10 ± 1	0.9 ± 0.4	7 ± 1	
#4	0.6	0.5	1.0	1.0	0.7 ± 0.3	0.2 ± 0.1	9 ± 2	0.2 ± 0.1	7 ± 1	0.5 ± 0.3
HH PDR	0.3	0.5	0.7	0.9	0.5 ± 0.2	0.13 ± 0.04	8 ± 1	0.5 ± 0.3	5 ± 1	1.6 ± 1.4
#6	0.2	0.6	0.8	0.9	0.6 ± 0.2	0.4 ± 0.2	7 ± 1	1.1 ± 0.7		
#7	0.3	0.5	0.8	1.0	0.8 ± 0.3	0.3 ± 0.1	6.6 ± 0.8	0.8 ± 0.3	5.2 ± 0.3	2.4 ± 0.4
#8	0.5	0.6	0.8	1.0	0.7 ± 0.3	0.3 ± 0.1	6.1 ± 0.6	0.5 ± 0.1	4.2 ± 0.2	3.0 ± 0.7
HH Core	0.3	0.5	0.7	1.0	0.5 ± 0.2	0.16 ± 0.08	5.3 ± 0.7	0.7 ± 0.4	4.3 ± 0.5	2.2 ± 1.1
#10	0.2	0.5	0.7	1.1	0.4 ± 0.2	0.12 ± 0.04	5.0 ± 0.9	0.4 ± 0.2		
#11	0.3	0.6	0.8	1.0	0.4 ± 0.2	0.10 ± 0.04	6.8 ± 0.9	0.5 ± 0.3		
#12	0.4	0.5	0.8	0.8	0.3 ± 0.1	0.10 ± 0.04	4.7 ± 0.9	0.7 ± 0.5		
#13	0.2	0.6	1.0	1.1	0.3 ± 0.1	0.09 ± 0.04	4.7 ± 0.8	0.4 ± 0.2		
#14	0.4	0.5	1.0	1.1	0.3 ± 0.1	0.06 ± 0.02	4.4 ± 0.5	0.4 ± 0.2		

Notes. The uncertainty in R_{02}, R_{12}, $R_{02}^{\Delta v}$, and $R_{12}^{\Delta v}$ is between 10 and 20%.

Table 8. HNC rotational temperatures, HCN/HNC column density, and line intensity ratios toward selected positions in Orion B.

Pos.	$T_{\rm rot}$(HNC)	$\frac{N(\rm HCN)}{N(\rm HNC)}$ [†]	$\frac{W(\rm HCN)}{W(\rm HNC)}$ $J = 1$–0	$\frac{W(\rm HCN)}{W(\rm HNC)}$ $J = 3$–2
#1	11 ± 2	3–54	4	4
#2	9 ± 2	4–7.5	4	3
#3	7 ± 1	3–14	4	5
#4	6 ± 1	0.7–1.7	0.8	0.6
HH PDR	5 ± 1	1.7–5	2	2
#6	6 ± 1	3	3	5
#7	8 ± 1	1.2–4	1	0.6
#8	8 ± 1	0.8–5	1	0.5
HH Core	6 ± 1	2–5	2	1.6
#10	6 ± 1	1.3	1	0.8
#11	–	–	3	–
#12	6 ± 1	1.7	2	1.2
#13	5 ± 1	1.3	1	0.8
#14	5 ± 1	4	3	2

Notes. [†]The lower value of the ratio adopts column densities obtained from rotational diagrams in the optically thin limit. The higher value of the ratio implements a line opacity correction (see Tables 7 and E.1).

Fig. 12. 2D histogram of the observed HCN/HNC $J = 1$–0 line intensity ratio as a function of G_0' in the Orion B map. The dashed black curve shows the running median. The error bars show the standard deviation.

to $\simeq 3$ at $G_0' \simeq 200$. For higher values of G_0', the running median intensity ratio stays roughly constant at $\simeq 3$–4. We estimate that the higher HCN $J = 1$–0 line opacity toward these bright positions (at least $\tau \simeq 5$–10, see Table D.1) compared to that of HNC $J = 1$–0 (on the order of $\tau \simeq 1$–3, Table E.1) contributes to the observed constancy of the line intensity ratio.

In FUV-illuminated environments, the strength of the radiation field influences the gas chemistry and determines much of the gas temperature and electron abundance (see Sect. 5). At a given abundance, HNC responds more weakly to electron excitation than HCN. In particular, the HCN $J = 1$–0 critical fractional abundance of electrons ($\chi_{\rm cr,e}^*$ in Table 1) is a factor of ~4

lower than that of HNC $J = 1$–0. Moreover, HNC is typically less abundant in FUV-illuminated gas (Sect. 5).

In addition, as HCN and HNC rotational lines become optically thick, HFS line overlap effects become important for both species. However, their relative effect as a function of J are different (Daniel & Cernicharo 2008). These aspects ultimately drive their excitation and contribute to the slightly different rotational temperatures we infer for the two species. Still, modeling the HFS resolved excitation of HNC is beyond the scope of our study. Future determinations of HFS-resolved HNC–H$_2$ inelastic collision rate coefficients will make such detailed studies feasible.

5. HCN and HNC chemistry in FUV-illuminated gas

To guide our interpretation of the extended HCN $J = 1$–0 emission, here we reassess the chemistry of HCN, HNC, and related
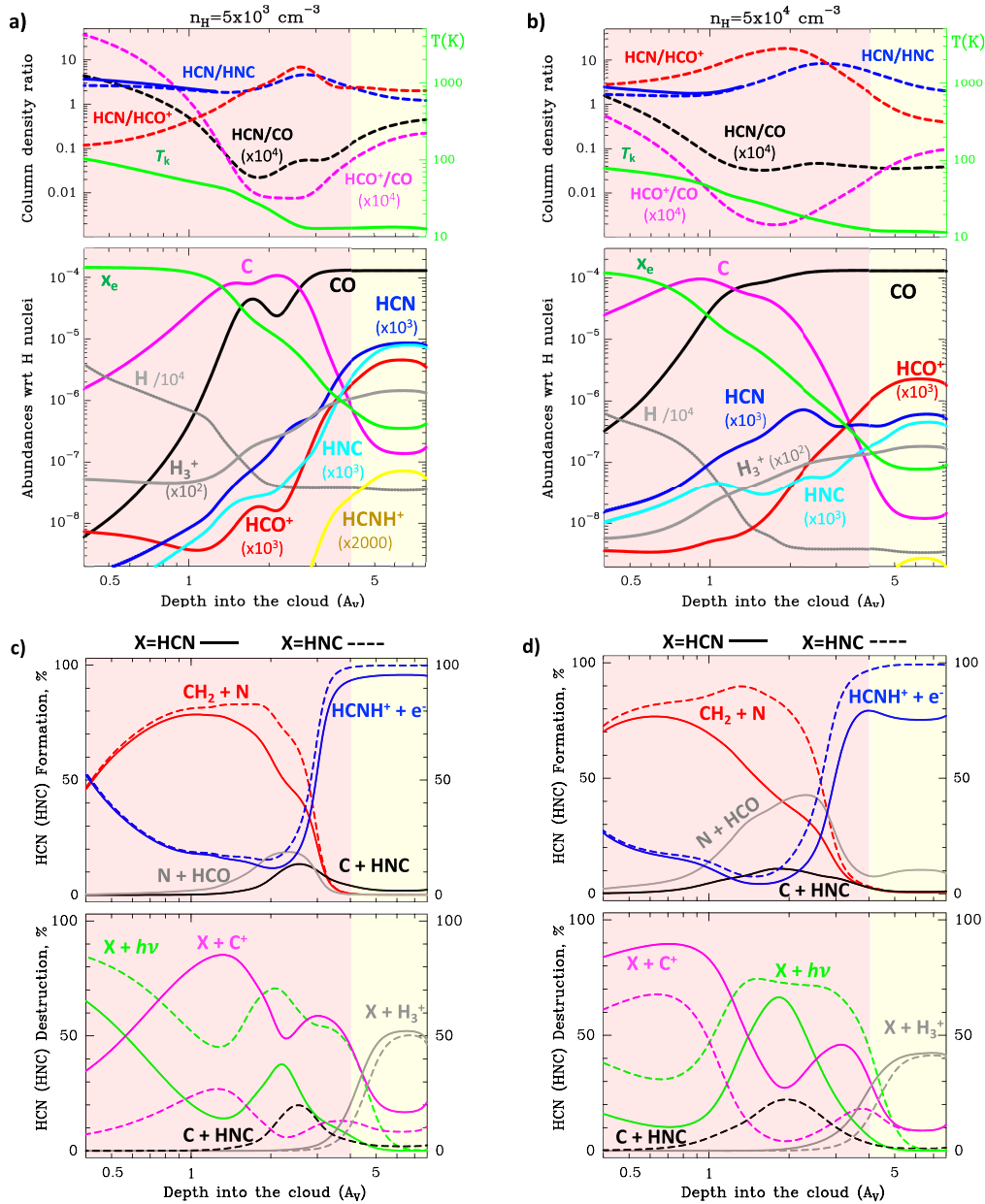
Fig. 13. Constant density gas-phase PDR models with $G_0 = 100$ and $n_H = 5 \times 10^3$ cm^{-3} (left) and 5×10^4 cm^{-3} (right). These models adopt $E_b = 1200$ K for Reaction (8). Upper panels in (a) and (b): dashed curves show the depth-dependent column density ratios of selected species (left y-axis). The blue continuous curves in the upper panels of (a) and (b) show the HCN/HNC column density ratio adopting $E_b = 200$ K. Green continuous curves show the temperature structure as a function of A_V (right y-axis). Lower panels in (a) and (b): abundance profiles with respect to H nuclei. (c) and (d): Contribution (in percent) of the main formation and destruction reactions for HCN (continuous curves) and HNC (dashed curves).

species in FUV-illuminated gas. The presence of FUV photons, C$^+$ ions, C atoms, and high electron abundances triggers a distinctive nitrogen chemistry, different to that prevailing in cold and dense cores (e.g., Hily-Blant et al. 2010) shielded from FUV radiation. Sternberg & Dalgarno (1995), Young Owl et al. (2000) and Boger & Sternberg (2005) previously studied the formation and destruction of HCN in FUV-irradiated gas. Here we used an updated version of the Meudon PDR code (Le Petit et al. 2006) that implements a detailed treatment of the penetration of FUV photons (Goicoechea & Le Bourlot 2007) and includes v-state-dependent reactions of FUV-pumped H$_2(v)$ (hereafter H$_2^*$) with neutral N atoms leading to NH + H (Goicoechea & Roncero 2022), as well as reactions of o-H$_2$ and p-H$_2$ with N$^+$ ions, leading to NH$^+$ + H (Zymak et al. 2013).

We also included the isomerization reaction:

$$\text{HNC} + \text{H} \rightarrow \text{HCN} + \text{H}, \tag{8}$$

with a rate coefficient $k(T) = 10^{-10} \exp(-E_b/T)$, where E_b is the reaction energy barrier. Theoretical calculations agree on the presence of a barrier, however, different methods provide slightly different barrier heights: ~2130 K (Talbi et al. 1996), ~1670 K (Sumathi & Nguyen 1998), and ~960 K (Petrie 2002). In our models we initially adopt $E_b = 1200$ K (see Graninger et al. 2014). We also included the isomerization reaction:

$$\text{HNC} + \text{C} \rightarrow \text{HCN} + \text{C}, \tag{9}$$

which is generally not included in dark cloud chemical models but plays a role in FUV-illuminated gas. We adopt a rate coefficient $k(T) = 1.6 \times 10^{-10}$ cm^3 s^{-1} and no energy barrier (from calculations by Loison et al. 2014; Loison & Hickson 2015).

In order to accurately treat the photochemistry of HCN and HNC, our models explicitly integrate their photodissociation and photoionization cross sections at each cloud depth. We use the wavelength-dependent cross sections tabulated in Heays et al. (2017), which include a theoretical calculation of the HNC photodissociation cross section by Aguado et al. (2017). For the interstellar radiation field, this cross section implies that HNC is photodissociated about two times faster than HCN.

We adopted a H$_2$ cosmic ray ionization rate ζ_{CR} of 10^{-16} s^{-1}, typical of translucent gas and cloud edges in the disk of the galaxy (e.g., Indriolo et al. 2015). We assumed standard interstellar dust grain properties and extinction laws. We ran photochemical models adapted to the illumination conditions and gas densities at large scales in Orion B. In particular, we adopted a representative FUV field of $G_0 = 100$, typical of the Horsehead edge, the IC 434 ionization front, and close to the mean G_0 in the mapped area (see Table 5). Nonetheless, we note that adopting lower G_0 values basically shifts the abundance profiles to lower cloud depths but the following chemical discussion remains very similar. Figure 13 shows the predictions of constant density models, with $n_H = 5 \times 10^3$ cm^{-3} (left panels) and $n_H = 5 \times 10^4$ cm^{-3} (right panels). Figures 13a and b show the predicted column density ratios (upper panels) and abundance[8] profiles (lower panels) as a function of cloud depth, in mag of visual extinction[9].

We determine molecular column densities at a given cloud depth A_V (or cloud path length l) by integrating the predicted depth-dependent abundance profile, x(species), from 0 to A_V:

$$N(l) = \int_0^{A_V} x(l)\, n_H\, dl, \qquad (10)$$

where $x(l)$ is the species abundance, with respect to H nuclei[7], at a cloud path length l.

5.1. Chemistry at cloud edges, $A_V < 4$ mag

The red shaded areas in Fig. 13 show model results for $A_V < 4$ mag typical of FUV-illuminated cloud edges. FUV photons drive the chemistry in these translucent layers that host the C$^+$ to C transition and have high electron abundances: from $x_e \simeq x(C^+) \simeq 10^{-4}$ to $x_e \simeq 10^{-6}$ depending on A_V and G_0/n_H. To simplify our chemical discussion, Fig. 14 summarizes the network of dominant chemical reactions at $A_V < 4$ mag. Wherever C$^+$ is abundant, reactions of CH$_2$ with N atoms dominate the formation of HCN and HNC, as shown by the red curves in Figs. 13c and 13d. These two figures show the contribution (in percent) of the main HCN and HNC formation and destruction reactions as a function of cloud depth. The second most important path for

HCN and HNC formation at $A_V < 4$ mag is HCNH$^+$ dissociative recombination. HCN and HNC destruction is governed by photodissociation and by reactions with C$^+$. Their exact contribution depends on the gas density and G_0. Our model assumes that the rate coefficient of reactions C$^+$ + HCN and C$^+$ + HNC, as well as the branching ratios of dissociative recombination HCNH$^+$ + e → HCN/HNC + H, are identical for both isomers (e.g., Semaniak et al. 2001). Therefore, the N(HCN)/N(HNC) column density ratio at $A_V < 4$ mag basically depends on the differences between HCN and HNC photodissociation cross sections. Wherever photodissociation dominates (e.g., green curves in Figs. 13c and 13d), we predict N(HCN)/N(HNC) $\simeq$ 1.5–2.5. These values are consistent with the ratio inferred toward the rim of the Horsehead, a nearly edge-on PDR (see Table 8).

Neutral atomic carbon reaches its abundance peak at $A_V \simeq 1$–3 mag (depending on n_H), which is relevant to understand the nature of the extended [C I] 492 GHz emission in Orion B (Fig. 2h). The isomerization reaction C + HNC → HCN + C as well as reaction N + HCO → HCN + O provide additional formation paths for HCN at $A_V < 4$ mag (black and gray curves in Figs. 13c and 13d). These two reactions enhance the HCN/HNC column density ratio to ~5–15 at $A_V \simeq 3$ mag. These ratios agree with the high N(HCN)/N(HNC) ratios we infer toward NGC 2024 (e.g., positions #1 and #2 in Table 8).

We end this subsection by giving the HCN and HNC column densities predicted by the $n_H = 5 \times 10^3$ cm^{-3} (5×10^4 cm^{-3}) models at $A_V = 4$ mag: N(HCN) $= 4.5 \times 10^{12}$ cm^{-2} (2.4×10^{12} cm^{-2}) and N(HNC) $= 1.8 \times 10^{12}$ cm^{-2} (4.5×10^{11} cm^{-2}). These column densities are representative of extended and translucent gas.

5.2. Intermediate depths, 4 mag < A_V < 8 mag

The yellow shaded areas in Fig. 13 show model results for 4 mag < A_V < 8 mag. In these intermediate-depth cloud layers, the FUV flux diminishes and most carbon becomes locked in CO. Figure 15 summarizes the dominant chemical reactions in these molecular cloud layers. As shown in Figs. 13c and 13d, HCN and HNC are now predominantly destroyed by reactions with abundant molecular and atomic ions (H$_3^+$ and C$^+$ at low densities, H$_3^+$, HCO$^+$, and H$_3$O$^+$ at higher densities). The main formation route for HCN and HNC switches to HCNH$^+$ dissociative recombination (blue curves in Figs. 13c and 13d). For equal branching ratios (Semaniak et al. 2001), the predicted N(HCN)/N(HNC) column density ratio is $\simeq$ 1–2. Indeed, our observations of Orion B reveal N(HCN)/N(HNC) ratios and W(HCN J = 1–0)/W(HNC J = 1–0) line intensity ratios of $\simeq$ 1–2 toward positions with low G_0' values (see Table 8 and Fig. 6).

The abundance of HCNH$^+$, the precursor of HCN and HNC at large A_V (Figs. 13c and 13d), depends on the H$_3^+$ abundance, which is sensitive to the penetration of FUV radiation and to the cosmic ray ionization rate. The H$_3^+$ abundance is higher at lower n_H because the higher penetration of FUV radiation reduces the abundances of the neutral species (CO, O, N$_2$, and S) that destroy H$_3^+$. In addition, the H$_3^+$ abundance scales with ζ_{CR}. We run a few models with ζ_{CR} rates significantly lower than assumed in Fig. 13 and indeed they produce lower HCNH$^+$ abundances than those shown in Figs. 13a and b. This leads to higher HCN/HNC abundance ratios (see also Behrens et al. 2022) because reaction:

$$N + HCO \rightarrow HCN + O, \qquad (11)$$

becomes more important than HCNH$^+$ dissociative recombination. Reaction (11) is often quoted in chemical networks

---

[8] Because at low A_V the abundance of H atoms can be significant, in this Section we provide the abundance of a given species (x) with respect to H nuclei. That is, x(species) $= n$(species)$/n_H$, where $n_H = n(H) + 2n(H_2)$. If the abundance of H atoms is negligible, then x(species) $= 0.5\, \chi$(species).

[9] In these 1D PDR models, the cloud depth or shielding (A_V in mag of visual extinction) refers to the extinction normal to the cloud surface and parallel to the FUV illumination direction. In general, this extinction is different from A_V determined from observations and the dust SED along a given line of sight. Only for a face-on cloud (with the illuminating stars in the observed line of sight) both magnitudes are equivalent.
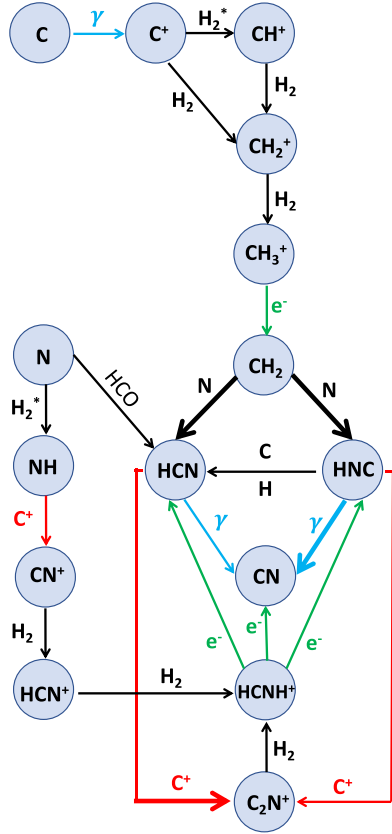
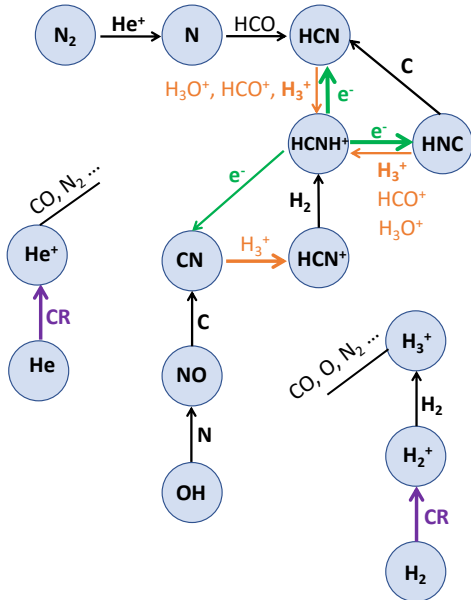**Fig. 14.** Dominant chemical reactions in FUV-illuminated gas.

Fig. 15. Dominant chemical reactions in FUV-shielded gas.

(Mitchell 1984; Young Owl et al. 2000) but no detailed study seems to exist.

We end this subsection by providing HCN and HNC column densities predicted at $A_V = 8$ mag. The PDR model with $n_H = 5 \times 10^3$ cm^{-3} (5×10^4 cm^{-3}) predicts $N(HCN) = 6.2 \times 10^{13}$ cm^{-2} (6.4×10^{12} cm^{-2}) and $N(HNC) = 5.2 \times 10^{13}$ cm^{-2} (3.2×10^{12} cm^{-2}). These column densities encompass the range of HCN (see Table 7) and HNC (see Table E.1) column densities we infer toward the observed sample of representative positions in Orion B.

5.3. On HNC destruction reactions

Previous studies invoked that the isomerization reaction $H + HNC \rightarrow HCN + H$ determines a temperature dependence of the $N(HCN)/N(HNC)$ ratio in warm molecular gas (Schilke et al. 1992; Herbst et al. 2000; Graninger et al. 2014; Hacar et al. 2020). In our PDR models, the gas temperature is $T \simeq 50$ K at $A_V \simeq 1$ mag, and $T \simeq 15$ K at $A_V \simeq 4$ mag (upper panels of Fig. 13a and b). We run the same two models adopting $E_b = 200$ K for reaction (8) and found that reducing E_b has little effect on the predicted $N(HCN)/N(HNC)$ ratio (blue continuous curves in the upper panels of Figs. 13a and b). Even at $A_V < 2$ mag, where the abundance of H atoms and T are moderately high, the $N(HCN)/N(HNC)$ ratio increases by less than 30% (i.e., the effects are very small). We note that in all these models, HCN and HNC photodissociation, as well as $C + HNC \rightarrow HCN + C$ reactions, are faster than the isomerization reaction $H + HNC$ (see Figs. 13c and 13d).

We run a more extreme model adopting $E_b = 0$ K. That is to say, as if reaction (8) was barrierless. Only in this case, the isomerization reaction $H + HNC \rightarrow HCN + H$ would dominate HNC destruction (specially at large A_V), increasing the $N(HCN)/N(HNC)$ ratio. However, this choice of E_b results in very low HNC column densities, 2×10^{12} cm^{-2} and 3×10^{11} cm^{-2} at $A_V = 8$ mag for $n_H = 5 \times 10^3$ cm^{-3} and 5×10^4 cm^{-3}, respectively. These $N(HNC)$ values are much lower than the $N(HNC)$ column densities we infer from observations (Table E.1). In addition, models with $E_b = 0$ K would imply very high $N(HCN)/N(HNC) = 30$–75 ratios, something not seen in our observations (Table 8).

Some studies also suggest that in cold molecular gas, reaction $HNC + O \rightarrow CO + NH$ dominates HNC destruction, and thus it controls the HCN/HNC abundance ratio if the energy barrier of this particular reaction is low, $E_b \simeq 20$–50 K (Schilke et al. 1992; Hacar et al. 2020). However, these values are much lower than the expected theoretical barrier (A. Zanchet, priv.comm. and Lin et al. 1992). Overall, our observational results are more consistent, at least for the extended cloud emission, with a greater dependence of the $N(HCN)/N(HNC)$ ratio on the FUV radiation field (as suggested in planetary nebulae, Bublitz et al. 2019, 2022).

6. Discussion

In this section we discuss the nature of the extended HCN $J = 1-0$ emission observed in Orion B and its relation to other species. We conclude by comparing the observed line intensity vs. FIR dust continuum intensity scalings with the line luminosity vs. SFR scaling laws typically inferred in extragalactic studies.

6.1. The origin of the extended HCN $J = 1-0$ emission: weak collisional excitation vs. scattering

The existence of a widespread HCN $J = 1-0$ emission component in low density gas, weakly collisionally excited, but enhanced by electron collisions (see Sect. 4.3), may affect the interpretation of the extragalactic relationship HCN luminosity versus SFR. Alternatively, the extended HCN $J = 1-0$ emission we observe in Orion B might arise from photons emitted in dense
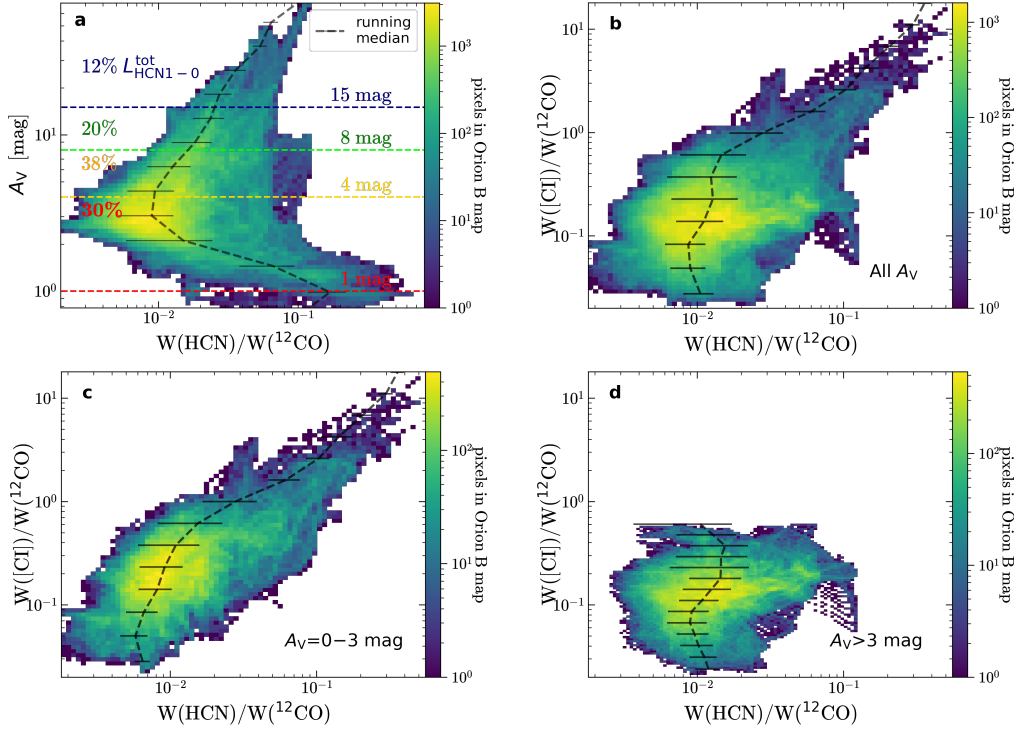
Fig. 16. 2D histograms. (a) Visual extinction A_V as a function of the HCN/CO $J = 1$–0 integrated intensity ratio (from maps at 120″ resolution). Dashed red, yellow, green, and blue horizontal lines are the visual extinction values 1, 4, 8, and 15 mag, respectively. Above each line, we show the percentage of the total HCN $J = 1$–0 luminosity that comes from the different A_V ranges. (b), (c), and (d) 2D histogram of the observed [C I] 492 GHz/CO $J = 1$–0 line intensity ratio (in units of K km s^{-1}) as function of the observed HCN/CO $J = 1$–0 line ratio for all A_V, for $A_V < 3$ mag, and for $A_V > 3$ mag. The dashed black curve shows the running median. Error bars show the standard deviation in the x-axis.

star-forming cores that become resonantly scattered by halos of low density gas. This seems to be the case, albeit at much smaller spatial scales, in dense cores inside cold dark clouds shielded from stellar FUV radiation (e.g., Langer et al. 1978; Walmsley et al. 1982; Cernicharo et al. 1984b; Gonzalez-Alfonso & Cernicharo 1993).

The above two scenarios lead to different HCN $J = 1$–0 HFS line intensity ratios (see predictions by Goicoechea et al. 2022), which can be tested on the basis of HFS resolved observations of the extended gas emission in GMCs. In particular, if the observed HCN $J = 1$–0 HFS photons arise from dense gas and become resonantly scattered by interacting with a low density halo, then both the R_{02} and R_{12} HFS line intensity ratios should be very anomalous. That is, $R_{02} < 0.2$ and $R_{12} < 0.6$. On the other hand, if the HCN $J = 1$–0 emission intrinsically arises from low density gas, far from dense cores, models predict that weak collisional excitation drives the HFS intensity ratios to $R_{02} \gtrsim 0.2$ and $R_{12} \lesssim 0.6$.

Figure 8a shows that the most common HCN $J = 1$–0 HFS line intensity ratios in Orion B are $R_{02} \gtrsim 0.2$ and $R_{12} < 0.6$ (Fig. 7). Hence, the very anomalous ratios predicted by the scattering halo scenario are rarely encountered at large scales. Therefore, we conclude that the extended HCN $J = 1$–0 emission in Orion B is weakly collisionally excited, and it mostly arises from low density gas. In particular, we determined $n(\mathrm{H_2})$ of several 10^3 cm^{-3} to 10^4 cm^{-3} (see Sect. 4.3). This result contrasts with the prevailing view of HCN $J = 1$–0 emission as a tracer of dense gas (e.g., Gao & Solomon 2004a,b; Rosolowsky et al. 2011; Jiménez-Donaire et al. 2017, 2019; Sánchez-García et al. 2022; Rybak et al. 2022).

6.2. Bimodal behavior of the HCN/CO $J = 1$–0 line intensity ratio as a function of A_V

Extragalactic studies frequently interpret the HCN/CO $J = 1$–0 line luminosity ratio as a tracer of the dense gas fraction (e.g., Lada 1992; Gao & Solomon 2004b,a; Usero et al. 2015; Gallagher et al. 2018; Jiménez-Donaire et al. 2019; Neumann et al. 2023). This interpretation assumes that CO $J = 1$–0 line emission is a tracer of the bulk molecular gas, whereas HCN $J = 1$–0 traces dense gas in star-forming cores (at high A_V). Normal galaxies have low luminosity ratios $L_{\mathrm{HCN}}/L_{\mathrm{CO}} = 0.02$–0.06 while luminous and ultraluminous galaxies have $L_{\mathrm{HCN}}/L_{\mathrm{CO}} > 0.06$. By contrast, Helfer & Blitz (1997) argue that the HCN/CO intensity ratio could measure the total hydrostatic gas pressure.

Figure 16a shows a 2D histogram of the HCN/CO $J = 1$–0 line intensity ratios in Orion B as a function of A_V. The 2D histogram shows a bimodal behavior. There is a first branch at $A_V > 3$ mag where $W(\mathrm{HCN})/W(\mathrm{CO})$ $J = 1$–0 increases with extinction (the assumed behavior in extragalactic studies). The running median $W(\mathrm{HCN})/W(\mathrm{CO})$ $J = 1$–0 ratio increases from $\gtrsim 0.02$ (at $A_V \simeq 8$ mag) to ~0.1 (dense cores at larger A_V). In addition, there is a second branch at $A_V < 3$ mag where $W(\mathrm{HCN})/W(\mathrm{CO})$ $J = 1$–0 increases with decreasing extinction. This is somehow unexpected, because the running median intensity ratio reaches high values, $\gtrsim 0.1$, in diffuse gas at $A_V \simeq 1$ mag.

Figure 6a shows the spatial distribution of the HCN/CO $J = 1$–0 intensity ratios in Orion B. The ratio is indeed high toward the dense gas in filaments and cores. In addition, $W(\mathrm{HCN})/W(\mathrm{CO})$ $J = 1$–0 also increases toward the east rim of the cloud that borders the ionization front IC 434. Owing
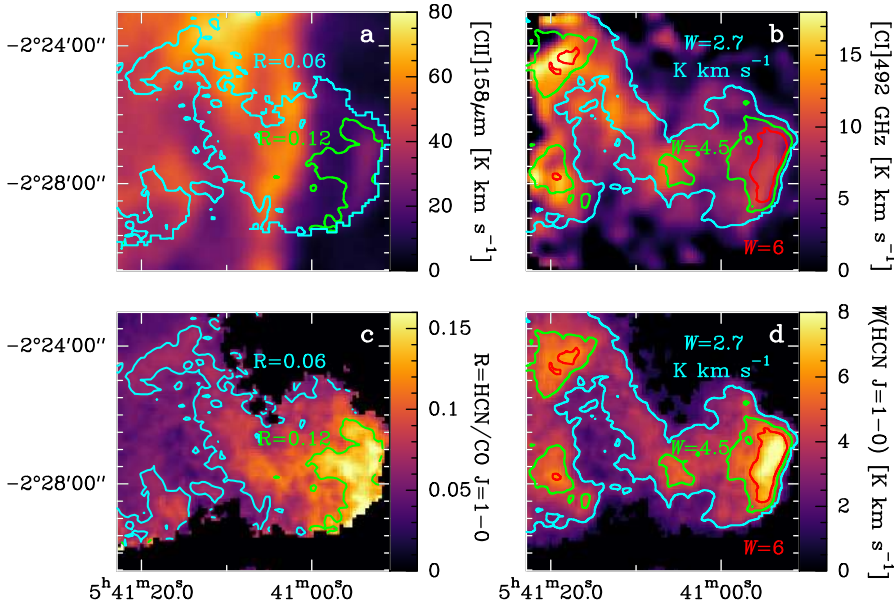
Fig. 17. 30″-resolution view of the Horsehead. (a) [C II] 158 μm (Pabst et al. 2017) and (b) [C I] 492 GHz (Philipp et al. 2006) integrated line intensity maps (from 7 to 18 km s⁻¹). (c) $R =$ HCN/CO intensity ratio and (d) HCN $J = 1$–0 line intensity maps. Contours on [C II] 158 μm map: HCN/CO ratio ($R = 0.06$ and 0.12). Contours on [C I] 492 GHz map: HCN $J = 1$–0 surface brightness ($W = 2.7$, 4.5, and 6 K km s⁻¹).

to the roughly edge-on geometry with respect to the illuminating stars, we can easily spatially resolve these FUV-illuminated cloud edges (high χ_e) from the more shielded cloud interior. This picture agrees with HCN $J = 1$–0 emission arising from extended and relatively low density gas, $n(H_2) \leq 10^4$ cm⁻³, in GMCs illuminated by FUV radiation, and being boosted by electron excitation. This extended cloud component must be common in GMCs that host young massive stars, or have massive stars in their vicinity.

6.2.1. Cloud porosity to FUV radiation: HCN 1–0 emission from high electron abundance gas traced by [C II] 158 μm and extended [C I] 492 GHz emission

The ionization fraction in cloud edges and in gas translucent to FUV–radiation is high. It starts at $\chi_e \simeq$ a few 10^{-4}, where the electron abundance is controlled by the photoionization of carbon atoms, thus leading to $\chi_e \simeq \chi(C^+)$ at $A_V \lesssim 2$ mag. These cloud layers emit bright FIR [C II] 158 μm fine-structure line emission. Slightly deeper inside the molecular cloud, at $A_V \lesssim 3$ mag, the flux of FUV photons decreases to the point where the gas becomes fully molecular, and neutral atomic carbon (C⁰) becomes more abundant than C⁺ (see PDR models in Figs. 13a and b). Our models predict $\chi_e \gtrsim 10^{-5}$ at the C⁰ abundance peak, where the [C I] 492 GHz line emission reaches its intensity peak.

Figure 17a shows a [C II] 158 μm line emission map of the Horsehead nebula and the ionization front IC 434 observed with SOFIA (Pabst et al. 2017) and convolved to the 30″ resolution of the ORION-B maps. The C⁺ map shows faint [C II] 158 μm emission from the (nearly edge-on) molecular PDR at the rim of the Horsehead. It also shows bright [C II] 158 μm emission from the neutral atomic PDR, $\chi(H) \gg \chi(H_2)$ at $A_V < 1$ mag, that delineates the edge of IC 434 and shows very little CO emission (e.g., Bally et al. 2018). Figure 17c shows a closer look to the HCN/CO $J = 1$–0 line intensity ratio. The ratio is particularly high, ≥ 0.12 (green contours), toward the FUV-illuminated cloud edge. This area matches the [C II] 158 μm emission from the rim of the Horsehead. As $n(H_2)$ is a few 10^4 cm⁻³ (e.g., Pabst et al. 2017) and $\chi^*_{cr,e}$(HCN $J = 1$–0) $< \chi_e \simeq \chi(C^+) \simeq 10^{-4}$, electron excitation

boosts the HCN emission (see Fig. 10), and thus the HCN/CO $J = 1$–0 line intensity ratio.

Figure 17b shows a map of the [C I] 492 GHz line emission around the Horsehead nebula observed with Caltech Submillimeter Observatory (Philipp et al. 2006) and smoothed to 30″ resolution. The HCN $J = 1$–0 emission nicely follows that of [C I] 492 GHz. This agrees with the widespread nature of neutral atomic carbon, and with the similar spatial distribution of [C I] 492 GHz and HCN $J = 1$–0 emission seen at much larger scales (cf., the complete Orion B maps in Fig. 2h). This observational result indicates that C⁰ coexists with HCN in large areas of the cloud, which implies moderate ionization fractions, $\chi_e \gtrsim 10^{-6}$ to several 10^{-5}, in gas where [C I] 492 GHz and HCN $J = 1$–0 emissions coexist.

Since the spatial and velocity distribution of the large-scale [C I] 492 GHz and ¹³CO $J = 1$–0 emission are very similar (Ikeda et al. 2002), the presence of C⁰ cannot be restricted to cloud edges ($A_V < 3$ mag). Otherwise Fig. 2h would only show bright [C I] 492 GHz emission parallel to the IC 434 front associated with the rims of all nearly edge-on PDRs such as the Horsehead (zoomed in Fig. 17). Instead, the [C I] 492 GHz emission is widespread and extended through the cloud. We find that [C I] 492 GHz also linearly correlates with the HCO⁺, HCN, and ¹³CO $J = 1$–0 emission (Pearson coefficients of 0.80, 0.79, and 0.73 respectively). These correlations include many positions at $A_V > 3$ mag (60% of [C I] 492 GHz detections, and 70% of total [C I] 492 GHz luminosity, see Fig. 4). Therefore, C⁰ must be abundant also toward the cloud interior. The most plausible scenario suggested by these maps is that GMCs are porous to FUV radiation. This is consistent with the detection of very extended 70 μm dust emission from FUV-illuminated grains (see Fig. 1). This implies that GMCs are inhomogeneous, and we are detecting [C I] 492 GHz emission from the cloud edges as well as from FUV-illuminated surfaces of structures located at moderate cloud depths (typically modeled as clumps, filamentary, or fractal structures, e.g., Boisse 1990; Falgarone et al. 1991; Spaans 1996; Stutzki et al. 1998; Barnes et al. 2013). Unfortunately, while ALMA, Keck, and JWST observations show surprisingly rich small-scale substructures in the prototypical PDR the Orion Bar (Goicoechea et al. 2016; Habart et al. 2023a,b), similar sub-arcsecond resolution observations of the [C I] 492 GHz

are still missing. Such observations will help to constrain the small-scale origin of C^0.

6.2.2. High HCN/CO $J = 1$–0 and [C I] 492 GHz/CO $J = 1$–0 line intensity ratios from gas at $A_V < 3$ mag

We close our discussion of the bimodal behavior of the $W(\text{HCN})/W(\text{CO})$ $J = 1$–0 intensity ratio by providing more evidence that FUV radiation (leading to abundant C^0 and moderate χ_e) is ultimately responsible of the increased ratios observed at $A_V < 3$ mag (Fig. 16a). These regions correspond to translucent gas and FUV-illuminated cloud edges. They coincide with enhanced [C I] 492 GHz/CO $J = 1$–0 line intensity ratios (Fig. 6), which traces low-density PDRs (Hollenbach et al. 1991; Kaufman et al. 1999). Hence, we expect that both ratios are related.

Figure 16 shows the distribution of [C I] 492 GHz/CO $J = 1$–0 and HCN/CO $J = 1$–0 intensity ratios in Orion B. The upper-right panel shows all detections (at all A_V) in the map. The running median clearly shows that, above a threshold of $W(\text{HCN})/W(\text{CO})$ $J = 1$–$0 \gtrsim 0.02$, the ratio quickly increases with the [C I] 492 GHz/CO $J = 1$–0 intensity ratio. The lower panels in Fig. 16 separate the HCN/CO and [C I]/CO detections in the lines of sight with $A_V < 3$ mag (Fig. 16c) and $A_V > 3$ mag (Fig. 16d). These plots show that the HCN/CO $J = 1$–0 line intensity ratio linearly correlates with [C I] 492 GHz/CO $J = 1$–0 at $A_V < 3$ mag. Hence, the ratios follow the increasing electron abundance in PDR gas. On the other hand, the ratios are not correlated at higher $A_V > 3$ mag. As a corollary, our observations imply that the detection of high HCN/CO $J = 1$–0 line intensity ratios do not always imply the presence of dense gas. The existence of a low-A_V branch, from extended FUV-illuminated low-density gas, leads to increasing ratios with decreasing A_V. This cloud component cannot be overlooked, specially in the context of the very large scale emission from GMCs, otherwise the mass of the dense molecular gas can easily be overestimated. In the next section we specifically quantify the amount of dense molecular gas traced by the HCN $J = 1$–0 emission.

6.3. The dense gas mass conversion factor α (HCN $J = 1$–0)

Using the dust SEDs across the observed field[10], we derive the mass of the dense gas in the mapped area (represented by gas at $A_V > 8$ mag, e.g., Lada et al. 2010). The likely density of this cloud component is $n(\text{H}_2) > 10^4$ cm^{-3} (e.g., Bisbas et al. 2019). We obtain $M_{\text{dg}} = 3.1 \times 10^3$ $M_\odot$, which accounts for about 20% of the total mass ($M_{\text{H}_2,\text{tot}} \sim 1.7 \times 10^4$ $M_\odot$) in the mapped area. These numbers imply a dense gas surface density ($\Sigma_{\text{dg}} = M_{\text{dg}}/A$) and a total gas surface density ($\Sigma_{\text{H}_2,\text{tot}} = M_{\text{H}_2,\text{tot}}/A$) of $\Sigma_{\text{dg}} = 13$ $M_\odot$ pc^{-2} and $\Sigma_{\text{H}_2,\text{tot}} = 70$ $M_\odot$ pc^{-2}, respectively, where in both cases we divide by the total mapped area, $A \simeq 250$ pc^2.

High spatial resolution observations of the dust SED are rarely available in extragalactic studies. Hence, it is appropriate to calibrate the mass of the dense molecular gas with the emitted luminosity of a convenient molecular line tracer, with HCN $J = 1$–0 being the traditional choice. Hence, it is common to define:

$$M_{\text{dg}} = \alpha(\text{HCN}) \cdot L'(\text{HCN}), \tag{12}$$

where $L'(\text{HCN})$ is the total HCN $J = 1$–0 line luminosity in the mapped area (in K km s^{-1} pc^2) as defined in

---
[10] Appendix C.2 details how we determine the gas mass.

Eq. (4). Gao & Solomon (2004a) originally estimated $\alpha(\text{HCN}) = 10$ $M_\odot$ / K km s^{-1} pc^2. Recent dust continuum and line emission surveys determine $\alpha(\text{HCN})$ in a few local GMCs (e.g., Shimajiri et al. 2017; Kauffmann et al. 2017; Barnes et al. 2020). These studies find quite a diversity of $\alpha(\text{HCN})$ values, from 10 to 500 $M_\odot$/K km s^{-1} pc^2. However, these surveys typically map star-forming clumps and their immediate environment (areas <1 deg^2) but do not account for, or do not spatially resolve, the extended HCN $J = 1$–0 emission from low density and more translucent gas. This emission is weakly excited ($T_{\text{CMB}} \lesssim T_{\text{ex}} \ll T_{\text{k}}$), but because it covers large spatial scales, its total line luminosity typically exceeds the line luminosity from dense gas in star-forming cores at $A_V > 8$ mag ($\sim$30% in Orion B).

Here we determine α for HCN, HCO$^+$, and HNC $J = 1$–0 lines in Orion B. We obtain $L'(\text{HCN}) = 110$ K km s^{-1} pc^2 for HCN $J = 1$–0, which implies a dense mass conversion factor $\alpha(\text{HCN}) = 29$ $M_\odot$/K km s^{-1} pc^2. Table 4 summarizes the luminosities and α values derived for other molecules. A recent survey of the Perseus low-mass star-forming region (at 11 arcmin resolution and covering 8.1 deg^2 or $\sim$215 pc^2) finds $\alpha(\text{HCN}) = 92$ $M_\odot$/K km s^{-1} pc^2, $L'(\text{HCN}) = 55.3$ K km s^{-1}, and $M_{\text{dg}} = 5.1 \times 10^3$ $M_\odot$ (Dame & Lada 2023). As FUV radiation favors the formation of HCN and the excitation of the $J = 1$–0 line at large spatial scales (enhanced by electron collisions; Sect. 6.1), our study suggests that the lower $\alpha(\text{HCN})$ value in Orion B is linked to the presence of FUV radiation from massive stars. Indeed, Shimajiri et al. (2017) mapped small areas of Orion B, Aquila, and Ophiuchus star-forming cores (<10 pc^2). They find that $\alpha(\text{HCN})$ anticorrelates with G_0. We do find this tendency at the much larger spatial scales of our maps, but not a strong anticorrelation. This can be explained by the nonlinear dependence of the HCN abundance, HCN $J = 1$–0 line emission, and electron abundance with G_0.

All in all, we conclude that there is no universal $\alpha(\text{HCN}$ $J = 1$–$0)$ value, as environmental conditions and contribution of the low density extended cloud component at different angular scales likely vary from cloud to cloud. In Orion B, the cloud mass at $A_V > 8$ mag is similar to that at $A_V < 3$ mag. This results in a similar value of the mass to total $L'(\text{HCN})$ ratio in both cloud components. Thus, it will not be straightforward to distinguish, based on the observation of a single line, which component dominates the emission from spatially unresolved GMCs.

6.4. Schmidt-like laws: Spatially resolved relations between molecular and atomic lines with FIR intensities

On more global spatial scales (hundreds of parsec to kiloparsec scales) than those discussed in our study, observations of nearby normal galaxies find a tight, close to linear, correlation between the HCN $J = 1$–0 line luminosity and the FIR luminosity (a proxy of the SFR when averaged on such global scales; Solomon et al. 1992; Gao & Solomon 2004a; Kennicutt & Evans 2012). However, when considering starburst galaxies and (U)LIRGs, the relation often deviates from linearity (e.g., Gao et al. 2007; García-Burillo et al. 2012; Usero et al. 2015; Sánchez-García et al. 2022). These luminous galaxies lie above the FIR–HCN correlation observed in nearby normal galaxies. They also display high HCN/CO $J = 1$–0 line luminosity ratios ($\sim$ 0.2) interpreted as galaxies having high fractions of dense molecular gas. Our survey of Orion B provides access to the local properties that contribute to the large averages seen in
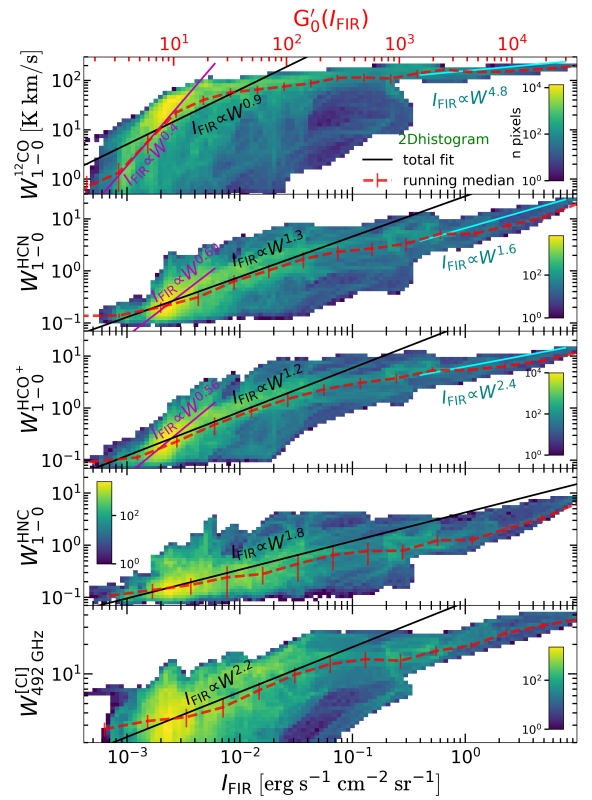
galaxies. In this section we discuss the spatially resolved relationships between I_{FIR} and CO, HCN, HCO$^+$, HNC $J = 1$–0, and [C I] 492 GHz line intensities (W) mapped in Orion B.

Figure 18 shows 2D histograms of the observed $W(\text{CO})$, $W(\text{HCN})$, $W(\text{HCO}^+)$, $W(\text{HNC})$, and $W(\text{[C I] 492 GHz})$ line intensities (in K km s^{-1}) as a function of I_{FIR} (in erg s^{-1} cm^{-2} sr^{-1}). We find that the observed line intensities W scale with I_{FIR} as a power law. As we fit these points using an orthogonal regression method[11] in log(y)-log(x) space and we use the appropriate error bars (the standard deviation) in both axes, we can present the scalings as $I_{\text{FIR}} \propto W^N$ (as in Fig. 18) or as $W \propto I_{\text{FIR}}^{1/N}$ (as in Fig. B.3). Perhaps provocatively, and in order to promote the comparison with the extragalactic scalings SFR–L_{mol} (e.g., Gao & Solomon 2004a; Shirley et al. 2008; Shetty et al. 2013, 2014a,b), here we start discussing the power-law indexes N.

As discussed in Sect. 2.5, I_{FIR} is a surrogate of the local FUV radiation field, G_0' (upper panel x-axis of Fig. 18). FUV photons are related to the presence of massive O and B stars that have short lifetimes. Thus, the FIR emission from FUV-heated grains is ultimately related to the SFR. However, the statistical connection between SFR and FIR luminosities in galaxies holds when averaging over large cloud samples (e.g., Kennicutt & Evans 2012). Therefore, the extrapolation of the local scalings in Orion B to galaxies (global averages) has to be taken with caution, bearing in mind that I_{FIR} traces the strength of the FUV radiation field, but L_{FIR} over a small region does not trace the true SFR[12].

By fitting all points in Fig. 18, we find that $W(\text{CO})$, $W(\text{HCO}^+)$ and $W(\text{HCN } J = 1$–0) scale with I_{FIR} as a power law with $N \sim 0.9$–1.3. However, $W(\text{HNC } J = 1$–0) and $W(\text{[C I] 492 GHz})$ show a different behavior, with a power-law index $N \sim 1.8$–2.2. A closer inspection of the $I_{\text{FIR}} - W(\text{CO } J = 1$–0) running median shows two clear tendencies. The median toward the brightest FIR positions ($I_{\text{FIR}} > 0.4$ erg s^{-1} cm^{-2} sr^{-1} or $G_0' > 1500$, mostly arising from NGC 2024 star-forming clump) shows a power-law index of $N \sim 4.8$. On the other hand, the faintest I_{FIR} and $W(\text{CO } J = 1$–0) positions show $N \sim 0.4$ (sublinear relationship). This faint CO emission is associated with widespread and very extended diffuse gas (low A_V and $G_0' < 20$).

The $I_{\text{FIR}} - W(\text{HCN } J = 1$–0) and $I_{\text{FIR}} - W(\text{HCO}^+ J = 1$–0) histograms are quite similar. They also reveal two different tendencies. Fitting the brightest I_{FIR} positions alone, most of them associated with dense gas in NGC 2024 (as demonstrated by the detection of bright HCN $J = 4$–3 line emission, Fig. 3), provides $N \sim 1.6$ for HCN and $N \sim 2.4$ for HCO$^+$ (superlinear relationships). In contrast, the most common low surface brightness HCN $J = 1$–0, HCO$^+$ $J = 1$–0, and I_{FIR} positions (those with $G_0' < 20$) show $N \sim 0.6$ (i.e., not far from the extended and diffuse CO emission index). Interestingly, the $I_{\text{FIR}} - W(\text{HNC } J = 1$–0) and $I_{\text{FIR}} - W(\text{[C I]492 GHz})$ histograms show a single superlinear tendency across the map, with $N \sim 1.8$ and 2.2, respectively. Hence, HNC and [C I] 492 GHz have a very different behavior compared to the other species. The derived N index for HNC resembles the index we find for HCN at the highest values of I_{FIR} ($G_0' > 1500$

---

[11] Using the Scipy-odr package (Branham 1995; Virtanen et al. 2020). https://docs.scipy.org/doc/scipy/reference/odr.html

[12] The total FIR luminosity in the mapped region of Orion B (~ 250 pc^2) is $L_{\text{FIR}} = 1.5 \times 10^5 \, L_\odot$ (or $\Sigma_{\text{FIR}} = 6 \times 10^2 \, L_\odot$ pc^{-2}). Using the extragalactic scalings (e.g., Kennicutt 1998a), these FIR luminosities translate into a SFR of $2.6 \times 10^{-5} \, M_\odot$ yr^{-1}, which is nearly an order of magnitude lower than the SFR estimated by counting young stellar objects (YSOs), $1.6 \times 10^{-4} \, M_\odot$ yr^{-1} (Lada et al. 2010). Pabst et al. (2021) find a similar result in Orion A, namely that SFR(FIR) < SFR(YSOs).

Fig. 18. 2D histograms of the ^{12}CO, HCN, HCO$^+$, HNC, $J = 1$–0, and [C I] $^3P_1 - ^3P_0$ line intensities as a function of FIR intensity in Orion B (from maps at 120″ resolution). The dashed red lines show the running median (median values of the integrated intensity within equally spaced log I_{FIR} bins). The error bars show their dispersion. Black lines (and associated text) show a linear fit (orthogonal regression in log(y)-log(x)) to all observed positions in each map. Magenta lines and blue lines show a linear fit to a range of $I_{\text{FIR}} < 6 \times 10^{-3}$ erg s^{-1} cm^{-2} sr^{-1} and (0.4–7.7) erg s^{-1} cm^{-2} sr^{-1}, respectively. We note that in each plot the number of line detections is different.

and dense gas), whereas the single index for [C I] 492 GHz resembles that of HCO$^+$ at high G_0'. This similitude must reflect their related chemistry and excitation conditions.

From the point of view of the local gas properties, Figs. 18 and B.3 show that $W(\text{CO } J = 1$–0), $W(\text{HCO}^+ J = 1$–0), and $W(\text{HCN } J = 1$–0) intensities increase with increasing I_{FIR} up to $G_0' \simeq 20$. Most of these positions refer to the extended cloud component, which hosts low densities and thus, the HCN $J = 1$–0 line is weakly collisionally excited (see Sect. 4.3), with $n(\text{H}_2) < n_{\text{cr, eff}}(\text{HCN } 1$–0) and thus, $T_{\text{ex}} < T_k$. Under these conditions (effectively thin emission), $W(\text{HCN } J = 1$–0) scales with $N(\text{HCN})$ even for large line opacities (see also Liszt & Pety 2016). Furthermore, our chemical analysis shows that models with a higher G_0/n_H ratio produce more HCN (Sect. 5 and Fig. 13). In addition, electron excitation contributes to enhance $W(\text{HCN } J = 1$–0) at low densities. These conditions favor the emission of CO, HCO$^+$, and HCN as G_0' increases.

On the other hand, Figs. 18 and B.3 show that $W(\text{CO } J = 1$–0), $W(\text{HCO}^+ J = 1$–0), and $W(\text{HCN } J = 1$–0) respond weakly to I_{FIR} once the FUV field becomes too intense ($G_0' > 1500$). These other regions at large A_V host denser gas, so that $n(\text{H}_2) > n_{\text{cr, eff}}(\text{HCN } 1$–0), and $J = 1$–0 lines turn into very optically thick, thus becoming less sensitive to column densities. Interestingly, $W(\text{HNC } J = 1$–0) and $W(\text{[C I] 492 GHz})$ weakly respond to I_{FIR} at all G_0'. We already showed that HNC traces

slightly denser gas than HCN (Fig. 5c) and that HNC responds less to electron excitation (Table 1). In addition, the observed W(HCN 1–0)/W(HNC 1–0) intensity ratio increases with the FUV field for $G_0' < 200$ (Fig. 12). Indeed, our chemical models show that the HNC abundance is lower in the FUV-illuminated gas (Sect. 5). This gas is usually at lower density than the FUV-shielded cold gas. Thus, we expect that most of the HNC $J = 1–0$ emission arises from gas in which $n(H_2) > n_{cr, eff}$(HNC 1–0). These facts explain the weaker response of W(HNC $J = 1–0$) to FUV radiation. Finally, PDR models predict that the C^0 column density is a weak function of gas density and especially of G_0 (e.g., Hollenbach et al. 1991). This is consistent with the weak scaling we find in Orion B.

As a corollary, we conclude that our large-scale and spatially resolved lines maps of a local GMC show a variety of power-law indexes, $I_{FIR} \propto W^N$ (or $W \propto I_{FIR}^{1/N}$). These N indexes resemble the kind of Kennicutt-Schmidt power-law indexes, SFR $\propto L_{mol}^N$, found in galaxy surveys that average multiple GMCs (e.g., Wu et al. 2005, 2010; Kennicutt & Evans 2012; García-Burillo et al. 2012; Sánchez-García et al. 2022). We attribute the different scalings in Orion B to the different gas densities, excitation regimes, and chemistry of the star-forming (dense and compact) versus non-star-forming (low density, extended, and FUV-illuminated) environments. However, while it is tempting to extrapolate our results to the extragalactic scalings (as in Krumholz & Thompson 2007; Narayanan et al. 2008), we still need to better understand the spatial scales at which L_{FIR} becomes a reliable tracer of the global SFR, as well as the connection between the extragalactic averages versus our spatially resolved scalings.

7. Summary and conclusions

In the context of the IRAM 30m ORION-B large program, we presented a detailed analysis of 5 deg^2 ($\sim$250 pc^2) HCN, HNC, HCO$^+$, CO $J = 1–0$, and [C I] 492 GHz line emission maps of the Orion B GMC. We complemented this dataset with new pointed observations of rotationally excited HCN, HNC, H^{13}CN, and HN^{13}C lines. We constructed integrated line intensity (W), visual extinction, and I_{FIR} (a proxy of G_0) maps from existing dust SED observations. We summarize our results as follows:

– About 70% of the total HCN $J = 1–0$ luminosity, L'(HCN $J = 1–0$) = 110 K km s^{-1} pc^{-2}, arises from gas at $A_V < 8$ mag (Sect. 3.1), that is, from gas below the common extinction threshold of star-forming cores. About 80% of the total cloud mass and 50% of the total FIR luminosity (mostly arising from FUV-heated dust grains) also stems from $A_V < 8$ mag.

– We detect anomalous HCN $J = 1–0$ HFS line intensity ratios (also in the HCN $J = 2–1$ and 3–2 transitions) almost everywhere in the cloud (Sect. 4.4). That is, HCN $J = 1–0$ $R_{02} = W(F = 0–1)/W(F = 2–1)$ and $R_{12} = W(F = 1–1)/W(F = 2–1)$ hyperfine line intensity ratios outside the LTE range $R_{02} = [0.2, 1]$ and $R_{12} = [0.6, 1]$. We also detect anomalous HFS line width ratios. That is, $\Delta v(F = 0–1) \neq \Delta v(F = 2–1) \neq \Delta v(F = 1–1)$ (Sect. 4.2). Radiative effects induced by moderate line opacities and HFS line overlaps produce these anomalous ratios, which are inconsistent with the common assumption of the same T_{ex} and line width for all HFS lines of a given rotational transition.

– Most of the widespread and extended HCN $J = 1–0$ emission arises from weakly collisionally excited gas with $n(H_2) \lesssim 10^4$ cm^{-3}. That is, it is not line radiation emitted by dense cores that is resonantly scattered by low density halos (Sect. 6.1). This is demonstrated by the typical HCN $J = 1–0$ HFS intensity ratios $R_{02} \gtrsim 0.2$ and $R_{12} < 0.6$ observed at large scales. Even lower densities are possible in FUV-illuminated gas if $\chi_e \gtrsim 10^{-5}$ and electron collisional excitation dominates (Sect. 4.3).

– The HCN/HNC $J = 1–0$ line intensity ratio is sensitive to the strength of the FUV radiation field. Our chemical models and observations suggest that the HCN/HNC abundance ratio is more sensitive to G_0 than to T_k (Sect. 5). In particular, HNC is a slightly better tracer of dense gas, defined as $n(H_2) > 10^4$ cm^{-3}, than HCN, because its abundance is lower in the FUV-illuminated gas (translucent gas and cloud edges). This gas is usually at lower density than the FUV-shielded cold gas. In addition, HNC is less sensitive to electron excitation than HCN (Table 1).

– The HCN/CO $J = 1–0$ line intensity ratio (Sect. 3.2), widely used as a tracer of the dense gas fraction, shows a bimodal behavior with respect to A_V, with an inflection point at $A_V \lesssim 3$ mag (Sect. 6.2) typical of translucent gas and FUV-illuminated cloud edges. The extended cloud HCN $J = 1–0$ emission (Sect. 4.3) explains the low A_V branch of the observed distribution of the HCN/CO $J = 1–0$ line intensity ratio. The highest HCN/CO $J = 1–0$ line intensity ratios (~ 0.1) at $A_V < 3$ mag correspond to regions displaying high [C I] 492 GHz/CO $J = 1–0$ intensity ratios too (> 1). These values are characteristic of low-density PDRs and $\chi_e \gtrsim 10^{-5}$. Therefore, we conclude that the detection of high HCN/CO $J = 1–0$ intensity ratios does not always imply the presence of dense gas.

– Given the widespread and extended nature of the [C I] 492 GHz emission (a typical tracer of PDR gas), and its spatial correlation with W(HCO$^+$ $J = 1–0$), W(HCN $J = 1–0$), and W(^{13}CO $J = 1–0$) (see Sect. 6.2.1), the extended component of Orion B (and likely in most GMCs), must be porous to FUV radiation from nearby massive stars. Indeed, 70% of the total [C I] 492 GHz luminosity arises from lines of sight with $A_V > 3$ mag (i.e., not exactly from the cloud surface). In addition, the 70 μm continuum emission from FUV-illuminated dust grains is very extended. The enhanced FUV field favors the formation of HCN and the excitation of the $J = 1–0$ line at large scales, not only in dense star-forming cores. This is exemplified by the relatively low value of the dense gas mass to the HCN $J = 1–0$ line luminosity ratio, α(HCN) = 29 $M_\odot$/K km s^{-1} pc^2, in Orion B (Sect. 6.3). The existence of a widespread HCN $J = 1–0$ emission component associated with low density gas affects the interpretation of the extragalactic relationship L_{HCN} versus SFR.

– The low-surface brightness and extended HCN $J = 1–0$ and HCO$^+$ $J = 1–0$ emissions ($\lesssim 1$ K km s^{-1}) scale with I_{FIR} with a similar power-law index (Sect. 6.4). Together with CO $J = 1–0$, these lines respond to the increasing I_{FIR} up to $G_0' \simeq 20$. On the other hand, the bright HCN emission (> 6 K km s^{-1}) from dense gas in star-forming clumps weakly responds to I_{FIR} once the FUV radiation field becomes too intense ($G_0' > 1500$). HNC $J = 1–0$ and [C I] 492 GHz lines weakly respond to I_{FIR} at all G_0'.

– Our large-scale and spatially resolved lines maps of a local GMC show a variety of power-law indexes, $I_{FIR} \propto W^N$ (from sublinear to superlinear), that resemble the kind of Kennicutt-Schmidt power-law indexes, SFR $\propto L_{mol}^N$, found in surveys of different galaxy types that spatially average multiple GMCs (e.g., Kennicutt & Evans 2012). We attribute the different scalings in Orion B to the different gas densities, excitation regimes, and chemistry of the star-forming (compact) versus non-star-forming (extended) environments (Sect. 6.4).

Our study stresses the major contribution of the extended and low density component of GMCs to the total CO, HCO$^+$, and HCN $J = 1$–0 line luminosity. It also enables us to remark that there is a need to carry out sensitive wide field surveys of galactic GMCs in multiple molecular lines. This will allow us to determine the properties of the star formation environment and to better understand the origin of the extragalactic Kennicutt-Schmidt scalings on global galaxy averages. In Orion B, the HCN $J = 1$–0 line intensity at any position of the extended cloud component is obviously much fainter than that arising from dense star-forming clumps such as NGC 2024. However, the much larger area of the extended cloud component at low A_V implies that the emission arising from dense cores does not dominate the HCN $J = 1$–0 line luminosity from GMCs (see also Santa-Maria et al. 2021). Finally, better knowledge of the rate coefficient of some critical gas-phase reactions, namely reaction NCO + N → HCN + O and reactions of HNC with H, C, and O atoms, will help us to refine our abundance estimations from chemical models.

References

Abergel, A., Teyssier, D., Bernard, J. P., et al. 2003, A&A, 410, 577
Abt, H. A., & Levato, H. 1977, PASP, 89, 797
Aguado, A., Roncero, O., Zanchet, A., Agúndez, M., & Cernicharo, J. 2017, ApJ, 838, 33
Ahrens, V., Lewen, F., Takano, S., et al. 2002, Z. Naturfor. A, 57, 669
André, P., Men'shchikov, A., Bontemps, S., et al. 2010, A&A, 518, A102
Anthony-Twarog, B. J. 1982, AJ, 87, 1213
Bally, J., Chambers, E., Guzman, V., et al. 2018, AJ, 155, 80
Barnes, P. J., Crutcher, R. M., Bieging, J. H., Storey, J. W. V., & Willner, S. P. 1989, ApJ, 342, 883
Barnes, P. J., Ryder, S. D., O'Dougherty, S. N., et al. 2013, MNRAS, 432, 2231
Barnes, A. T., Kauffmann, J., Bigiel, F., et al. 2020, MNRAS, 497, 1972
Behrens, E., Mangum, J. G., Holdship, J., et al. 2022, ApJ, 939, 119
Bik, A., Lenorzer, A., Kaper, L., et al. 2003, A&A, 404, 249
Bisbas, T. G., Schruba, A., & van Dishoeck, E. F. 2019, MNRAS, 485, 3097
Blake, G. A., Sutton, E. C., Masson, C. R., & Phillips, T. G. 1987, ApJ, 315, 621
Boger, G. I., & Sternberg, A. 2005, ApJ, 632, 302
Boisse, P. 1990, A&A, 228, 483
Bowler, B. P., Waller, W. H., Megeath, S. T., Patten, B. M., & Tamura, M. 2009, AJ, 137, 3685
Branham, Richard L., J. 1995, Celest. Mech. Dyn. Astron., 61, 239
Bublitz, J., Kastner, J. H., Santander-García, M., et al. 2019, A&A, 625, A101
Bublitz, J., Kastner, J. H., Hily-Blant, P., et al. 2022, A&A, 659, A197
Carilli, C. L., & Walter, F. 2013, ARA&A, 51, 105
Caselli, P., Walmsley, C. M., Terzieva, R., & Herbst, E. 1998, ApJ, 499, 234
Cernicharo, J., Castets, A., Duvert, G., & Guilloteau, S. 1984a, A&A, 139, L13
Cernicharo, J., Guelin, M., & Askne, J. 1984b, A&A, 138, 371
Chandler, C. J., & Carlstrom, J. E. 1996, ApJ, 466, 338

Choi, M., Kang, M., & Lee, J.-E. 2015, AJ, 150, 29
Clark, F. O., Buhl, D., & Snyder, L. E. 1974, ApJ, 190, 545
Dame, T. M., & Lada, C. J. 2023, ApJ, 944, 197
Daniel, F., & Cernicharo, J. 2008, A&A, 488, 1237
Denis-Alpizar, O., Stoecklin, T., Dutrey, A., & Guilloteau, S. 2020, MNRAS, 497, 4276
Dickinson, A. S., Phillips, T. G., Goldsmith, P. F., Percival, I. C., & Richards, D. 1977, A&A, 54, 645
Elmegreen, B. G. 2002, ApJ, 577, 206
Emprechtinger, M., Wiedner, M. C., Simon, R., et al. 2009, A&A, 496, 731
Endres, C. P., Schlemmer, S., Schilke, P., Stutzki, J., & Müller, H. S. 2016, J. Mol. Spectrosc., 327, 95, new Visions of Spectroscopic Databases, Volume II
Evans, Neal J., I. 1999, ARA&A, 37, 311
Evans, Neal J., I., Kim, K.-T., Wu, J., et al. 2020, ApJ, 894, 103
Falgarone, E., Phillips, T. G., & Walker, C. K. 1991, ApJ, 378, 186
Faure, A., & Lique, F. 2012, MNRAS, 425, 740
Faure, A., Tennyson, J., Varambhia, H. N., et al. 2007a, in SF2A-2007: Proceedings of the Annual meeting of the French Society of Astronomy and Astrophysics, eds. J. Bouvier, A. Chalabaev, & C. Charbonnel, 244
Faure, A., Varambhia, H. N., Stoecklin, T., & Tennyson, J. 2007b, MNRAS, 382, 840
Faure, A., Tennyson, J., Kokoouline, V., & Greene, C. H. 2009, in J. Phys. Conf. Ser., 192, 012016
Fuller, G. A., Myers, P. C., Welch, W. J., et al. 1991, ApJ, 376, 135
Gallagher, M. J., Leroy, A. K., Bigiel, F., et al. 2018, ApJ, 868, L38
Gao, Y., & Solomon, P. M. 2004a, ApJS, 152, 63
Gao, Y., & Solomon, P. M. 2004b, ApJ, 606, 271
Gao, Y., Carilli, C. L., Solomon, P. M., & Vanden Bout, P. A. 2007, ApJ, 660, L93
García-Burillo, S., Usero, A., Alonso-Herrero, A., et al. 2012, A&A, 539, A8
Gaudel, M., Orkisz, J. H., Gerin, M., et al. 2023, A&A, 670, A59
Gaume, R. A., Johnston, K. J., & Wilson, T. L. 1992, ApJ, 388, 489
Gerin, M., Goicoechea, J. R., Pety, J., & Hily-Blant, P. 2009, A&A, 494, 977
Giannini, T., Nisini, B., Lorenzetti, D., et al. 2000, A&A, 358, 310
Godard, B., Falgarone, E., Gerin, M., Hily-Blant, P., & de Luca, M. 2010, A&A, 520, A20
Goicoechea, J. R., & Cuadrado, S. 2021, A&A, 647, A7
Goicoechea, J. R., & Le Bourlot, J. 2007, A&A, 467, 1
Goicoechea, J. R., & Roncero, O. 2022, A&A, 664, A190
Goicoechea, J. R., Pety, J., Gerin, M., Hily-Blant, P., & Le Bourlot, J. 2009, A&A, 498, 771
Goicoechea, J. R., Pety, J., Cuadrado, S., et al. 2016, Nature, 537, 207
Goicoechea, J. R., Lique, F., & Santa-Maria, M. G. 2022, A&A, 658, A28
Goldsmith, P. F., & Kauffmann, J. 2017, ApJ, 841, 25
Goldsmith, P. F., & Langer, W. D. 1999, ApJ, 517, 209
Goldsmith, P. F., Snell, R. L., Hemeon-Heyer, M., & Langer, W. D. 1984, ApJ, 286, 599
Gonzalez-Alfonso, E., & Cernicharo, J. 1993, A&A, 279, 506
Gottlieb, C. A., Lada, C. J., Gottlieb, E. W., Lilley, A. E., & Litvak, M. M. 1975, ApJ, 202, 655
Graninger, D. M., Herbst, E., Öberg, K. I., & Vasyunin, A. I. 2014, ApJ, 787, 74
Guelin, M., Langer, W. D., & Wilson, R. W. 1982, A&A, 107, 107
Guilloteau, S., & Baudry, A. 1981, A&A, 97, 213
Habart, E., Abergel, A., Walmsley, C. M., Teyssier, D., & Pety, J. 2005, A&A, 437, 177
Habart, E., Le Gal, R., Alvarez, C., et al. 2023a, A&A, 673, A149
Habart, E., Peeters, E., Berne, O., et al. 2023b, A&A, in press, https://doi.org/10.1051/0004-6361/202346747
Hacar, A., Bosman, A. D., & van Dishoeck, E. F. 2020, A&A, 635, A4
Heays, A. N., Bosman, A. D., & van Dishoeck, E. F. 2017, A&A, 602, A105
Helfer, T. T., & Blitz, L. 1997, ApJ, 478, 233
Herbst, E., Terzieva, R., & Talbi, D. 2000, MNRAS, 311, 869
Hernández Vera, M., Lique, F., Dumouchel, F., Hily-Blant, P., & Faure, A. 2017, MNRAS, 468, 1084
Hily-Blant, P., Walmsley, M., Pineau Des Forêts, G., & Flower, D. 2010, A&A, 513, A41
Hollenbach, D. J., Takahashi, T., & Tielens, A. G. G. M. 1991, ApJ, 377, 192
Hollenbach, D. J., & Tielens, A. G. G. M. 1999, Rev. Mod. Phys., 71, 173
Ikeda, M., Oka, T., Tatematsu, K., Sekimoto, Y., & Yamamoto, S. 2002, ApJS, 139, 467
Indriolo, N., Neufeld, D. A., Gerin, M., et al. 2015, ApJ, 800, 40
Jiménez-Donaire, M. J., Bigiel, F., Leroy, A. K., et al. 2017, MNRAS, 466, 49
Jiménez-Donaire, M. J., Bigiel, F., Leroy, A. K., et al. 2019, ApJ, 880, 127
Johnson, C. T., Burke, P. G., & Kingston, A. E. 1987, J. Phys. B At. Mol. Phys., 20, 2553
Kaufman, M. J., Wolfire, M. G., Hollenbach, D. J., & Luhman, M. L. 1999, ApJ, 527, 795

Kauffmann, J., Goldsmith, P. F., Melnick, G., et al. 2017, A&A, 605, A5
Kennicutt, R. C., J. 1998a, ARA&A, 36, 189
Kennicutt, R. C., J. 1998b, ApJ, 498, 541
Kennicutt, R. C., & Evans, N. J. 2012, ARA&A, 50, 531
Keto, E., & Rybicki, G. 2010, ApJ, 716, 1315
Könyves, V., André, P., Arzoumanian, D., et al. 2020, A&A, 635, A34
Krumholz, M. R., & Thompson, T. A. 2007, ApJ, 669, 289
Kwan, J., & Scoville, N. 1975, ApJ, 195, L85
Lada, E. A. 1992, ApJ, 393, L25
Lada, C. J., & Lada, E. A. 2003, ARA&A, 41, 57
Lada, E. A., Evans, Neal J., I., & Falgarone, E. 1997, ApJ, 488, 286
Lada, C. J., Lombardi, M., & Alves, J. F. 2010, ApJ, 724, 687
Langer, W. D., & Penzias, A. A. 1990, ApJ, 357, 477
Langer, W. D., Wilson, R. W., Henry, P. S., & Guelin, M. 1978, ApJ, 225, L139
Le Petit, F., Nehmé, C., Le Bourlot, J., & Roueff, E. 2006, ApJS, 164, 506
Lim, J., Dinh-V-Trung, Vrtilek, J., David, L. P., & Forman, W. 2017, ApJ, 850, 31
Lin, M. C., Yinsheng, H., & Melius, C. 1992, Int. J. Chem. Kinet., 24, 1103
Liszt, H. S. 2012, A&A, 538, A27
Liszt, H., & Lucas, R. 2001, A&A, 370, 576
Liszt, H. S., & Pety, J. 2016, ApJ, 823, 124
Loison, J. C., & Hickson, K. M. 2015, Chem. Phys. Lett., 635, 174
Loison, J.-C., Wakelam, V., & Hickson, K. M. 2014, MNRAS, 443, 398
Lombardi, M., Bouy, H., Alves, J., & Lada, C. J. 2014, A&A, 566, A45
Loughnane, R. M., Redman, M. P., Thompson, M. A., et al. 2012, MNRAS, 420, 1367
Madore, B. F. 1977, MNRAS, 178, 1
Magalhães, V. S., Hily-Blant, P., Faure, A., Hernandez-Vera, M., & Lique, F. 2018, A&A, 615, A52
McDowell, R. S. 1988, J. Chem. Phys., 88, 356
Megeath, S. T., Gutermuth, R., Muzerolle, J., et al. 2016, AJ, 151, 5
Meyer, M. R., Flaherty, K., Levine, J. L., et al. 2008, in Handbook of Star Forming Regions, 4, ed. B. Reipurth, 662
Mezger, P. G., Chini, R., Kreysa, E., Wink, J. E., & Salter, C. J. 1988, A&A, 191, 44
Miettinen, O., Harju, J., Haikala, L. K., Kainulainen, J., & Johansson, L. E. B. 2009, A&A, 500, 845
Miettinen, O., Harju, J., Haikala, L. K., & Juvela, M. 2010, A&A, 524, A91
Mitchell, G. F. 1984, ApJS, 54, 81
Narayanan, D., Cox, T. J., Shirley, Y., et al. 2008, ApJ, 684, 996
Neumann, L., Gallagher, M. J., Bigiel, F., et al. 2023, MNRAS, 521, 3348
O'Konski, C. T., & Ha, T.-K. 1968, J. Chem. Phys., 49, 5354
Orkisz, J. H., Peretto, N., Pety, J., et al. 2019, A&A, 624, A113
Pabst, C. H. M., Goicoechea, J. R., Teyssier, D., et al. 2017, A&A, 606, A29
Pabst, C. H. M., Hacar, A., Goicoechea, J. R., et al. 2021, A&A, 651, A111
Papadopoulos, P. P., Zhang, Z.-Y., Xilouris, E. M., et al. 2014, ApJ, 788, 153
Patra, S., Evans, Neal J., I., Kim, K.-T., et al. 2022, AJ, 164, 129
Petrie, S. 2002, J. Phys. Chem. A, 106, 11181
Pety, J., Goicoechea, J. R., Hily-Blant, P., Gerin, M., & Teyssier, D. 2007, A&A, 464, L41
Pety, J., Gratier, P., Guzmán, V., et al. 2012, A&A, 548, A68
Pety, J., Guzmán, V. V., Orkisz, J. H., et al. 2017, A&A, 599, A98
Philipp, S. D., Lis, D. C., Güsten, R., et al. 2006, A&A, 454, 213
Pickering, E. C. 1908, Ann. Harvard Coll. Observ., 60, 147
Ren, Z., & Li, D. 2016, ApJ, 824, 52
Rezaei Kh., S., Bailer-Jones, C. A. L., Soler, J. D., & Zari, E. 2020, A&A, 643, A151
Rosolowsky, E., Pineda, J. E., & Gao, Y. 2011, MNRAS, 415, 1977
Rybak, M., Hodge, J. A., Greve, T. R., et al. 2022, A&A, 667, A70
Sánchez-García, M., García-Burillo, S., Pereira-Santaella, M., et al. 2022, A&A, 660, A83
Sandell, G., Mookerjea, B., Güsten, R., et al. 2015, A&A, 578, A41
Sanders, D. B., & Mirabel, I. F. 1996, ARA&A, 34, 749
Santa-Maria, M. G., Goicoechea, J. R., Etxaluze, M., Cernicharo, J., & Cuadrado, S. 2021, A&A, 649, A32
Schaefer, G. H., Hummel, C. A., Gies, D. R., et al. 2016, AJ, 152, 213
Schilke, P., Walmsley, C. M., Pineau Des Forets, G., et al. 1992, A&A, 256, 595
Schmidt, M. 1959, ApJ, 129, 243
Schmidt, M. 1963, ApJ, 137, 758
Schneider, N., André, P., Könyves, V., et al. 2013, ApJ, 766, L17
Schroder, K., Staemmler, V., Smith, M. D., Flower, D. R., & Jaquet, R. 1991, J. Phys. B At. Mol. Phys., 24, 2487
Semaniak, J., Minaev, B. F., Derkatch, A. M., et al. 2001, ApJS, 135, 275
Shetty, R., Kelly, B. C., & Bigiel, F. 2013, MNRAS, 430, 288
Shetty, R., Clark, P. C., & Klessen, R. S. 2014a, MNRAS, 442, 2208
Shetty, R., Kelly, B. C., Rahman, N., et al. 2014b, MNRAS, 437, L61
Shimajiri, Y., André, P., Braine, J., et al. 2017, A&A, 604, A74
Shirley, Y. L. 2015, PASP, 127, 299

Shirley, Y. L., Wu, J., Shane Bussmann, R., & Wootten, A. 2008, in ASP Conf. Ser., 387, Massive Star Formation: Observations Confront Theory, eds. H. Beuther, H. Linz, & T. Henning, 401
Sofia, U. J., Lauroesch, J. T., Meyer, D. M., & Cartledge, S. I. B. 2004, ApJ, 605, 272
Sohn, J., Lee, C. W., Park, Y.-S., et al. 2007, ApJ, 664, 928
Solomon, P. M., Downes, D., & Radford, S. J. E. 1992, ApJ, 387, L55
Spaans, M. 1996, A&A, 307, 271
Stephens, I. W., Jackson, J. M., Whitaker, J. S., et al. 2016, ApJ, 824, 29
Sternberg, A., & Dalgarno, A. 1995, ApJS, 99, 565
Stutzki, J., Bensch, F., Heithausen, A., Ossenkopf, V., & Zielinsky, M. 1998, A&A, 336, 697
Sumathi, R., & Nguyen, M. T. 1998, J. Phys. Chem. A, 102, 8013
Tafalla, M., Usero, A., & Hacar, A. 2021, A&A, 646, A97
Talbi, D., Ellinger, Y., & Herbst, E. 1996, A&A, 314, 688
Turner, B. E., Pirogov, L., & Minh, Y. C. 1997, ApJ, 483, 235
Usero, A., Leroy, A. K., Walter, F., et al. 2015, AJ, 150, 115
Virtanen, P., Gommers, R., Oliphant, T. E., et al. 2020, Nat. Methods, 17, 261
Walmsley, C. M., Churchwell, E., Nash, A., & Fitzpatrick, E. 1982, ApJ, 258, L75
Walter, F. M., Sherry, W. H., Wolk, S. J., & Adams, N. R. 2008, in Handbook of Star Forming Regions, Volume I, 732, ed. B. Reipurth, 732
Wannier, P. G., Encrenaz, P. J., Wilson, R. W., & Penzias, A. A. 1974, ApJ, 190, L77
Wu, J., Evans, Neal J., I., Gao, Y., et al. 2005, ApJ, 635, L173
Wu, J., Evans, Neal J., I., Shirley, Y. L., & Knez, C. 2010, ApJS, 188, 313
Yamada, M., Wada, K., & Tomisaka, K. 2007, ApJ, 671, 73
Yang, B., Stancil, P. C., Balakrishnan, N., & Forrey, R. C. 2010, ApJ, 718, 1062
Young Owl, R. C., Meixner, M. M., Wolfire, M., Tielens, A. G. G. M., & Tauber, J. 2000, ApJ, 540, 886
Zucker, C., Speagle, J. S., Schlafly, E. F., et al. 2019, ApJ, 879, 125
Zymak, I., Hejduk, M., Mulin, D., et al. 2013, ApJ, 768, 86

[1] Instituto de Física Fundamental (CSIC), Calle Serrano 121-123, 28006, Madrid, Spain,
e-mail: miriam.g.sm@csic.es
[2] IRAM, 300 rue de la Piscine, 38406 Saint-Martin-d'Hères, France
[3] LERMA, Observatoire de Paris, PSL Research University, CNRS, Sorbonne Universités, 75014 Paris, France
[4] Chalmers University of Technology, Department of Space, Earth and Environment, 412 93 Gothenburg, Sweden
[5] LERMA, Observatoire de Paris, PSL Research University, CNRS, Sorbonne Universités, 92190 Meudon, France
[6] Univ. Grenoble Alpes, Inria, CNRS, Grenoble INP, GIPSA-Lab, Grenoble 38000, France
[7] Univ. Lille, CNRS, Centrale Lille, UMR 9189 – CRIStAL, 59651 Villeneuve d'Ascq, France
[8] Université de Toulon, Aix-Marseille Univ., CNRS, IM2NP, 83041 Toulon, France
[9] Laboratoire d'Astrophysique de Bordeaux, Univ. Bordeaux, CNRS, B18N Allée Geoffroy Saint-Hilaire, 33615 Pessac, France
[10] Instituto de Astrofísica, Pontificia Universidad Católica de Chile, Av. Vicuña Mackenna 4860, 7820436 Macul, Santiago, Chile
[11] Institut de Recherche en Astrophysique et Planétologie (IRAP), Université Paul Sabatier, 9 av. du Colonel Roche, BP 44346, 31028 Toulouse cedex 4, France
[12] Laboratoire de Physique de l'École normale supérieure, ENS, Université PSL, CNRS, Sorbonne Université, Université de Paris, Sorbonne Paris Cité, 24 rue Lhomond, 75005 Paris, France
[13] Jet Propulsion Laboratory, California Institute of Technology, 4800 Oak Grove Drive, Pasadena, CA 91109, USA
[14] National Radio Astronomy Observatory, 520 Edgemont Road, Charlottesville, VA 22903, USA
[15] Department of Physics, The University of Tokyo, 7-3-1, Hongo, Bunkyo-ku, Tokyo 113-0033, Japan
[16] Research Center for the Early Universe, The University of Tokyo, 7-3-1, Hongo, Bunkyo-ku, Tokyo, 113-0033, Japan
[17] Harvard-Smithsonian Center for Astrophysics, 60 Garden Street, Cambridge, MA 02138, USA
[18] School of Physics and Astronomy, Cardiff University, Queen's buildings, Cardiff CF24 3AA, UK

Appendix A: Main regions in Orion B

In this Appendix we provide more details about the properties of the main regions in Orion B discussed in this work (see Fig. 2).

— NGC 2024: also known as the Flame nebula, is located east of the belt star Alnitak (ζ Ori). This is an active massive star-forming region, with the highest H_2 column density ($\sim 5 \times 10^{23}$ cm^{-2}) and star formation efficiency (SFE$\sim$30%, Lada et al. 1997) in Orion B. It is composed of an embedded stellar cluster and associated H II region (Barnes et al. 1989). Inside the molecular ridge behind the H II region, FIR and radio observations reveal the presence of embedded dense cores, protostars, and YSOs (Mezger et al. 1988; Gaume et al. 1992; Chandler & Carlstrom 1996; Choi et al. 2015; Ren & Li 2016; Könyves et al. 2020). The bulk of the FIR line emission arises from an extended PDR, with $T_k \simeq$75-100 K and $n(H_2) \simeq 10^6$ cm^{-3}. This region is illuminated by ionizing and dissociating UV photons from a massive star (e.g., Giannini et al. 2000; Emprechtinger et al. 2009). The dominant ionizing source is likely the late-O or early-B star IRS2b (Bik et al. 2003; Meyer et al. 2008).

— NGC 2023: is a reflection nebula located 20′ south of NGC 2024 (Meyer et al. 2008). It is illuminated by a B1.5V star (Abt & Levato 1977). This is a filamentary massive star-forming region (Könyves et al. 2020; Gaudel et al. 2023), with a FUV radiation flux equivalent to a few 10^4 times the mean interstellar radiation field (G_0) toward the [C II] 158 μm emission peak (e.g., Sandell et al. 2015).

— The Horsehead nebula[13]: also known as Barnard 33, is a dense pillar seen projected against the bright H II region and ionization front IC 434. The multiple stellar system, σ Orionis, formed by an O9.5V and a B0.5V binary, photoionizes the region (Walter et al. 2008). The Horsehead and all the western rim of the Orion B cloud is a large scale PDR eroded by UV radiation from σ Ori. The molecular cloud is located at a projected distance of $\sim$4 pc from the ionizing stars, resulting in a moderate incident FUV flux, $G_0 \simeq 100$ (Abergel et al. 2003). The expansion of the H II region likely triggers gas compression along the cloud rim and perhaps star-formation (Bally et al. 2018). The Horsehead pillar points radially to the ionizing source, and its western edge is a PDR observed nearly edge-on. This region hosts a few dense cores, protostars and YSOs (Bowler et al. 2009; Könyves et al. 2020). The gas temperature ranges from $\sim$100 K (at the FUV-illuminated edge) to 10-20 K deeper inside the cloud (e.g., Habart et al. 2005; Pety et al. 2007; Goicoechea et al. 2009).

— Orion B9: is an active low-mass star-forming region composed of supercritical filaments hosting pre- and proto-stellar cores (Miettinen et al. 2009, 2010). Line observations resolve two different velocity components at about v_{LSR}=0-4 km s^{-1} and 8-10 km s^{-1}, respectively (e.g., Gaudel et al. 2023).

— The Flame filament: is physically connected with NGC 2024, at the southeast of NGC 2024. This is a very structured filament (Orkisz et al. 2019; Gaudel et al. 2023).

— The Hummingbird filament: is one of the longest isolated filaments in the observed field. Only a few embedded YSOs exist in this region (Orkisz et al. 2019).

— The Cloak: is a filamentary structure that crosses Orion B from east to west (Gaudel et al. 2023). Embedded starless and prestellar cores exist in the region (Könyves et al. 2020).

---

[13] Discovered by Williamina Fleming (Pickering 1908).

Appendix B: Line intensities, line intensity ratios, and their relation to A_V and I_{FIR}

In this Appendix we show 2D histograms that display the relationship between line intensity ratios, A_V, and I_{FIR}. In Sect. 6.2 we discussed the behavior of the HCN/CO $J=1-0$ line intensity ratio with A_V and its relation to the [C I]/CO $J=1-0$ line intensity ratio. In Sect. 5.3 we discussed the HCN/HNC abundance ratio and its possible relation with G_0. In addition, Fig. B.3 shows 2D histograms of the relation between line intensities and I_{FIR}, showing the exponents $W \propto I_{FIR}^{1/N}$ (see Sect. 6.4).
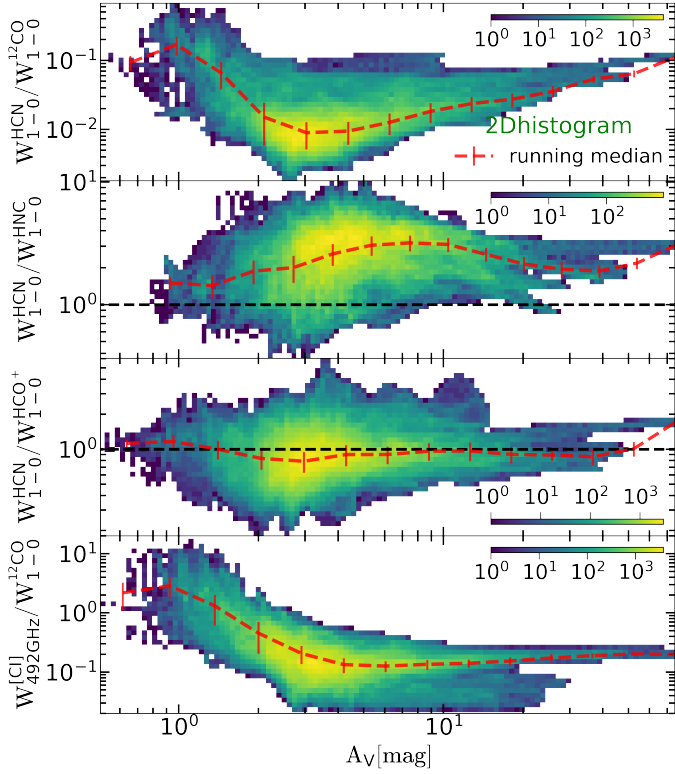
Fig. B.1. 2D histograms showing the line intensity ratios HCN/CO, HCN/HNC, HCN/HCO$^+$ $J=1-0$, and [C I] 492 GHz/CO $J=1-0$ with respect to the visual extinction A_V. The dashed red line marks the running median. The error bars mark the standard deviation. The dashed black line marks the intensity ratio equal to one.
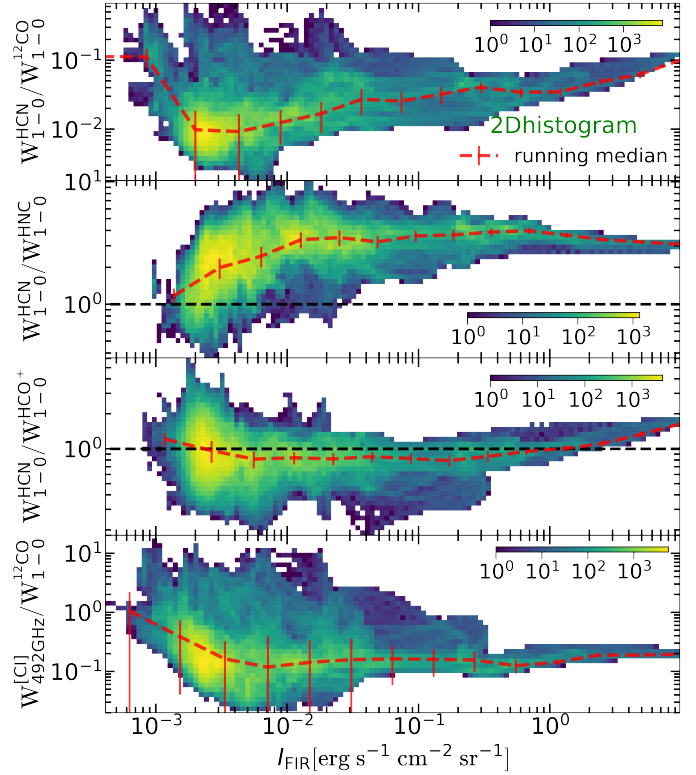
Fig. B.2. Same as Fig. B.1 but as a function of I_{FIR}.
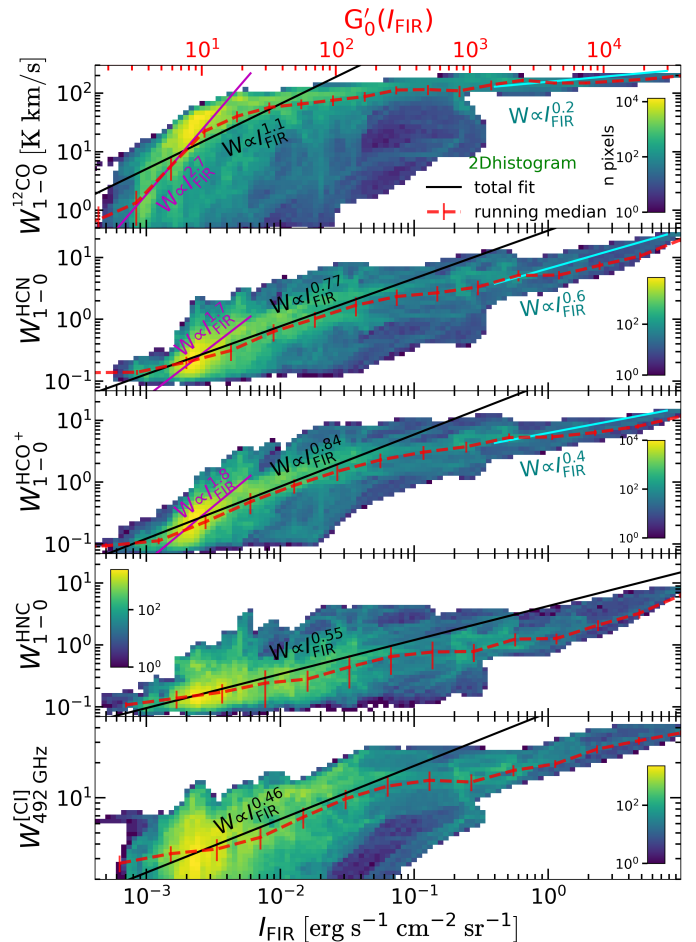
Fig. B.3. Same as Fig. 18 but showing the exponents $W \propto I_{FIR}^{1/N}$ (see text).

Appendix C: SED-derived parameters

C.1. Dust temperature and column density maps

In previous papers (e.g., Pety et al. 2017), we have used dust temperature and column density maps derived from the maps published by Lombardi et al. (2014), based on *Herschel* and *Planck* data. More recently, similar maps have been published by Könyves et al. (2020) as part of the HGBS (André et al. 2010; Schneider et al. 2013)[14].

The Könyves et al. (2020) maps benefit from additional *Herschel* observations, which were used to correct a small patch of pixels where the SPIRE detectors are saturated in the NGC 2024 region in the original data (Fig. C.1). This saturation creates an artifact in the maps derived by Lombardi et al. (2014). However, the two datasets, which in principle use essentially the same observational data and the same derivation method (modified black-body SED fitting) display some discrepancies (typically a factor of 1.2 – 1.5 in temperature and a factor 1.2 – 2 in column density), which can partly be attributed to the fact that Könyves et al. (2020) use a fixed value of zero-point calibrations for the *Herschel* bands and a fixed β index for the modified black body, whereas Lombardi et al. (2014) use spatially varying values for these parameters based on previous SED fitting of *Planck* and IRAS data.

For the sake of consistency with our previous work and due to the level of detail of its SED fitting, we chose to keep the Lombardi et al. (2014) data as our reference, but we incorporated the newly available reobserved patch in NGC 2024 by rescaling the Könyves et al. (2020) maps and compositing them into the Lombardi et al. (2014) maps (hereafter K20 and L14 maps respectively), as illustrated in Fig. C.1.

The compositing procedure for both column density and temperature was the following:

1. The saturated patch in NGC 2024 is masked out as tightly as possible, with a $81'' \times 216''$ (9×24 pixels) mask.

2. A $36''$ wide (4 pixels, about one beam) border is selected around the masked patch, yielding a $153'' \times 288''$ selection region.

3. From this we obtain a correction constant A_X corresponding to the local ratio between the datasets:

$$A_X = \langle X_{K20}/X_{L14} \rangle_{\text{selection}} \tag{C.1}$$

where X corresponds to N or T.

4. The $153'' \times 288''$ binary mask is then smoothed with a Hann window of radius 45" (4/3 beam) to avoid compositing artifacts. This yields a gray-scale mask M, with value 1 in most of the map, 0.5 at the edge of the compositing region, and 0 at the center of the NGC 2024 region.

5. The two datasets are finally merged into a final column density map N or a final temperature map T:

$$X = M \cdot X_{L14} + (1 - M) \cdot \frac{X_{K20}}{A} \tag{C.2}$$

where again X corresponds to N or T.

No significant discontinuity is visible in the combined datasets. Figure C.2 shows the spatial distribution of the dust temperature, the visual extinction, and integrated FIR intensity which are derived from these maps.

---

[14] The HGBS data can be found at http://www.herschel.fr/cea/star-formation/en/Phocea/Vie_des_labos/Ast/ast_visu.php?id_ast=66
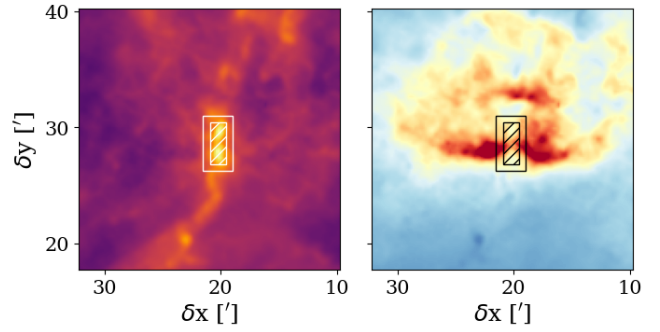
Fig. C.1. Compositing geometry in the NGC 2024 region between data from Lombardi et al. (2014) and Könyves et al. (2020), for column density (*left*) and dust temperature (*right*). The outer contour is the one in which the compositing is executed. The "selection area" over which the K20 datasets are rescaled to match the L14 ones corresponds to the outer contour minus the inner, hashed area (affected by the artifact in L14 and masked out). The full maps corresponding to these zoom-ins can be found in Fig. C.2

C.2. Determination of gas masses

We determined the mass of molecular gas as:

$$M_{H_2} = \mu\, m_H\, A_{\text{pixel}} \sum N(H_2) \tag{C.3}$$

where $N(H_2) = 1.9 \times 10^{21}\, A_V$, $\mu = 2.8$ is the molecular weight per H_2, m_H is the hydrogen atom mass, and A_{pixel} is the area of each pixel in cm^2. In Orion B, the total H_2 mass is $M_{H_2,\text{tot}} \sim 1.7 \times 10^4\, M_\odot$. The dense gas mass, M_{dg}, was computed for visual extinctions $A_V > 8$ mag (e.g., Lada et al. 2010; Shimajiri et al. 2017).

Appendix D: HCN hyperfine structure analysis

D.1. HCN J = 1–0 LTE-HFS fitting method

In Sect. 4.1 we determined $T_{\text{ex}}(J=1\text{–}0)$ and the opacity corrected column density $N^{\tau,\text{corr}}(\text{HCN})$ by applying the LTE-HFS fitting method implemented in CLASSfootnote 2. This method uses as input the line separation and the intrinsic line strengths of the $J=1\text{–}0$ HFS components, 1:5:3 (so that $S = 9$). The method assumes that the three HFS lines have the same T_{ex} and linewidth Δv. The output parameters are the linewidth $\Delta v = p_3$, the velocity of the reference component $v_{\text{LSR}} = p_2$, the sum of all the line center opacities such as $p_4\, S = \sum \tau_{\text{HFS},i}$, and the product of the antenna temperature and the line opacity $p_1 = T_a^* \tau$. This procedure allows one to derive the (LTE) excitation temperature as:

$$T_{\text{ex}} = T_{\text{bg}} + \frac{F_{\text{eff}}}{B_{\text{eff}}} \frac{p_1}{p_4} \tag{D.1}$$

where T_{bg} is the background temperature (~ 2.73 K), and $F_{\text{eff}}/B_{\text{eff}}$ is the ratio of the telescope forward and beam efficiencies (see CLASSfootnote 2 documentation). From the opacities and T_{ex}, we derive the opacity corrected column density, assuming Boltzmann populations at a single T_{ex} value:

$$N^{\tau,\text{corr}} = \frac{8\pi\nu^3}{A_{\text{ul}}\, c^3} \frac{Q(T_{\text{ex}})}{g_u} \frac{e^{E_u/kT_{\text{ex}}}}{e^{h\nu/kT_{\text{ex}}} - 1} \frac{W_{F=2-1}}{[J_\nu(T_{\text{ex}}) - J_\nu(T_{\text{bg}})]} \frac{\tau_{F=2-1}}{1 - e^{-\tau_{F=2-1}}}, \tag{D.2}$$
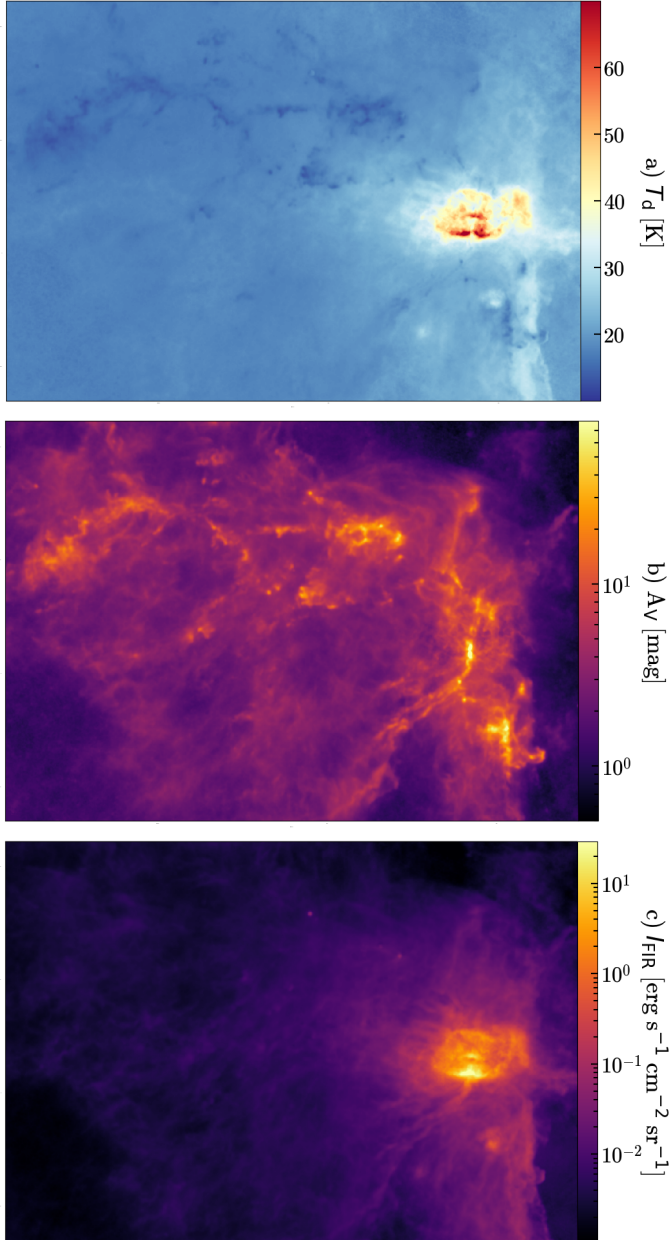
Fig. C.2. Maps of dust SED derived parameters at 30″ angular resolution. (a) Dust temperature, T_d. (b) Visual extinction, A_V. (c) FIR surface brightness (integrated from 40 to 500 μm).

Fig. D.1. HCN $J = 1$–0 HFS lines toward the Horsehead PDR. The right axis shows the normalized line intensity to make clear that the observed HFS emission differs from the optically thin LTE line ratios 1:5:3 (green lines). Red curves show the results of a non-LTE radiative transfer model including line overlaps (for details, see Sect. 5.1 in Goicoechea et al. 2022). Blue curves show the best LTE-HFS fit using CLASSfootnote 2.

where $W_{F=2-1}$ is the integrated intensity of the main HFS component $F=2$–1, $\tau_{F=2-1}$ is the line center opacity, $Q(T_{ex})$ is the partition function at a temperature of T_{ex}, g_u is the statistical weight of the transition upper level, and E_u/k is the upper level energy. The rotational partition function can be approximated with precision as:

$$Q(T_{ex}) \simeq \frac{k\,T_{ex}}{h\,B_0}\,e^{h\,B_0/3kT_{ex}}. \qquad (D.3)$$

where B_0 is the rotational constant (McDowell 1988). We took the HCN HFS spectroscopic parameters compiled in CDMS (Endres et al. 2016, and references therein).

This fitting method works better on high S/N spectra. Thus, we only applied it to the main cloud velocity component

($v_{LSR} \simeq 10$ km s^{-1}) where S/N$>5\sigma$. Figure D.1 shows the anomalous HCN $J=1$–0 spectrum observed (at by the IRAM 30m telescope toward the Horsehead PDR position $\delta v \simeq 0.16$ km s^{-1} resolution). This figure compares the expected HFS line strengths in the LTE and optically thin limit (green lines), the result of the LTE-HFS fit in CLASS (blue curve), and a non-LTE radiative transfer model (red curve, Goicoechea et al. 2022).

D.2. HCN J=2–1 and 3–2 HFS line ratios

The HCN $J=2$–1 transition has six HFS lines that blend into three lines with relative intensity ratios ~1:9:2 in the LTE and optically thin limit. The HCN $J=3$–2 transition also has six HFS lines. Only the central ones are blended and cannot be spectrally resolved. This gives the impression of three lines with relative intensity ratios 1:25:1 in the LTE and optically thin limit (e.g., Ahrens et al. 2002; Loughnane et al. 2012). Here we term these three apparent components (blueshifted, central, and redshifted) of the $J=2$–1 and $J=3$–2 rotational lines as "satellite(L)," "main," and "satellite(R)," respectively. Table D.1 provides the entries used to construct Fig.11.

Appendix E: HCN and HNC rotational diagrams

In Sect. 4.4, we analyzed multiple-J HCN and HNC line observations. Here we detail how we obtained the opacity corrected population diagrams. We took the HCN and HNC rotational spectroscopic parameters from CDMS (Endres et al. 2016, and references therein).

E.1. Estimation of line opacities:

To estimate the opacity of a given rotational transition HCN $J_u \rightarrow J_l$, we used the observed HCN/H^{13}CN line ratio. We

Table D.1. Observed HCN $J=2-1$ opacities (see Sect. E.1 for their definition), and HCN $J=2-1$ and $J=3-2$ HFS line intensity ratios satellite(R)/main and satellite(B)/main (see Sect. 4.4 for their definition) in the sample of representative positions.

Pos	HCN $J=2-1$	$J=2-1$		$J=3-2$	
	τ	Ratio satellite(B)/main	Ratio satellite(R)/main	Ratio satellite(B)/main	Ratio satellite(R)/main
#1	13.9	1.1±0.2	1.5±0.2	–	–
#2	1.7	0.15±0.02	0.38±0.38	0.12±0.006	0.14±0.004
#3	5	0.31±0.01	0.51±0.02	0.28±0.02	0.50±0.03
#4	2.6	0.34±0.03	0.67±0.05	0.29±0.04	0.23±0.04
HH PDR	1.8	0.30±0.03	0.60±0.05	0.10±0.02	0.24±0.03
#6	–	–	–	–	–
#7	2	0.4±0.1	0.8±0.1	0.11±0.02	0.23±0.02
#8	3	0.55±0.08	1.1±0.1	0.13±0.04	0.29±0.05
HH CORE	1.7	0.25±0.02	0.63±0.04	–	–
#10	–	0.21±0.04	0.51±0.04	–	–
#11	–	–	–	–	–
#12	–	0.24±0.04	0.51±0.05	–	–
#13	–	0.17±0.04	0.41±0.04	–	–
#14	–	–	–	–	–

assumed that the H^{13}CN $J_u \rightarrow J_l$ line is optically thin, that T_{rot} is the same for the two isotopologues, and that HCN and H^{13}CN $J_u \rightarrow J_l$ emit from the same gas volume (Goldsmith et al. 1984). Hence,

$$\frac{W_{HCN}}{W_{H^{13}CN}} \approx \frac{1-e^{\tau_{HCN}}}{\tau_{HCN}} \frac{[^{12}C]}{[^{13}C]}, \quad (E.1)$$

where τ is the line opacity, W is the integrated line intensity, and $[^{12}C]/[^{13}C]$ is the isotopic ratio, around 60 in Orion (Langer & Penzias 1990).

The H^{13}CN $J=1-0$ line is detected toward NGC 2024 cores, as well as toward the Horsehead PDR and Core positions in the higher sensitivity WHISPER survey (Gerin et al. 2009; Pety et al. 2012). We detect HCN and H^{13}CN $J=2-1$ toward several positions (#1, #2, #3, #4, #7, #8, HH-PDR and HH-Core). Table D.1 shows the estimated HCN $J=2-1$ opacities following Eq. (E.1). We computed the opacities of the rotational lines $J=1-0$ (for positions with no H^{13}CN $J=1-0$ detections), 3–2, and 4–3 as a function of $J=2-1$ line opacity, as:

$$\tau_\nu = \frac{A_{ul}\, g_u}{8\pi\, \Delta v} \left(\frac{c}{\nu}\right)^3 \frac{N_{tot}}{Q(T_{rot})} \frac{e^{h\nu_{ul}/kT_{rot}}-1}{e^{E_u/kT_{rot}}}, \text{ and} \quad (E.2)$$

$$\frac{\tau_{ul}}{\tau_{2-1}} = \frac{A_{ul}\, g_u\, \Delta v_{2-1}}{A_{2-1}\, g_2\, \Delta v_{ul}} \left(\frac{\nu_{2-1}}{\nu_{ul}}\right)^3 \frac{e^{E_2/kT_{rot}}}{e^{E_u/kT_{rot}}} \frac{e^{h\nu_{ul}/kT_{rot}}-1}{e^{h\nu_{2-1}/kT_{rot}}-1}, \quad (E.3)$$

where T_{rot} is the rotational temperature, ul refers to the transition from the upper to lower level, and Δv_{ul} is the linewidth. For simplicity, we assume a linewidth ratio $\Delta v_{2-1}/\Delta v_{ul} = 1$. For the fainter emitting positions, where we do not detect H^{13}CN, we assume that the HCN emission is optically thin.

E.2. Opacity corrected population diagram

In order to determine T_{rot} and the column density toward each observed position, we computed rotational diagrams assuming a single T_{rot}(HCN) (Goldsmith & Langer 1999),

$$\ln\left(\frac{N_u}{g_u}\right) = \ln\left(\frac{N_{tot}}{Q(T_{rot})}\right) - \frac{E_u}{kT_{rot}}, \quad (E.4)$$

where N_u is the level u population, N_{tot} is the total column density. We iteratively applied the opacity correction $\left(C_\tau = \frac{\tau}{1-e^{-\tau}}\right)$ to the population diagram until a solution for T_{rot} and N converged. For the first iteration we use eq. (E.4) and compute the line opacities from eq. (E.3). From the second iteration to convergence, we implement the opacity correction as

$$\ln\left(\frac{N_u}{g_u}\right) = \ln\left(\frac{N_{tot}}{Q(T_{rot})}\right) - \frac{E_u}{kT_{rot}} - \ln C_\tau. \quad (E.5)$$

The uncertainties are $\Delta\left(\ln\left(\frac{N_u}{g_u}\right)\right) = \frac{\Delta W}{W}$, where ΔW is the uncertainty of the integrated intensity, $\sim$20% of W. Figure E.1 shows a comparison between the optically thin (squares and dashed lines), and opacity-corrected HCN population diagrams (circles and straight lines), for positions #1, #2, and #4 in Fig. E.1a, and for positions #7, #8, and Core, in the Horsehead, in Fig. E.1b.

E.3. HNC rotational population diagrams

Table E.1 shows the rotational temperatures and column densities obtained from rotational diagrams constructed with the observed HNC $J=1-0$ and $J=3-2$ lines. This table also shows the estimated $J=1-0$ line opacities toward positions with HNC and HN^{13}C $J=1-0$ detections (assuming that both emission lines steam from the same gas).
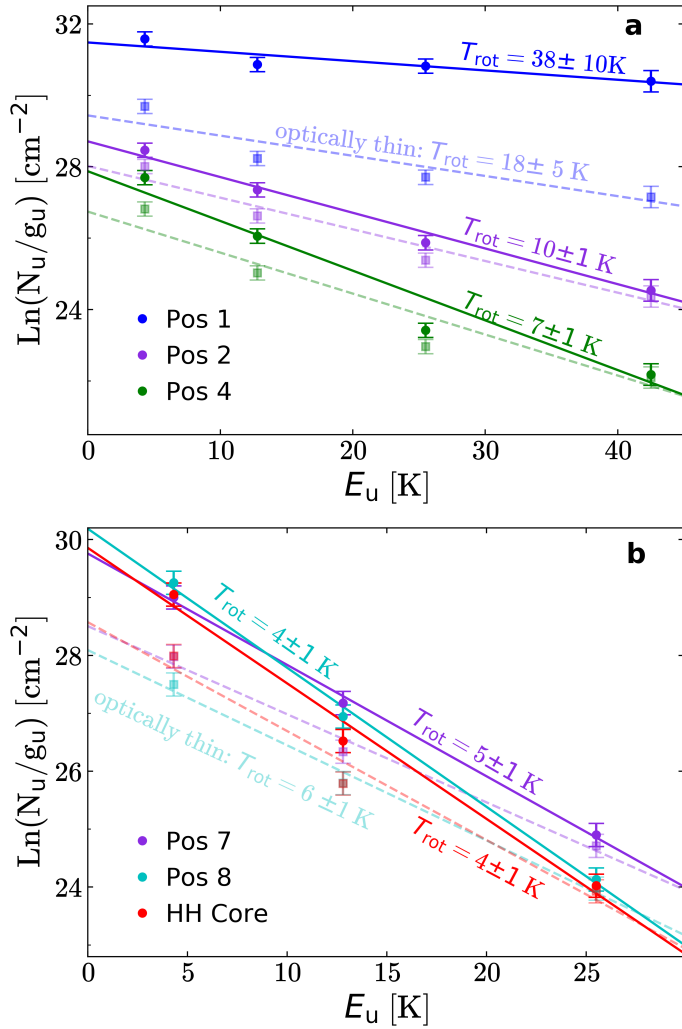
Fig. E.1. HCN rotational diagrams. (a) Opacity corrected (straight lines) population diagrams for positions #1, #2, #4. Lighter color dashed lines and squares show the optically thin population diagrams. (b) The same but for positions #7, #8, and the HH-Core.

Appendix F: Raster crossmap observation strategy

Because the telescope beam size changes with frequency, we split the observation of each position into a small raster crossmap of ~30" extent (the beam size in the 3 mm band). Figure F.1 shows the target positions. This way, the raster averaged spectra from the 2 and 1 mm bands (J=2–1 and 3–2 lines), and to a lesser extend the 0.8 mm band (J=4–3), can directly be compared with the J=1–0 observations.

Table F.1. Observed frequency ranges and telescope parameters

Rec. & Back.	Freq. range [GHz]	δv [km s^{-1}]	HPBW [arcsec]	Pointings [beams]
E1-FTS200	171.7 – 179.8	0.33	14	5
E2-FTS200	249.2 – 253.3	0.22	9	9
	253.3 – 257.3	0.23		
E3-FTS200	349.7 – 357.8	0.17	7	5

Notes. Col 1. EMIR receiver and FTS backend. Col 2. Observed frequency range. Col 3. δv is the observed spectral resolution in velocity units in the observed frequency range. HPBW is the angular resolution of the telescope. Col 4. Number of pointings in the raster map, around each target position, for each spectral band (see Fig. F.1).

Table E.1. HNC excitation temperature and column densities obtained from rotational diagrams, as well as HNC J=1–0 line opacities for positions in which we detected HN^{13}C J=1–0.

	$T_{\rm rot}^{\rm thin}$ [K]	$N^{\rm thin}$ 10^{13} [cm^{-2}]	τ(HNC 1–0)
#1	11	1.6	1.2
#2	9	0.2	
#3	7	0.3	
#4	6	0.3	
PDR HH	5	0.3	1.5
#6	6	0.4	
#7	8	0.9	
#8	8	0.6	
Core HH	6	0.4	2.8
#10	6	0.3	
#11			
#12	6	0.4	
#13	5	0.3	
#14	5	0.1	

HCN 1−0, $\theta_{\mathtt{hpbw}}$(E0) = 27″   HCN 2−1, $\theta_{\mathtt{hpbw}}$(E1) = 14″

HCN 3−2, $\theta_{\mathtt{hpbw}}$(E2) = 9″   HCN 4−3, $\theta_{\mathtt{hpbw}}$(E3) = 7″
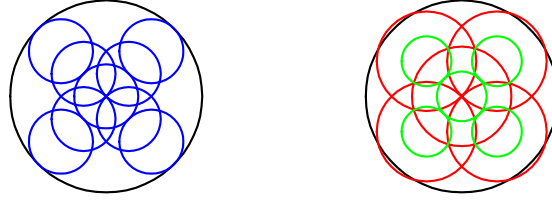
Fig. F.1. Pointing strategy of raster crossmaps designed to obtain multi frequency line observations at the ∼30″ angular resolution of the Orion-B $J = 1$–0 maps.

Appendix G: Complementary figures and tables

In this section we provide figures (Figs. G.1 and G.2) with all detected HCN, HNC, $H^{13}CN$, and $HN^{13}C$ line spectra toward the sampled of selected positions in Orion B (pointed observations). The following tables summarize their observed spectroscopic parameters: integrated line intensities, peak LSR velocity, line width and, peak temperature.
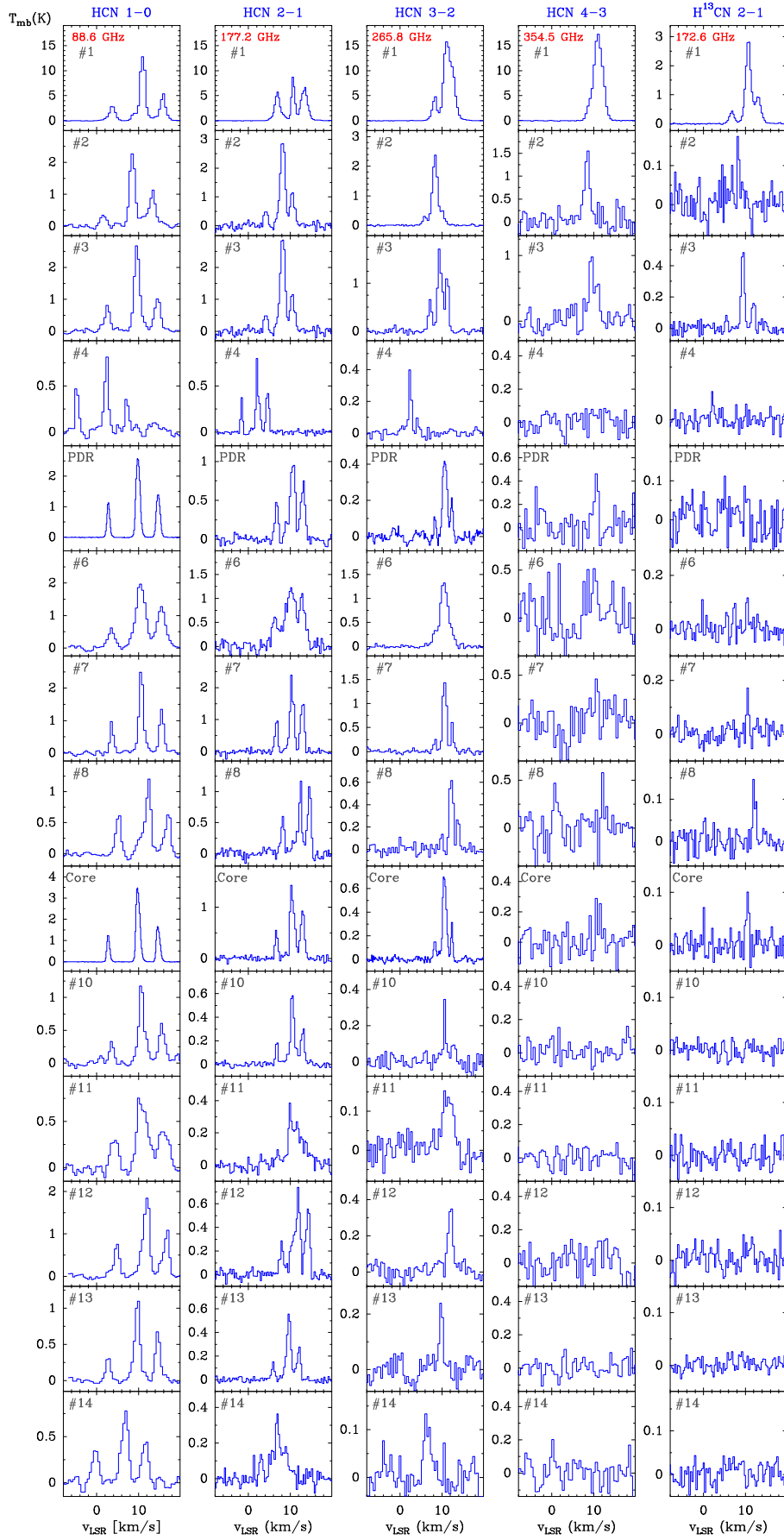
Fig. G.1. HCN J=1–0 to J=4–3, and H^{13}CN J=2–1 pointed observations. The velocity resolution is ~0.5 km s^{-1}.
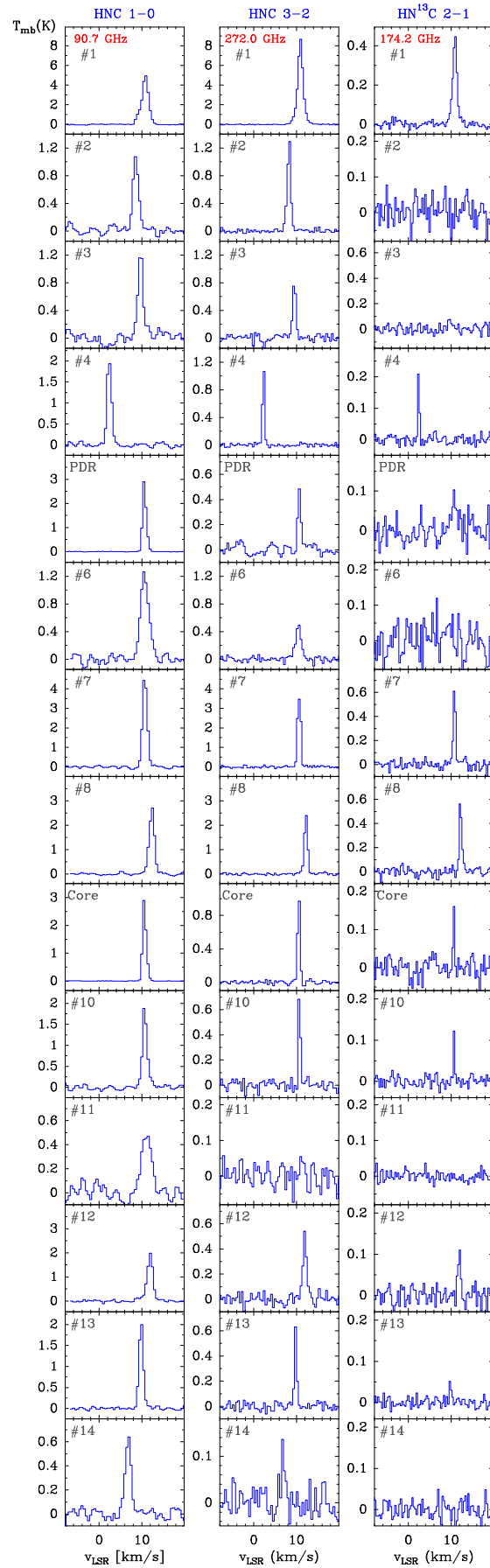
Fig. G.2. HNC J=1–0 and J=3–2, and HN^{13}C J=2–1 pointed observations. The velocity resolution is ~0.5 km s^{-1}.

Table G.1. Line spectroscopic parameters obtained from Gaussian fits to the observed HCN lines.

Freq. [MHz] Pos.	HCN J=1–0 88631.6 W [K km s^{-1}]	v_{LSR} [km s^{-1}]	Δv(F=0-1) [km s^{-1}]	T_{mb} [K]	HCN J=2–1 177261.1 W [K km s^{-1}]	v_{LSR} [km s^{-1}]	$\Delta v^{\dagger}$ [km s^{-1}]	T_{mb} [K]	HCN J=3–2 265886.4 W [K km s^{-1}]	v_{LSR} [km s^{-1}]	$\Delta v^{\dagger}$ [km s^{-1}]	T_{mb} [K]	HCN J=4–3 354505.5 W [K km s^{-1}]	v_{LSR} [km s^{-1}]	$\Delta v^{\ddagger}$ [km s^{-1}]	T_{mb} [K]
#1	37.2	11.0	1.6	12.8	34.5	10.6	6.6	9.7	45.9	11.1	3.8	14.8	46.9	11.0	2.8	16.4
#2	6.9	8.5	1.8	2.3	6.9	8.2	4.0	3.1	4.5	8.4	2.8	2.3	2.9	8.3	3.1	1.7
#3	8.1	9.4	1.5	2.7	8.4	9.2	4.9	3.2	4.0	9.5	3.3	1.5	2.1	9.7	2.4	1.0
#4	2.1	2.6	1.0	0.8	1.4	2.0	4.8	0.9	0.4	2.3	1.9	0.4	0.3	0.8	2.0	0.2
PDR HH	5.6	9.6	1.2	2.3	2.7	10.6	6.0	1.0	0.7	10.5	2.3	0.4	0.23	10.5	0.9	0.4
#6	10.3	10.4	2.0	2.0	6.2	11.3	5.4	1.2	3.6	10.5	2.7	1.3				
#7	6.7	10.5	0.9	2.5	5.2	10.8	2.5	2.4	2.3	10.4	2.6	1.6				
#8	4.2	12.6	1.7	1.2	3.0	12.2	5.5	1.2	1.1	12.1	2.6	0.6				
Core HH	6.8	9.6	0.8	3.2	3.4	10.8	4.7	1.4	1.1	10.5	2.5	0.7				
#10	3.4	10.5	1.1	1.2	1.3	10.7	4.4	0.6	0.4	10.6	2.5	0.3				
#11	4.0	9.9	2.1	0.8	1.4	10.0	5.0	0.4	0.4	10.5	2.5	0.1	–	–	–	–
#12	6.9	12.1	1.5	1.9	2.2	11.8	4.8	0.7	0.7	12.3	3.7	0.3				
#13	3.3	10.0	1.7	1.1	1.1	9.8	4.2	0.6	0.3	9.7	2.8	0.2				
#14	3.2	7.0	1.8	0.8	1.0	6.9	4.8	0.4	0.2	6.2	2.0	0.1				

Notes. W refers to velocity-integrated line intensity, $\int T_{mb}\, dv$.. v_{LSR} is the local standard of rest velocity. T_{mb} is the peak temperature: for J=1–0 is the peak of the F=2–1 component; for J=2–1, the central line are the blended HFS components F=3–2 and F=2–1; for J=3–2, the central line are the blended HFS components F=4–3, 3–2, 2–1; for J=4–3 the HFS is not spectrally resolved. Δv(F=0-1) is the linewidth of the hyperfine component J=1–0 F=0–1. $\Delta v^{\dagger}$ refers to Moment 2 of the J=2–1 line emission (the individual HFS component overlap). $\Delta v^{\ddagger}$ is the J=4–3 total linewidth from a gaussian fit (HFS complents overlap).

Table G.2. Line spectroscopic parameters obtained from Gaussian fits to the observed HNC lines.

Pos.	HNC J=1–0				HNC J=3–2			
Freq. [MHz]	90663.6				271981.1			
	W [K km s^{-1}]	v_{LSR} [km s^{-1}]	Δv [km s^{-1}]	T_{mb} [K]	W [K km s^{-1}]	v_{LSR} [km s^{-1}]	Δv [km s^{-1}]	T_{mb} [K]
#1	9.7±0.1	10.8±0.1	1.9±0.1	4.8	12.4±0.1	11.0±0.1	1.5±0.1	7.8
#2	1.7±0.1	8.6±0.1	1.5±0.1	1.1	1.3±0.1	8.4±0.1	1.0±0.1	1.3
#3	1.9±0.1	9.7±0.1	1.4±0.1	1.2	0.8±0.1	9.3±0.1	0.9±0.1	0.8
#4	2.6±0.1	2.4±0.1	1.2±0.1	2.1	0.7±0.1	2.3±0.1	0.5±0.1	1.0
PDR HH	2.4±0.1	10.7±0.1	1.1±0.1	2.0	0.4±0.1	10.6±0.1	0.8±0.1	0.5
#6	3.0±0.1	10.7±0.1	2.3±0.1	1.2	0.8±0.1	10.6±0.1	1.5±0.1	0.5
#7	6.5±0.1	10.7±0.1	1.3±0.1	4.7	3.7±0.1	10.6±0.1	1.0±0.1	3.5
#8	4.2±0.1	12.4±0.1	1.5±0.1	2.7	2.4±0.1	12.2±0.1	1.0±0.1	2.4
Core HH	3.1±0.1	10.6±0.1	1.0±0.1	2.9	0.7±0.1	10.6±0.1	0.6±0.1	1.0
#10	2.6±0.1	10.7±0.1	1.3±0.1	1.9	0.5±0.1	10.5±0.1	0.5±0.1	0.7
#11	1.4±0.1	11.1±0.1	2.7±0.1	0.5	–	–	–	–
#12	3.2±0.1	12.0±0.1	1.6±0.1	1.9	0.6±0.1	11.8±0.1	1.1±0.1	0.5
#13	2.7±0.1	9.9±0.1	1.2±0.1	2.1	0.4±0.1	9.8±0.1	0.6±0.1	0.6
#14	1.1±0.1	6.8±0.1	1.7±0.1	0.6	0.1±0.1	6.6±0.1	0.7±0.1	0.1

Notes. W refers to velocity-integrated line intensity, $\int T_{\mathrm{mb}}\, dv$. T_{mb} is the line peak temperature.

Table G.3. Line spectroscopic parameters obtained from Gaussian fits to the observed H^{13}CN and HN^{13}C lines.

Pos.	H^{13}CN J=2–1				HN^{13}C J=2–1			
Freq. [MHz]	172677.9				174179.4			
	W [K km s^{-1}]	v_{LSR} [km s^{-1}]	$\Delta v^{\dagger}$ [km s^{-1}]	T_{mb} [K]	W [K km s^{-1}]	v_{LSR} [km s^{-1}]	Δv [km s^{-1}]	T_{mb} [K]
#1	8.0	10.7	4.3	3.3	0.6±0.1	10.9±0.1	1.2±0.1	0.5
#2	0.2	7.4	3.7					
#3	0.67	9.72	3.6					
#4	0.06	2.4	3.0	0.05	0.1±0.1	2.4±0.1	0.4±0.1	0.2
PDR HH	0.08±0.02	10.4±0.1	0.9±0.2	0.08	0.1	10.7±0.2	1.2±0.8	0.1
#6	0.08	11.3	2.1	1.0				
#7	0.18	9.7	5.8		0.44±0.02	10.80±0.02	0.64±0.04	0.6
#8	0.15	12.1	3.9		0.45±0.02	12.2±0.02	0.71±0.04	0.59
Core HH	0.1	11.0	4.0		0.07±0.01	10.62±0.09	0.4±0.4	0.2
#10					0.049±0.008			
#11	–	–	–	–	–	–	–	–
#12					0.09±0.01	11.94±0.06	0.8±0.1	0.11
#13					0.03±0.006	9.8±0.03	0.3±0.1	0.08
#14								

Notes. W refers to velocity-integrated line intensity, $\int T_{\mathrm{mb}}\, dv$. T_{mb} is the line peak temperature. $\Delta v^{\dagger}$ refers to Moment 2 of the J=2–1 line emission (the individual HFS component overlap).